EXTRACTION OF ELASTIC-PLASTIC MATERIAL PROPERTIES FROM SPHERICAL INDENTATION STRESS-STRAIN MEASUREMENTS AND FINITE ELEMENT SIMULATIONS

A Dissertation
Presented to
The Academic Faculty

by

Dipen K. Patel

In Partial Fulfillment
of the Requirements for the Degree
Doctor of Philosophy in the
George W. Woodruff School of Mechanical Engineering

Georgia Institute of Technology
May 2017

EXTRACTION OF ELASTIC-PLASTIC MATERIAL PROPERTIES FROM SPHERICAL INDENTATION STRESS-STRAIN MEASUREMENTS AND FINITE ELEMENT SIMULATIONS

Approved by:

Dr. Surya R. Kalidindi, Advisor
George W. Woodruff School of Mechanical Engineering
Georgia Institute of Technology

Dr. Richard W. Neu
George W. Woodruff School of Mechanical Engineering
Georgia Institute of Technology

Dr. David L. McDowell
School of Materials Science and Engineering
Georgia Institute of Technology

Dr. Antonia Antoniou
George W. Woodruff School of Mechanical Engineering
Georgia Institute of Technology

Dr. Hamid Garmestani
School of Materials Science and Engineering
Georgia Institute of Technology

Date Approved: 26 September 2016

This work is dedicated to my Parents, Kirti and Jagruti Patel and my wonderful, young sister, Tulsi. The work penned here would not have been possible without the support and sacrifices of my Parents, sister and our beloved Mota Papa, Ashwin kaka.

ACKNOWLEDGEMENTS

I wish to thank my advisor Prof. Surya R. Kalidindi for his support and guidance without which this work would not have been possible. I would especially thank him for providing the opportunity to work on different research topics and encouraging me to think independently. I am also grateful to Dr. David McDowell, Dr. Richard Neu, Dr. Hamid Garmestani and Dr. Antoniou for taking the time to be on my thesis committee.

I would like to express my sincere gratitude to Materials INformatics and Engineering Design (MINED) group who have helped and supported me during my PhD at Georgia Tech. I would especially thank Mr. Hamad Al-Harbi and Mr. Jordan Weaver for many insightful discussions on nanoindentation through the course of my PhD.

I would also like to thank all the faculty and staff of Mechanical Engineering department, especially Glenda Johnson for her help on various departmental issues over the years.

Additionally, I would like to thank National Science Foundation (NSF) and U.S. Department of Energy, Office of Nuclear Engineering, Nuclear Engineering Enabling Technology (DOE-NEET) and Army Research Office (ARO) for providing the financial support for the work.

Lastly, I wish to thank my family and friends for their support and encouragement through the completion of my PhD.

TABLE OF CONTENTS

LIST OF TABLES

Page

LIST OF FIGURES

LIST OF SYMBOLS AND ABBREVIATIONS

FEM	Finite Element Method
EBSD	Electron Backscatter Diffraction
ISS	Indentation Stress-Strain
USS	Uniaxial Stress-Strain
Fe-3% Si	Iron-3% Silicon
P	Indentation Load
h_t	Total Displacement
h_e	Elastic Displacement
E_{eff}	Effective Modulus
R_{eff}	Effective Radius
E	Young's Modulus
E_s	Sample Modulus
ν	Poisson Ratio
ν_s	Sample Poisson Ratio
ν_i	Indenter Poisson Ratio
E_i	Indenter Young's Modulus
h_r	Residual Displacement
a	Contact Radius
R_i	Indenter Radius
R_s	Sample Radius
σ_{ind}	Indentation Stress
ε_{ind}	Indentation Strain

σ_y	Uniaxial Yield Stress
OIM	Orientation Image Map
IPF	Inverse Pole Figure
MSD	Microstructure Sensitive Design
SSH	Spherical Surface Harmonics Functions
T_l^m	Generalized SSH
K_l^m	Symmetrized SSH
$g \in (\varphi_2, \Phi)$	Bunge-Euler Angles
P_l^m	Associated Legendre Polynomial
δ	Kronecker Delta
FZ	Fundamental Zone
A	Zener Anisotropic Ratio
UMAT	User Materials Subroutine

SUMMARY

Simulating complex interactions at different length scales of a hierarchical material system is essential to multi-scale modelling techniques. Such models, however, need reliable information on the effective properties measured at different length scales (i.e., spanning from the macroscale to the microscale constituents). This dissertation presents new protocols for estimating these multiscale properties from the indentation stress-strain curves measured using recently developed spherical indentation protocols. More specifically, protocols are developed to extract the homogenized (bulk) properties (e.g., uniaxial yield strength and hardening rate) at the macroscale. At the microscale, new protocols are formulated to extract single crystal elastic-plastic parameters (e.g., elastic stiffness constants and initial slip resistance) from nanoindentation measurements. All of the new protocols will be validated using a finite element model of the spherical indentation, used here as a surrogate for the actual experiment. The protocols are also demonstrated on a range of materials, for which experimental measurements have been published in prior literature.

CHAPTER 1

INTRODUCTION

Integration of advanced material systems into most engineering applications requires a detailed understanding of the deformation behavior of such materials. Successful integration requires simulating complex interactions at different length scales. Such models, however, need reliable information on the effective properties measured at different length scales (i.e. spanning from the macroscale to the microscale constituents) as illustrated in Figure 1.1.

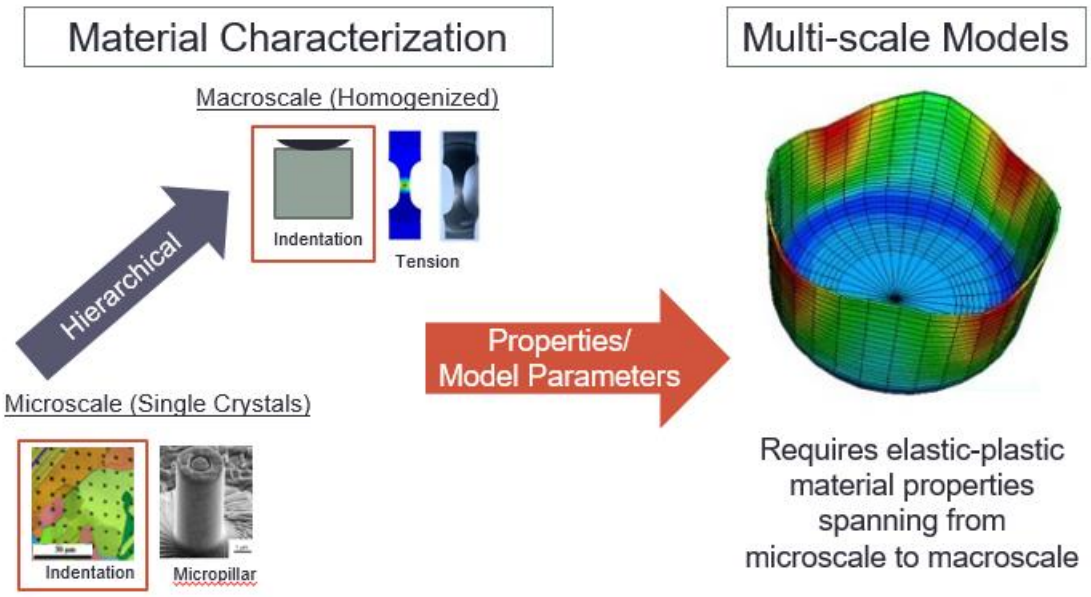

Figure 1.1. Illustration of the hierarchical material structure and its integration into structural applications requires multi-scale models.

The overall performance characteristics of such material systems are typically measured under uniaxial loading conditions such as simple tension or simple

compression (ASTM, 2015). However, testing methods for extracting the local properties from these individual microscale constituents are still in developmental stages (Uchic et al., 2004; Zhang et al., 2006). Knowledge of homogenized properties (e.g., uniaxial yield strength) as well as local properties (e.g., grain-scale elastic-plastic material constant) at different length scales is critical to the formulation and validation of physics-based multiscale materials models (Groh et al., 2009; Panchal et al., 2013; Roters et al., 2010).

Indentation is a versatile tool for measuring the mechanical properties from small material volumes (Cordill et al., 2009; Field and Swain, 1993; Li and Bhushan, 2002; Oliver and Pethica, 1989; Oliver and Pharr, 1992). The technique has been used widely in the past to determine the elastic modulus and hardness of the sample material from the unloading segment of the load-displacement data, which is purely elastic. Kalidindi et al. (Kalidindi and Pathak, 2008; Pathak et al., 2008; Pathak et al., 2009) recently developed a novel approach to convert load-displacement data measured during the initial loading segments in spherical nanoindentation into more meaningful indentation stress-strain (ISS) curves. The new data analysis procedure reliably captures the local elastic, yield, and post-elastic behavior during the deformation process for various material systems. With this new characterization technique, we are now in a position to extract elastic-plastic (isotropic and anisotropic) material properties required for multi-scale modelling.

In this context, spherical nanoindentation provides a new opportunity to deduce the constitutive models that govern the deformation behavior of materials. A large number of analytical and numerical approaches employed over the last few decades reveal that the interpretation of the indentation response is not a straightforward task, and

requires careful treatment. It is imperative to recognize that the stress-strain fields realized in spherical indentation test and a uniaxial test (e.g., simple compression or tension) are fundamentally different. In particular, the stress fields in the indentation test are highly heterogeneous compared to uniaxial loading conditions and present a significant challenge to the recovery of the physical material properties.

Previous characterization studies in using spherical indentation were mainly focused on the extraction of meaningful indentation stress-strain curves from small material volumes. However, these previous investigations did not resolve the relevant elastic-plastic properties used in physics-based multi-scale material models. Nanoindentation analysis protocols coupled with a suitable finite element model have the potential to resolve the elastic-plastic properties of interest in multi-scale material model theories.

The objective of this dissertation is to develop novel protocols for estimating homogenized (macroscale) and local (microscale) elastic-plastic properties of polycrystalline sample material using spherical nanoindentation. At the macroscale, protocols are formulated to predict homogenized properties (i.e. uniaxial yield strength and hardening rate) using isotropic J2 flow theory of plasticity. This is done by correlating ISS response to uniaxial stress-strain (USS) response. To understand the macroscale response of a polycrystalline sample, one also needs to understand the microscale response. At the microscale, the deformation behavior depends on the local constituent details such as crystal orientation and the elastic-plastic properties (e.g., elastic stiffness constants, initial slip resistance, and initial hardening rates) of the single crystal. Novel protocols are formulated to estimate these single crystal elastic-plastic

parameters using indentation experimental observation coupled with finite element models. The merits of the proposed approach in this work will be demonstrated with a specific case study on as-cast polycrystalline sample.

The dissertation is structured as follow. Chapter 2 briefly reviews the tools/techniques utilized throughout the thesis. Since spherical nanoindentation technique forms the basis of this work, the chapter begins with a review of the current nanoindentation analyses protocols of extracting mechanical properties and converting load-displacement curves to indentation stress-strain curves. In Chapter 3, protocols are developed to address the longstanding problem of recovering macroscale, uniaxial mechanical properties from instrumented indentation experiments, with the central challenge being the lack of validated protocols for converting indentation stress-strain values to equivalent values in uniaxial stress states such as simple compression of an isotropic material system following a J2 flow theory. In Chapter 4 and Chapter 5, protocols are developed to extract microscale elastic-plastic properties. More specifically, in Chapter 4 a two-step inverse methodology is developed to estimate the single crystal elastic stiffness parameters for polycrystalline samples using spherical nanoindentation and orientation measurements from electron backscattered diffraction (EBSD) combined with FE simulations. The accuracy and viability of the approach were demonstrated for an as-cast cubic polycrystalline Fe-3% Si sample. In Chapter 5, an application of the two-step procedure developed in chapter 4 is demonstrated to estimate the average slip resistance in a cubic polycrystalline metal sample from spherical nanoindentation and lattice orientation measurements. The validity of the approach is demonstrated for annealed Fe-3% Si using measurements published in prior literature. Chapter 6

summarizes the dissertation and includes possible directions for future research endeavors.

CHAPTER 2

BACKGROUND

Development of physics-based multi-scale materials model with excellent predictive capabilities is largely hampered by lack of methods to characterize materials at multiple length scales of interest. One approach explored in literature involves the fabrication of micro-pillar tests (Li et al., 2011; Shan et al., 2008; Uchic et al., 2004) using focused ion-beam and deforming the micro-pillar in compression. Preparation of micro-pillar requires intricate fabrication and handling which comes with certain challenges such as ion beam damage, misalignment of the pillar under compression – leads to a non-uniform cross section, etcetera. This approach requires access to highly sophisticated equipment and is not particularly well suited for extracting the local elastic-plastic property of the microscale constituents. In contrast to micro-pillar testing, nanoindentation can provide mechanical information at different length scales at significantly lower effort and cost. Traditionally, indentation test has been one of the most common technique for measuring hardness properties of materials at large effective strains using sharp indenters. Although sharp indenters are effective in measuring the properties at finite plastic strains, the inherent high stress concentration at the tip is a major impediment in studying the elastic and elastic-plastic behavior of a material which makes the spherical indenters a more likely option for such studies.

2.1 Spherical nanoindentation

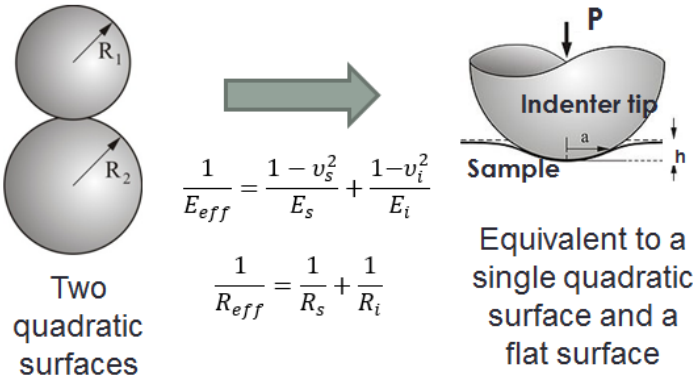

Figure 2.1. Demonstrate the transformation of contact between two quadratic surface to a case of indenting a flat deformable surface by a single quadratic surface.

Spherical nanoindentation data analyses procedures are largely based on Hertz's theory (H., 1896; Johnson and Johnson, 1987; Willis, 1966), which assumes frictionless, elastic, contact between two isotropic quadratic surfaces. The main result of this theory can be expressed as

$$P = \frac{4}{3} E_{eff} R_{eff}^{\frac{1}{2}} h_t^{\frac{3}{2}}, \qquad a = \left(\frac{3PR_{eff}}{4E_{eff}} \right)^{1/3} \tag{2.1}$$

where a is the contact radius at the indentation load P and the penetration depth, h_t. $h_t = h_e$ for purely elastic indentation. R_{eff} and E_{eff} denote the effective radius and the effective indentation modulus of the sample and the indenter system, defined as

$$\frac{1}{E_{eff}} = \frac{1-\upsilon_s^2}{E_s} + \frac{1-\upsilon_i^2}{E_i}, \qquad \frac{1}{R_{eff}} = \frac{1}{R_s} + \frac{1}{R_i} \tag{2.2}$$

In Eq. (2.2), E and ν denote the Young's modulus and Poisson's ratio of the indenter (subscript *i*) and the specimen (subscript *s*), and R denotes the radius. In the purely elastic indentation of a perfectly flat surface, $R_{eff} = R_i$. Eq. (2.2) is a transformation of the elastic indentation response between the two isotropic, quadratic deformable bodies (i.e.

the sample and the indenter) to the elastic response in the case of contact between a flat isotropic deformable sample by a spherical indenter as illustrate in Figure 2.1.

The extraction of macroscale and microscale material properties using spherical nanoindentation (e.g. modulus, uniaxial yield strength) is discussed next.

2.1.1 Extracting macroscale properties

Bulk mechanical properties of materials are typically measured under uniaxial loading conditions such as simple tension or simple compression (ASTM, 2015). However, testing methods for extracting these properties from exceedingly small sub-volumes of a sample requires local characterization technique such as indentation. As mentioned earlier, indentation test has been one of most common techniques for measuring macroscale (i.e. hardness) properties of materials at large strains. These hardness measures were found to be invaluable in quickly assessing the resistance to plastic deformation in rage of materials. In spite of these advantages, hardness measurements continue to be used mainly as a comparative measure since hardness numbers are sensitive to indenter shape, indenter size, and the imposed load level.

As a natural extension of the hardness measurement, Tabor (Tabor, 1951) recognized the need to standardize the hardness measurements and introduced the concept of normalized indentation stress-strain curves (ISS). Tabor recorded the hardness measurements on copper and steel using spherical indenter at different loads and aggregating them into a single ISS curve for each material. Tabor assumes indentation stress (Meyer's hardness) as load, P normalized by the projected contact area, A. The

projected contact area was determined by measuring the impression left after unloading the indenter. Then, the ISS curves can be defined as

$$\sigma_{ind} = \frac{4E_{eff}}{3\pi}\varepsilon_{ind}, \qquad \sigma_{ind} = \frac{P}{\pi a^2}, \qquad \varepsilon_{ind} = \frac{a}{R_{eff}}. \tag{2.3}$$

The linear relationship between stress and strain in elastic indentation has prompted many studies (Basu et al., 2006; Field and Swain, 1993; Field and Swain, 1995; Herbert et al., 2001; Swain, 1998) to adopt some variant of a/R_{eff} as a measure of indentation strain for more general case of elastic-plastic indentation.

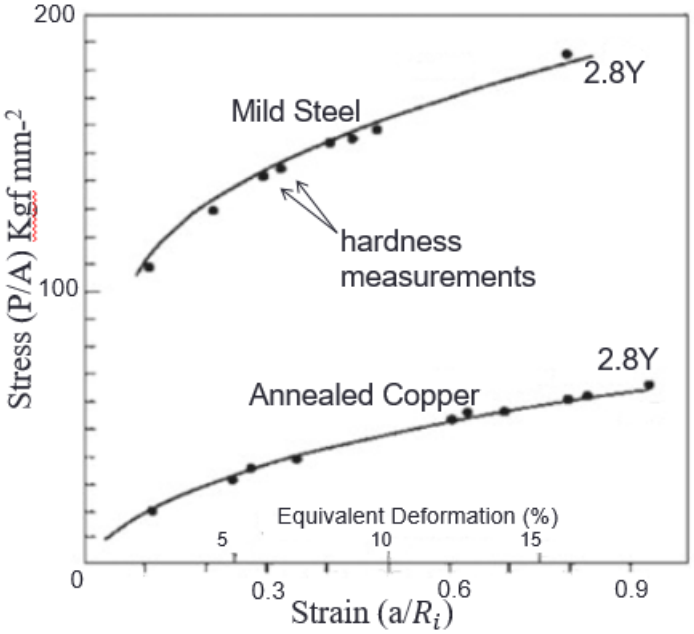

Figure 2.2. Tabor correlate indentation measurements to uniaxial stress-strain response for mild steel and annealed copper taken from Tabor, 1951

Following the ISS definition defined in Eq. (2.3), Tabor was able to empirically correlate experimentally measured value of indentation flow stresses and strains on annealed copper and mild steel to a uniaxial test of the same materials. More specifically, Tabor showed a reasonable agreement between ISS and uniaxial stress-strain curves

when the uniaxial true stress is scaled by a factor of 2.8 and the uniaxial true strain by a factor of 0.2 (Tabor, 1951) as shown in Figure 2.2. The factor of 2.8 is defined as constraint factor as it captures the effect of the higher hydrostatic pressure associated to the indentation test. Numerous numerical/analytical studies (Hill, 1948; Hill et al., 1947; Hill et al., 1989; Ishlinsky, 1944; Johnson, 1987; Johnson and Johnson, 1987) support the scaling of indentation stress-strain curves to extract the uniaxial macroscale properties using Tabor's approach. However, the scaling relationship is constraint to a fully plastic indentation defined by a specific range of a/R_{eff} (Herbert et al., 2001). Also, the definition of indentation strain as a/R_{eff} lacks any physical interpretation as a measure of strain. This is because strain should be fundamentally interpreted as a ratio of the change in length over the initial length of a selected line segment in region of interest in the sample.

Tabor's work has stimulated numerous theoretical studies aimed at correlating the elastic-plastic stress-strain responses in indentation and simple compression. The theoretical treatment for the perfectly-plastic deformation imposed by a rigid frictionless indenter was first explored by Hill (Hill et al., 1947) using slip-line field approach and assuming plane strain deformation (note that the real deformation mode in indentation is far from this assumption). This approach, applied to the rigid plastic deformation of a flat sample with a wedge indenter, produces the widely cited result that the average pressure under the (wedge) indenter being approximately three times the flow stress in a uniaxial test. Subsequently, Ishlinksy (Ishlinsky, 1944) performed slip-line field analysis of a spherical contact and reported that the contact pressure for a perfectly plastic contact (no hardening) is between 2.61 and 2.84. In the slip-line analyses, the volume of material

displaced by the indenter is accounted by the upward flow of the material as shown in Figure 2.3 (i.e. the material bounded in the region ABCDE flows outward and upward as the load is imposed on the indenter). It should be noted that the imposed plane-strain boundary conditions in these theoretical approaches naturally yields an upper bound in determining the constraints factor (Yu and Blanchard, 1996).

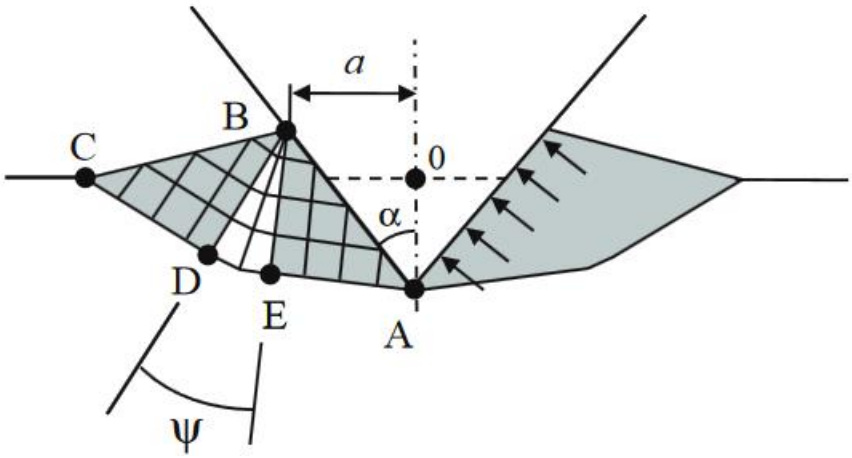

Figure 2.3. Schematics of slip-lines (lines of maximum shear stress) under the indenter (Fischer-Cripps, 2011).

An alternative approach to the analysis of an elastic-plastic indentation was suggested by Bishop *et al*. (Bishop et al., 1945), and was further developed extensively by Johnson (Johnson, 1987). The spherical cavity model (Fig. 2.4) proposed by Johnson assumes that the surface of the indenter in contact is encased in a hemi-spherical core that essentially comprises both the rigid indenter and the surrounding material. The core is assumed to be in a hydrostatic stress state (i.e., the core acts as an inflating spherical cavity). Outside the core, it is assumed that the stress and displacement are radially symmetric, same as in an infinite elastic perfectly-plastic body containing a spherical cavity under pressure. The stress and displacement fields are computed invoking two

conditions at the interface between the core and the elastic-plastic zone (Johnson, 1987): (i) the hydrostatic pressure in the core must be equal the radial component of stress in the external zone, and (ii) neglecting the compressibility in the core, the displacement of points lying on the interface during penetration must accommodate the volume of material displaced by the indenter.

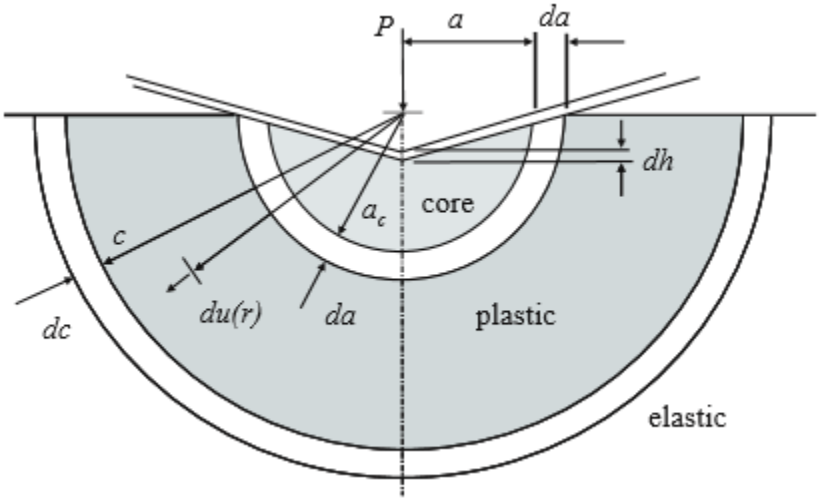

Figure 2.4. Schematic of spherical cavity model. Indenter is encased by a hydrostatic core of radius a_c which is surrounded by a hemispherical plastic zone of radius c. An increment in the displacement of indenter, dh results in a uniform expansion of the core da. The volume displaced by the indenter is accommodated by radial movement of the material $du(r)$ at the boundary between the core and the plastic zone (Fischer-Cripps, 2011)

The spherical cavity model of indentation predicts that the mean pressure at initial yield (deviation from Hertz theory) is 1.1 times the uniaxial flow stress, and at the fully plastic state, it would reach around 3.0 times the uniaxial flow stress. Although the spherical cavity model allows imposing large plastic deformation on the sample, it neglects the upheaval or "pile-up" behavior of the material around an indenter. Also, the model assumes uniform expansion of the material around the core as in the case of spherical pressurized void in an infinite elastic-plastic space. These assumptions severely limit the

utility of this approach. Moreover, numerical studies (Fischer-Cripps, 1997) showing the evolution of plastic zone beneath the indenter also shows significant deviation in the contours of maximum shear stress from the expanding cavity model as shown in Fig. 2.5.

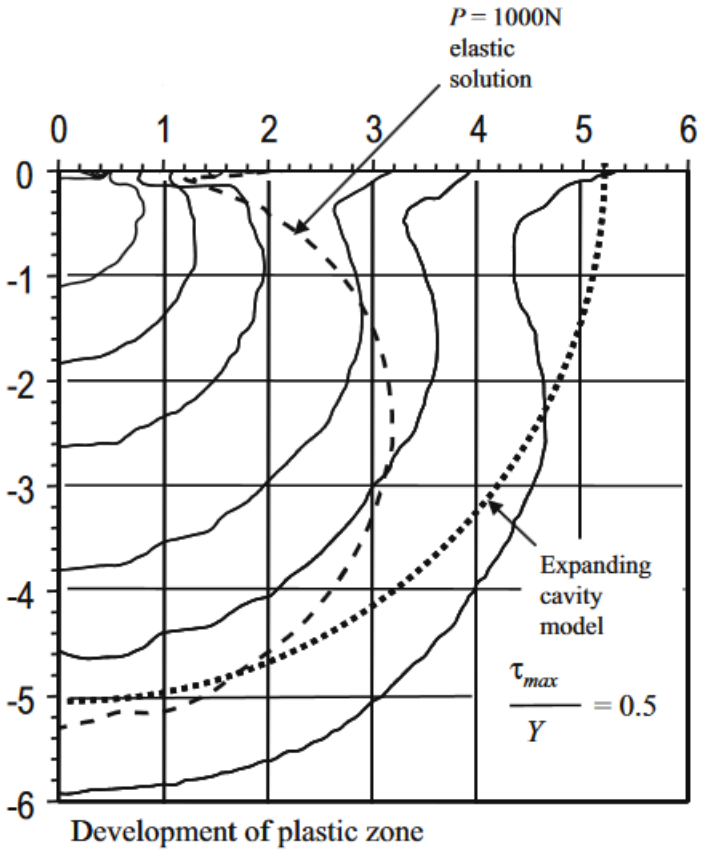

Figure 2.5. Comparing contours of maximum shear stress using FE model and expanding cavity model of elastic-plastic indentation response for mild steel material, E/Y = 550.

In practice, it is very difficult to compute theoretically the contact stresses in an elastic-plastic indentation, because the shape and the size of the elastic-plastic boundary cannot be captured adequately in idealized simple geometries. This has led to the development of various numerical methods to the indentation simulation problem. One of the first numerical models for spherical indentation was established by Hill (Hill et al., 1989) using the infinitesimal deformation theory of plasticity. In this model, Hill invokes

geometrical-similarity in the scaling of contact variables as a function of penetration depth with the spherical indenter approximated by a paraboloid of revolution. Hill's model is in excellent agreement with Tabor's findings that the representative indentation strain is $0.2a/R_i$ and that the average pressure is 2.8 times the uniaxial flow stress in tension. It should be noted that Hill's model makes the following simplifying assumptions: (i) the constitutive behavior of the indented half-space is governed by a simple power-law between suitable measures of stress and strain, and the elastic contribution to the deformation is neglected, (ii) the contact geometry remains constant throughout the indentation, and (iii) the diameter of the indenter is very large compared to the indentation depth leading to infinitesimal plastic strain imposed on the material. In spite of these simplifying assumptions, it is remarkable that the predictions of the numerical model are in excellent agreement with Tabor's experiments.

In an effort to extend the applicability of Hill's model (Hill et al., 1947) while capturing the complex heterogeneous deformation field under the indenter, several recent studies have resorted to finite element models (Beghini et al., 2006; Bhattacharya and Nix, 1988; Park and Pharr, 2004; Taljat et al., 1998). A majority of these studies report a value of around 3.0 for the constraint factor for an elastic-perfectly plastic response. However, the ISS curves produced by these models show unusually large elastic-plastic transitions with high levels of apparent strain hardening (note that the materials constitutive behavior was assumed to be elastic-perfectly plastic in these models). In a recent study Donohue et al. (Donohue et al., 2012) pointed out that these abnormal features of the ISS curves arise because of the use of specific definitions of the contact

radius and the indentation strain measures that are completely inconsistent with Hertz's theory.

2.1.2 Extracting microscale properties

Instrumented indentation (Doerner and Nix, 1986; Oliver and Pharr, 1992) exhibits tremendous potential as a low cost, high throughput, approach because of its capability to probe quickly multiple local volumes in a small sample. Hence, indentation techniques have been employed successfully to characterize the local mechanical responses in individual grains in a polycrystalline sample (i.e., at length scales significantly lower than typical grain sizes). Although one can measure directly the local response at selected locations in a sample, one still needs a sophisticated strategy to extract the values of the elastic-plastic parameters of interest from the measured load-displacement curves. The general approach for addressing this challenge has been to employ optimization strategies that minimize a suitably defined error between the measurements (typically the load-displacement curves) and the corresponding predictions from a finite element (FE) simulation of the indentation experiment, by fine-tuning the model parameters of interest (such as slip resistances aka critical resolved shear stress). Examples of such efforts have included the extraction of the average slip resistance value for single crystal copper (Liu et al., 2008; Zaafarani et al., 2006) and the hardening rate for low-alloy steels (Dao et al., 2001; Kucharski and Mróz, 2001). Since the entire elastic-plastic transition occurs over a very short regime in the indentation load-displacement curve (Kalidindi and Pathak, 2008; Pathak and Kalidindi, 2015), it is

generally very difficult to identify this regime precisely on the measured load-displacement curve as shown in Figure 2.6.

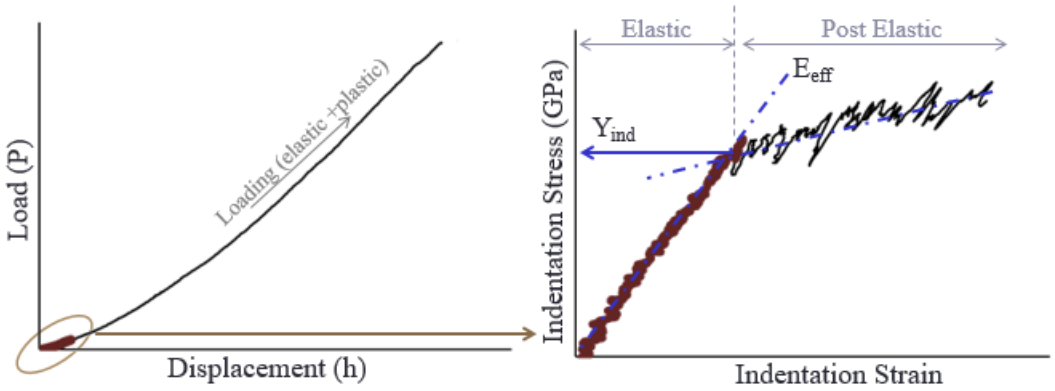

Figure 2.6. Shows the elastic-plastic transition occurs over a short regime on a load-displacement curve and illustrate the need to convert load-displacement curve to indentation stress-strain curve for clear identification of elastic, elastic-plastic transition and post-elastic behavior.

Consequently, values of the slip parameters estimated using such approaches are generally not robust (i.e., very sensitive to small changes in the protocols employed). Indeed, it is much more practical and insightful to compare the indentation stress-strain curves instead of the load-displacement curves in calibrating the material constitutive laws (Donohue et al., 2012). In this regard, the recently developed spherical nanoindentation data analysis protocols have shown tremendous potential (Kalidindi and Pathak, 2008; Pathak and Kalidindi, 2015) in converting the load-displacement curves to indentation stress-strain curves. These new data analysis protocols discussed in the following section enables to convert the load-displacement data obtained during spherical nanoindentation into a meaningful indentation stress-strain (ISS) curve, which exhibits a clear initial elastic regime followed by an elastic-plastic transition (Kalidindi and Pathak, 2008; Pathak et al., 2008; Pathak et al., 2009).

2.1.3 Indentation stress-strain measures

The central issues in recovering reliable indentation stress-strain curve from indentation load-displacement curve revolves around the definition of indentation stress and indentation strain. As mentioned earlier, commonly use definition of indentation stress and indentation strain, Eq. (2.3) lack physical significance. Recently, a more physical definition of indentation stress and indentation strain was proposed (Kalidindi and Pathak, 2008) defined as

$$\sigma_{ind} = E_{eff}\varepsilon_{ind}, \qquad \sigma_{ind} = \frac{P}{\pi a^2}, \qquad \varepsilon_{ind} = \frac{4}{3\pi}\frac{h_t}{a} \approx \frac{h_t}{2.4a}. \tag{2.4}$$

Note that Eq. (2.4) is essentially a rearrangement of Hertz's theory expressed in Eq. (2.1). This particular rearrangement suggests the use of the ratio h_t/a as the definition of indentation strain. The pre-multiplier, $4/3\pi$ in the definition of indentation strain was justified by noting that $2.4a$ corresponds to the depth of the indentation zone (Donohue et al., 2012). This definition of indentation strain allows interpretation of strain measure in the classical sense as the change in length per unit length by idealizing the deformation under indenter as being equivalent to compressing by h_t (total indentation depth) a cylindrical sample of radius a and height $2.4a$.

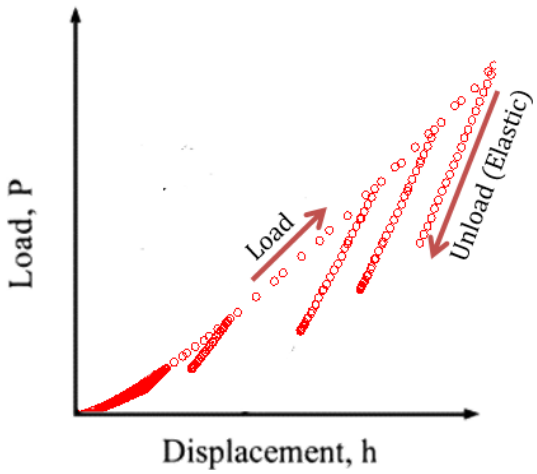

Figure 2.7. Load-displacement response from FE simulations. Unloading segment represents purely elastic behavior (i.e. each segment can be analyzed using Hertz's theory.

The definition of ISS curves, Eq. (2.4) requires precise information about the contact radius, a. Estimation of the contact radius (see Eq. (2.1)) needs an estimate of the effective radius. Note that the contact radius as well as the effective radius evolves continuously once plastic deformation initiates under the indenter. In simulations, contact radius can only be estimated from the unloading segments (see Figure 2.7) which are presumably purely elastic and enables application of the Hertz's theory. Each purely elastic unloading segment satisfies the following modified relationship of Eq. (2.1)

$$h_t - h_r = \left(\frac{3P}{4E_{eff}\sqrt{R_{eff}}}\right)^{2/3} \tag{2.5}$$

A least-fit between h_t and $P^{2/3}$ for the data in each of the unloading segment produces the best estimate of R_{eff} and the residual depth, h_r that corresponds to the peak load. Now, contact radii at the corresponding depth can be computed using Eq. (2.1). The corresponding indentation stress and indentation strain can be tabulated using Eq. (2.4).

Donohue et al. (Donohue et al., 2012) critically evaluated the indentation stress-strain definitions proposed by Tabor (Tabor, 1948, 1951), Field and Swain's (Field and Swain, 1995) and Kalidindi and Pathak (Kalidindi and Pathak, 2008) using finite element model of indentation for isotropic elastic-plastic material response. It was found that the protocols developed by Kalidindi and Pathak yields more realistic results. For a rigid perfectly plastic response, as expected the indentation stress-strain response shows no hardening behavior using the Kalidindi and Pathak approach; whereas, other ISS protocols shows significant strain hardening as shown in Fig. 2.8. The study concludes that the contact radius estimated using the Kalidindi and Patahak's protocols are consistent with the Hertz's theory (Donohue et al., 2012).

ε / a	$\left(\frac{3PR^*}{4E^*}\right)^{1/3}$	$\sqrt{2h_cR_i - h_c^2}$
$4h_t/3\pi a$	A	B
$4a/3\pi R_i$	D	C

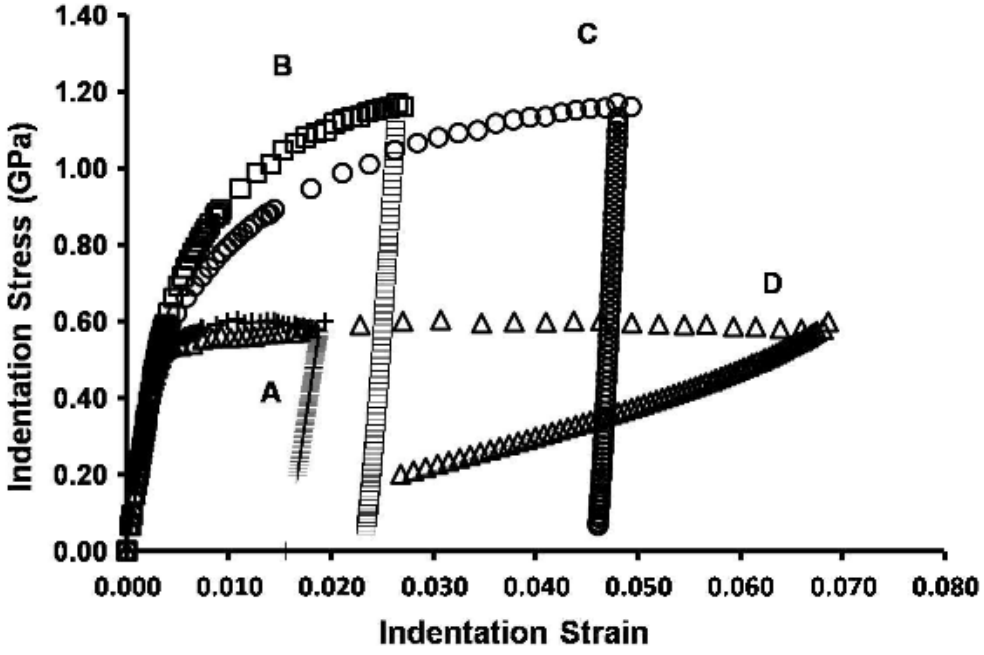

Figure 2.8. ISS curves for isotropic elastic-perfectly plastic material from FEM simulation using different definitions of contact radius and indentation strain taken from Donohue et al. 2012.

The recently developed ISS protocols is further used to capture the anisotropic elastic-plastic deformation behavior in polycrystalline Fe-3% Si (Kalidindi and Pathak, 2008). The protocols were able to record the changes in the indentation modulus and yield strength dependence on the lattice orientation as Figure 2.9.

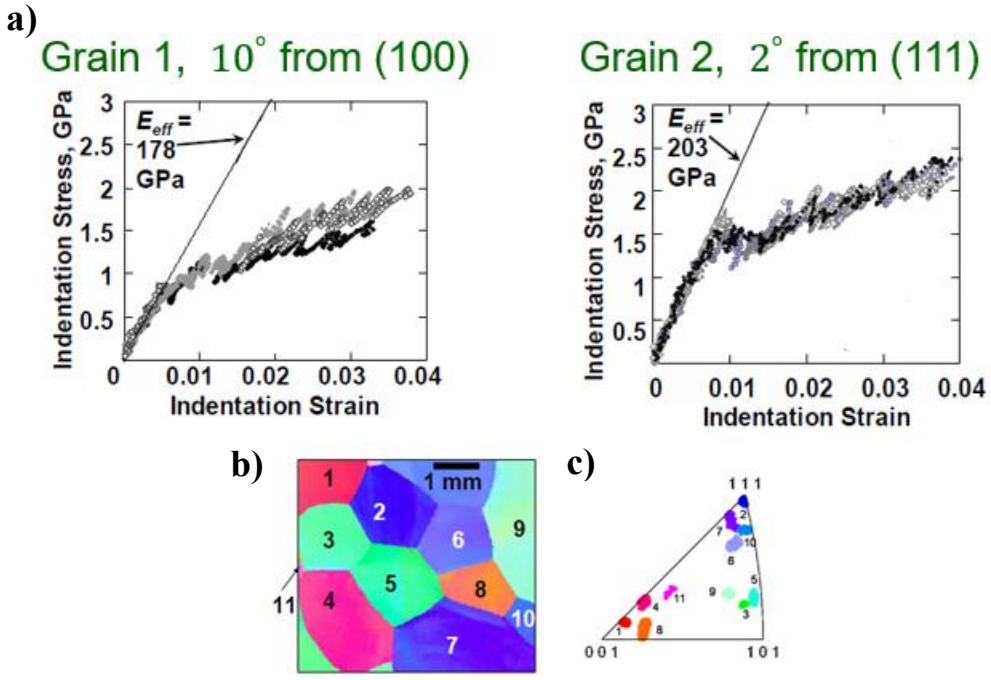

Figure 2.9. Spherical nanoindentation measurements showing the grain-scale elastic-plastic anisotropic. a) ISS curves for Grain #1 and Grain #2. b) Orientation imaging map (OIM) and its corresponding inverse pole figure (IPF).

Further, the ISS curves clearly record the increase in the indentation yield strength after imposing a macroscopic deformation of 30% and 80%. It is shown that the indentation yield strength measured on the ISS curve is sensitive to subtle variation in the local crystal orientation and dislocation density in the primary indentation zone. Indentation stress-strain curves has the capability of quantifying the heterogeneous deformation behavior across the grain boundary regions in polycrystalline high-purity aluminum as shown by Vachhani (Vachhani et al., 2016). The spherical indentation studies on Fe-3% Si and Al demonstrated that microstructure-property relationship can be determined from ISS curves.

CHAPTER 3

CORRELATION OF INDENTATION STRESS-STRAIN CURVES TO UNIAXIAL STRESS-STRAIN CURVES

The stress-strain fields realized in spherical indentation tests are highly heterogeneous, and present a significant challenge to the recovery of bulk stress-strain response such as those measured in simple compression tests performed on sample with a uniform cross section in the gauge section. In this chapter, I critically explore the correlations between indentation stress-strain curves and the simple compression stress-strain curves as illustrated in Figure 3.1 using finite element model of indentation for isotropic elastic-plastic materials obeying J_2 flow theory.

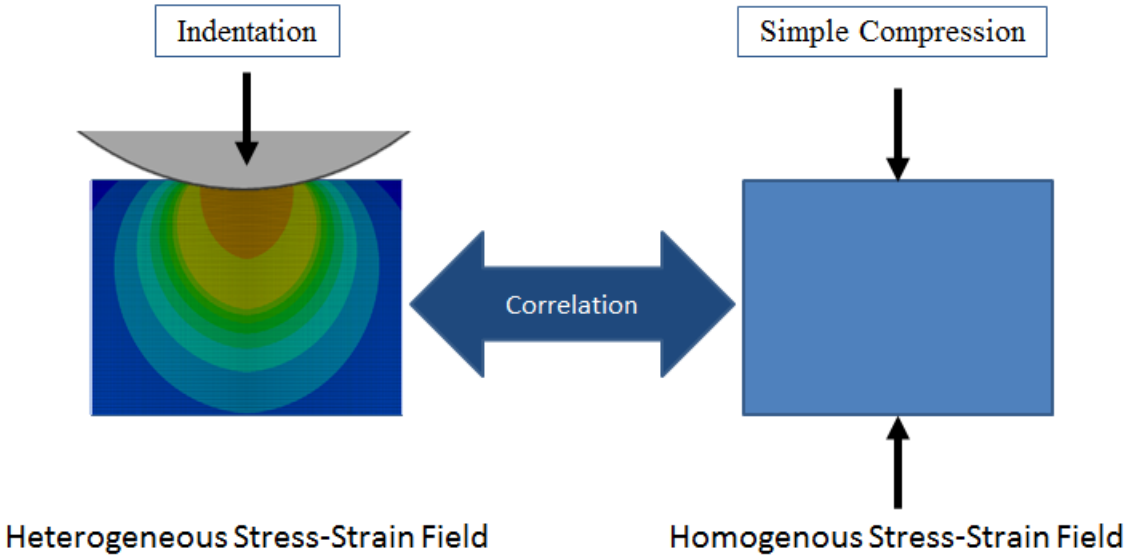

Figure 3.1. Comparing and correlating the stress-state realized in indentation and uniaxial compression tests.

3.1 Introduction

Bulk mechanical properties of materials are typically measured under uniaxial loading conditions such as simple tension or simple compression (ASTM, 2015). However, testing methods for extracting the local properties from exceedingly small sub-volumes of a sample and relate to macroscale properties are still in developmental stages (Gianola and Eberl, 2009; Shan et al., 2008; Uchic et al., 2004; Zhang et al., 2006).

The central issues in the extraction of ISS curves and their correlation to simple compression stress-strain curves revolve around the definitions of the indentation stress and indentation strain measures and their correspondence with stress and strain measures used in simple compression tests. Indentation stress and strain definition stems from Hertz's theory (Hertz, 1896) for frictionless contact between two isotropic elastic solids with spherical surfaces, which may be described as

$$P = \frac{4}{3} E_{eff} R_{eff}^{\frac{1}{2}} h_e^{\frac{3}{2}}, \qquad a = \sqrt{R_{eff} h_e} \tag{3.1}$$

where a is the contact radius at the indentation load, P and h_e is the elastic penetration depth. R_{eff} and E_{eff} denotes the effective radius and the effective modulus of the indenter and the specimen system. In order to convert the measured load-displacement data into ISS curve, one may define the indentation stress and indentation strain such that Hertz's theory, Eq. (3.1), transforms into a linear relationship as

$$\sigma_{ind} = \frac{4E_{eff}}{3\pi} \varepsilon_{ind}, \qquad \sigma_{ind} = \frac{P}{\pi a^2}, \qquad \varepsilon_{ind} = \frac{a}{R_{eff}}. \tag{3.2}$$

Eq. (3.2) has prompted many researchers to adopt some variant of a/R_{eff} as a measure of indentation strain for the more general case of elastic-plastic indentation. In this regard, it is important to note that Eq. (3.2) is strictly valid only for elastic indentations.

As a specific example, a majority of the studies in the literature (Basu et al., 2006; Field and Swain, 1993; Field and Swain, 1995; Herbert et al., 2001; Swain, 1998) have employed the definition of indentation strain as a/R_i for elastic-plastic indentation. As mentioned earlier, a number of recent studies have utilized this measure of indentation strain to correlate indentation stress-strain response to uniaxial stress-strain response of the same material. More specifically, the elastic-plastic transition in indentation is observed to initiate at $1.1\sigma_y$ and plateau at $3\sigma_y$, where σ_y is the uniaxial plastic yield strength of the sample material. However, this definition of indentation strain as a/R_i lacks any physical interpretation as a measure of strain. This is because strain should be fundamentally interpreted as a ratio of the change in length over the initial length of a selected line segment in region of interest in the sample.

Recent development in instrumented indentation techniques (Cordill et al., 2009; Field and Swain, 1993; Li and Bhushan, 2002; Oliver and Pethica, 1989; Oliver and Pharr, 1992; Pathak and Kalidindi, 2015; Pathak et al., 2008; Pathak et al., 2009; Vachhani et al., 2013) have resulted in the ability to probe reliably and consistently the mechanical properties of materials at the microscale. More specifically, as mentioned in the Chapter 2 it is possible to extract suitably normalized indentation stress-strain curves that display an initial linear elastic segment followed by a clear transition to a plastic response. However, relating these ISS curves to stress-strain responses measured in the conventional simple compression tests remains a significant challenge.

A number of other approaches in literature for the recovery of the USS response from the indentation experiments have employed inverse solution methodologies. These approaches utilize sophisticated optimization strategies to minimize a suitably defined

difference (i.e., error metric) between the measured load-displacement curve and the corresponding prediction from the finite element simulation by adjusting the material's constitutive law defined usually as its USS response (Abu Al-Rub and Voyiadjis, 2004; Bucaille et al., 2003; Cheng and Cheng, 1999; Liu et al., 2008; Pelletier, 2006; Raabe et al., 2002). The central deficiency of this approach stems from the fact that the entire elastic-plastic transition occurs over a very short regime in the load-displacement curve. Since it is very difficult to pinpoint this regime exactly in the measured load-displacement curve, it is very difficult to extract reliable properties consistently with such inverse solution methodologies. Indeed, transforming load-displacement curve to ISS curves addresses this problem and provides a much improved opportunity for extracting reliable uniaxial stress-strain curves.

In this chapter, protocols are developed to correlate the ISS curves extracted using the spherical indentation analyses (Donohue et al., 2012; Pathak and Kalidindi, 2015; Pathak et al., 2008; Pathak et al., 2009) and the USS response via simple scaling relationships. The scaling relationships are established and validated in this study using a two-dimensional finite element model for a class of isotropic elastic-plastic materials obeying the J_2 flow theories (Hill, 1948) with linear or saturation type hardening laws. The similarities and differences between these scaling factors and the ones originally used by Tabor (Tabor, 1948) are discussed in detail.

3.2 Finite element model of spherical indentation for isotropic materials

A finite element model of spherical indentation is employed as a surrogate for the experiment in exploring the correlations between ISS and USS responses. For this

purpose, a commercially available finite element code ABAQUS (ABAQUS, 2014) is used. The FE model developed for this study is shown in Figure 3.2a, and is comprised of two axisymmetric two-dimensional isotropic bodies: (i) an elastic-plastic deformable sample with an initially flat surface, and (ii) a rigid hemi-spherical indenter. Four-noded, bilinear, two-dimensional axisymmetric continuum elements (CAX4 in ABAQUS) are used to model the sample in this study. The size of the sample mesh was selected as $20\mu m$ x $20\mu m$ to ensure that it is much larger than the primary indentation zone. The top surface of the indenter is constrained to remain planar, and is allowed to move only normal to the indentation surface. The sample is constrained from moving in the x-direction along the axis of symmetry and along y-direction (indentation direction) at the bottom surface. The sample is discretized into five regions (as shown in Fig. 3.2a.) to achieve highest mesh density in the primary indentation zone (region in the sample with the highest localized deformation).

In the simulations, a vertical displacement boundary condition (along y-direction) is imposed on the node at the center of the indenter which is tied rigidly to entire surface of the indenter. Surface-to-surface contact definition is used to avoid any concentrated force buildup at individual nodes at initial point of contact. Detachment of the two surfaces is allowed to simulate loading-unloading response. The FE model is first validated for purely elastic indentations by comparing the predicted load-displacement curve to predictions from Hertz's theory (Eq. (3.1)). Figure 3.2b demonstrates excellent accuracy of the FE indentation model for purely elastic indentations.

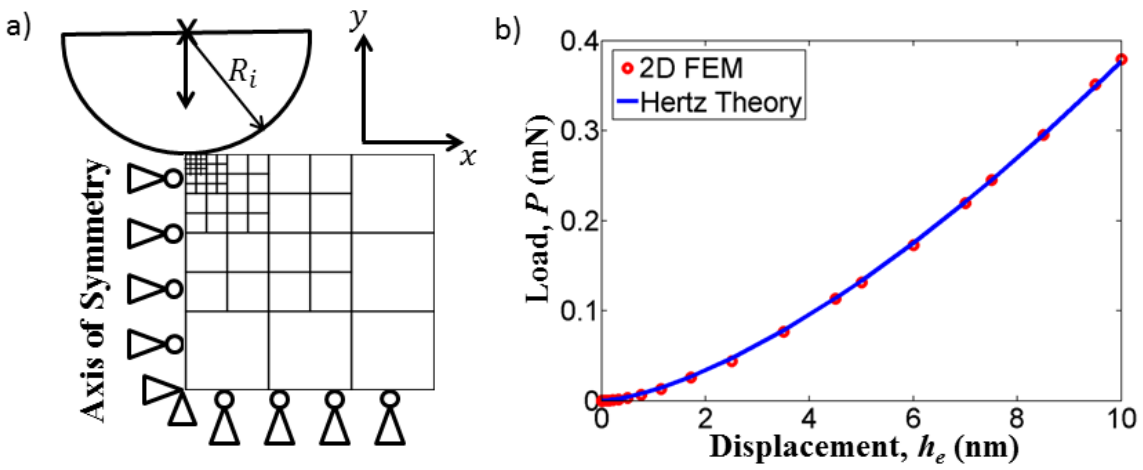

Figure 3.2. a) Schematic of the two dimensional FE mesh (discretized into 5 regions) to simulate isotropic elastic-plastic response under the indenter (axisymmetric boundary conditions applied). b) Load-displacement response compared from FE simulation against Hertz theory for isotropic elastic response.

The load-displacement history extracted from the FE model in multiple elastic-plastic loading-unloading cycles (Donohue et al., 2012) are then used to extract elastic-plastic ISS curves comparable to those extracted from experiments (Pathak et al., 2008; Pathak et al., 2009). For this purpose, we have adopt the following definitions of indentation stress and indentation strain (Kalidindi and Pathak, 2008):

$$\sigma_{ind} = E_{eff}\varepsilon_{ind}, \qquad \sigma_{ind} = \frac{P}{\pi a^2}, \qquad \varepsilon_{ind} = \frac{4}{3\pi}\frac{h_t}{a} \approx \frac{h_t}{2.4a} \tag{3.3}$$

Note that Eq. (3.3) is essentially a rearrangement of Hertz's theory expressed in Eq. (3.1). This particular rearrangement suggests the use of the ratio h_t/a as the definition of indentation strain. The pre-multiplier, $4/3\pi$ in the definition of indentation strain was justified by noting that $2.4a$ corresponds to the depth of the indentation zone (Donohue et al., 2012). This definition of indentation strain allows interpretation of strain measure in the classical sense as the change in length per unit length by idealizing the deformation

under indenter as being equivalent to compressing by h_t (total average indentation depth) a cylindrical sample of radius a and height $2.4a$.

The protocols needed to extract ISS curves from the FE model have been described previously by Donohue et al. (Donohue et al., 2012). A central feature of these protocols is that contact radius is estimated from a partial unloading segment which is assumed to be purely elastic and follow Hertz's theory. Since each unload leads to an estimation of one value of contact radius (in much the same way Tabor did in his experiments), it becomes necessary to conduct a very large number of load-unload steps (as shown in Figure 3.3) in the FE simulation to determine accurately the evolution of the effective radius and the residual depth in the sample.

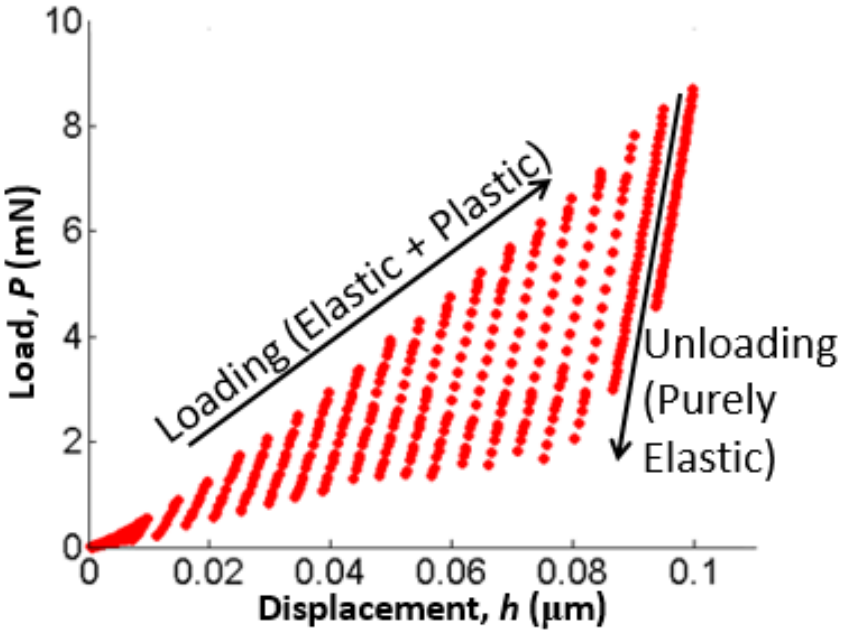

Figure 3.3. Load-displacement curve depicting partial unloads at multiple load levels. The unloading segments are used to compute indentation stress and strain values.

3.3 Scaling relationship between ISS and USS response

This work is aimed at developing robust protocols for recovering the USS curves from the ISS curves. As discussed earlier, this requires the estimation of suitable scaling factors between uniaxial and indentation stresses as well as between uniaxial and indentation strains. Furthermore, we focus on our attention in this study to isotropic elastic-plastic materials, where the plastic response is described by the J_2 flow theory (Hill, 1948).

The strategy for addressing this challenge involves two steps. In the first step, we focus on the scaling factor between uniaxial and the indentation stress through a consideration of the elastic-perfectly plastic indentation response. Because there is no hardening in this case, we expect the ISS curves to plateau at large strains. As a result, we should be able to extract a simple ratio between the plateau stresses in USS and ISS curves.

In the second step, we focus on the scaling factors for uniaxial and indentation strains. In fact, as soon as we establish a scaling factor for the stress (described in the first step above), the scaling factor for the elastic indentation strain can be extracted by matching the ISS curve obtained using Hertz's theory (Eq. 3.3) with the corresponding USS curve (note that for elasticity both these curves are linear). Therefore, we only need to focus on the scaling factor for indentation plastic strain. This can be established from a consideration of indentation response of materials exhibiting linear hardening.

The

central hypothesis is that the scaling factors established using the protocols described above are not strongly affected by the actual hardening behavior exhibited by

the sample material. We critically evaluate our hypothesis by applying the same scaling factors to a sample material exhibiting a completely different hardening response, namely the saturation-type hardening laws. The calibration and validation of these scaling factors are described next.

3.3.1 Scaling indentation stress

Table 3.1 summarizes the material properties used in this study for the elastic-perfectly plastic sample. These cover the typical range of properties exhibited by advanced metals of interest to structural applications. The corresponding ISS curves are generated from the finite element model following the protocols described above (cf. (Donohue et al., 2012)).

Material	Young's Modulus (GPa)	Poisson's Ratio	Yield Strength (GPa)
Soft	70	0.30	0.04
Stiff	400	0.28	0.75

Table 3.1. Elastic and plastic properties used to describe the isotropic sample material behavior used in the present study.

These ISS curves obtained using the FE model and elastic-perfectly plastic material response are shown in Figure 3.4, and show three clearly distinguishable

regimes: (i) an initial elastic regime where the indentation stress evolves linearly with the indentation strain, (ii) an elastic-plastic transition regime that exhibits apparent strain hardening (recall that there is no real hardening of the material in the elastic-perfectly plastic constitutive description) attributed to the transformation of the indentation zone from being dominated by elasticity to one dominated by plasticity, and (iii) a post-yield regime exhibiting the expected perfectly plastic response.

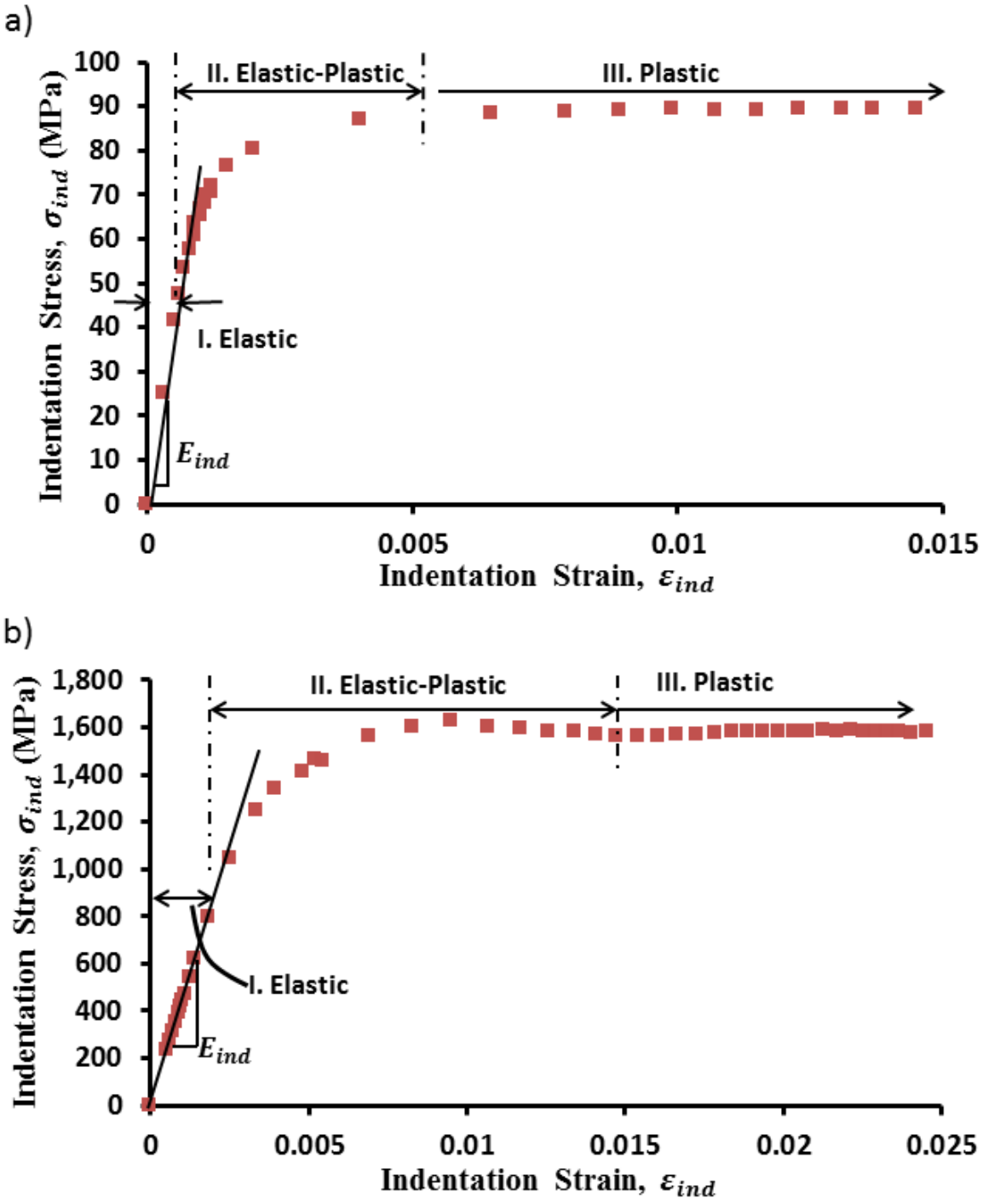

Figure 3.4. FE-generated indentation stress-strain curves for the a) soft and b) stiff materials selected for this study.

Based on the linear elastic solution for stress fields beneath the spherical indenter, initiation of plastic flow following the von-Mises criterion is predicted at an indentation stress of $1.07\sigma_y$ (Johnson, 1987). However, it is important to note that the deviation from elasticity on the ISS happens after a substantial amount of plastic deformation has been realized by the sample as seen in Figure 3.5. The elastic-plastic transition is marked by the fact that the stress fields in the indentation zone have to change from those dominated by elasticity in the first regime to those dominated by plasticity in the final regime. More specifically, the plastic zone underneath the indenter is initially fully surrounded by elastically deforming material. This initial plasticity is therefore heavily constrained until the plastic zone has grown to reach the sample surface (see Figure 3.5). At that point, plasticity occurs relatively easily and this marks the onset of the third regime of a perfectly plastic response in the ISS curves seen in Figs. 3.3 and 3.4. In particular, this transition is most clearly seen through the contour plots of equivalent plastic strain (PEEQ) fields at selected points on the ISS curve in Fig. 3.4. This elastic-plastic transition poses a significant challenge in our efforts to establish a useful correlation between ISS curves and the USS curves.

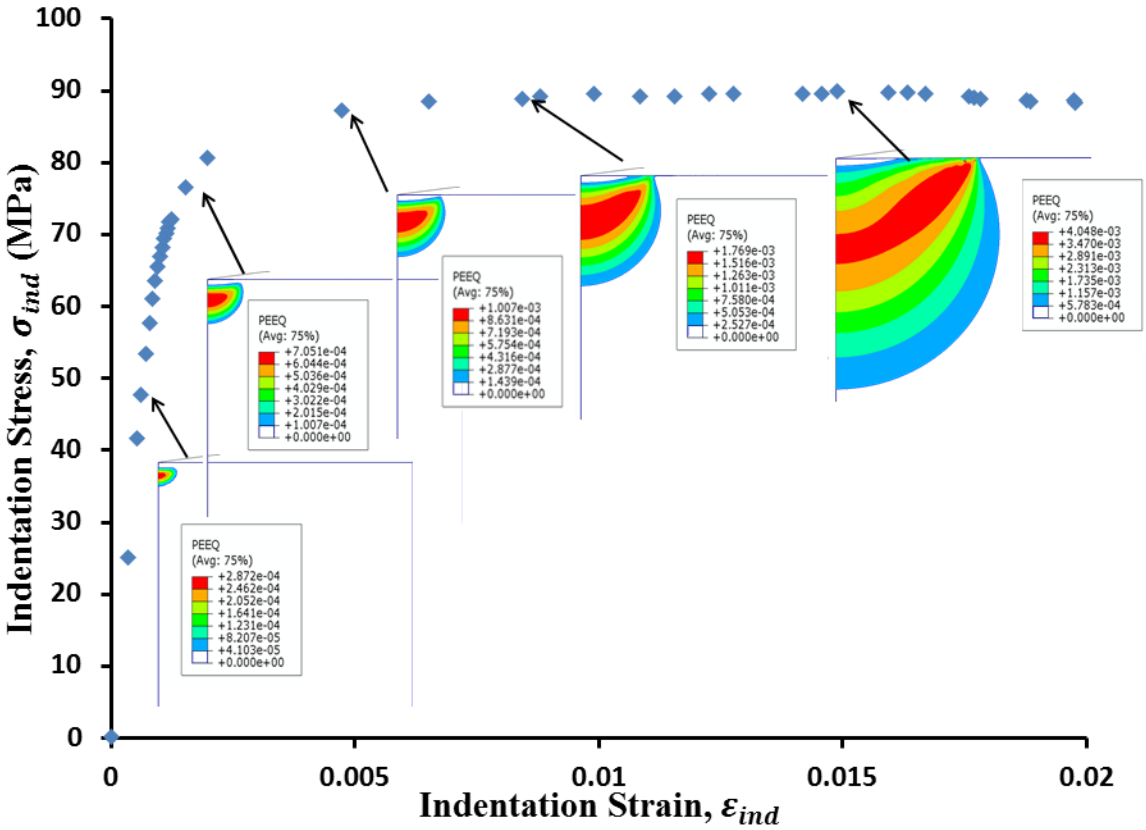

Figure 3.5. Finite element results showing the evolution of plastic zone under the indenter in terms of contours of equivalent plastic strain field (PEEQ) at the corresponding indentation stress (shown for soft material). Note only small subsection of the mesh is shown here.

It should be noted that the ISS curves in Figure 3.6 exhibit some degree of roughness. This, in our opinion, is a consequence of the many numerical computations involved both in the FE simulations (i.e., mesh design, mesh discretization) and the estimation of the contact radius from the analyses of the unloading segments. Our many trials in these simulations have indicated that these numerical oscillations can be alleviated by increasing the mesh density inside the constantly evolving primary indentation zone. However, this improvement is relatively small (and mostly inconsequential for the present study) and incurs a prohibitively high computational cost.

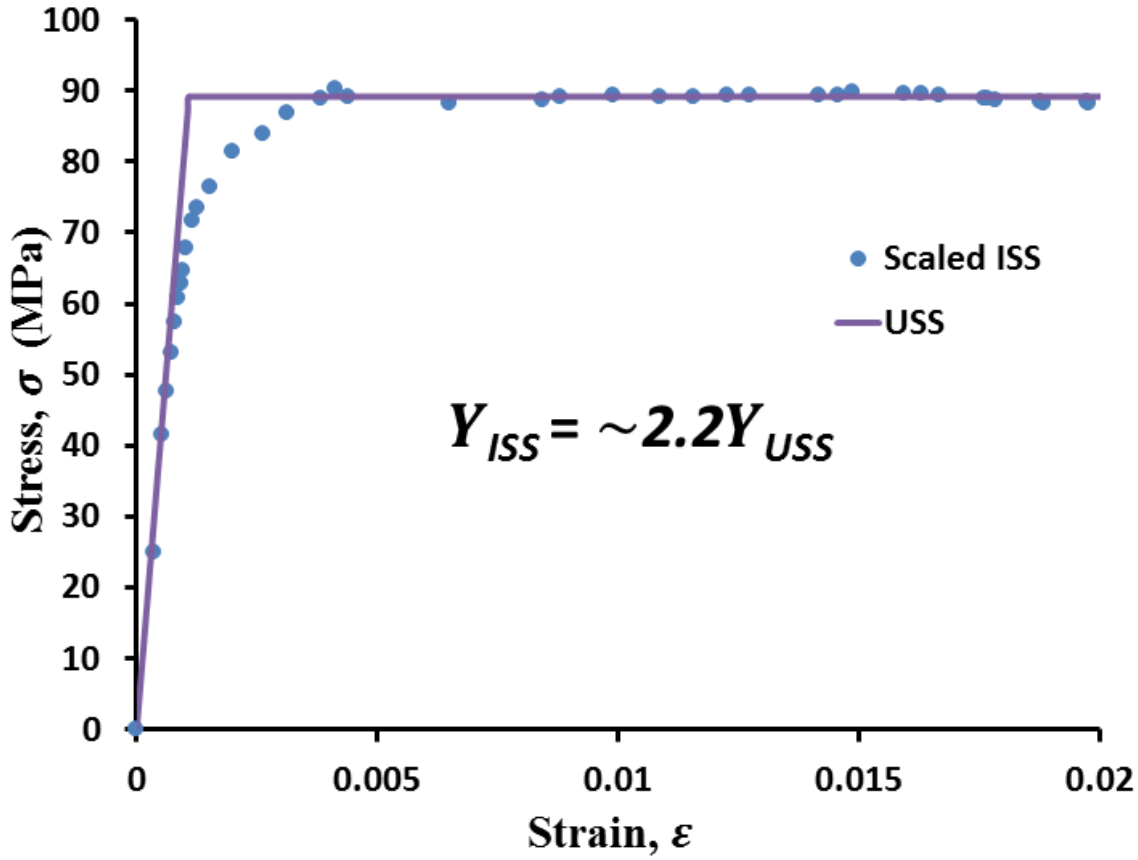

Figure. 3.6. USS curve vs. scaled ISS curve for the soft material (see Table 3.1) exhibiting elastic perfectly-plastic response.

As mentioned earlier, the ability to extract meaningful ISS curves is critical to our goals of extracting a reliable scaling factor between the uniaxial and indentation stresses. This scaling factor is simply the ratio of the indentation stress and the uniaxial stress in the plateau regions of these stress-strain curves. Based on the ISS curves shown in Figure 3.6, this ratio was observed to be in the range of 2.1- 2.2. The correspondence between the scaled ISS curve and the USS curve for the soft material is shown in Figure 3.6 (a similar correspondence was observed for the stiff material as well). In Figure 3.6, the indentation strain was scaled by 2.0, which is established simply using Hertz's theory

(i.e., matching Eqs. (3.1) and (3.3)). In other words, this scaling factor ensures that the elastic portions of the scaled ISS and USS curves would match. However, as mentioned earlier, the plastic strain in the indentation and the uniaxial tests are unlikely to be related by the same factor as the corresponding elastic strains; this will be explored in detail in later case studies that invoke strain hardening.

The stress scaling factor (also called constraint factor) of 2.2 is indeed significantly lower than the previously reported numbers (e.g., the factor of 2.8 reported by Tabor (Tabor, 1951) and Hill (Hill, 1948; Hill et al., 1947; Hill et al., 1989)). The difference is directly attributed to the differences in the definition of the contact radius used in the extraction of the ISS curves. More specifically, the contact radius used in prior studies was either based on the residual indentation left after complete unloading or is defined based on geometrical relationship between the indenter and the sample. In a recent paper (Donohue et al., 2012), we have demonstrated these choices have a significant effect on the estimated values of the contact radius and the subsequent computation of the indentation stress. In the same paper, we have demonstrated that the protocol used in this work provides the most meaningful ISS curves.

As noted earlier, the elastic-plastic transition in the ISS curve is significant in extent and poses a significant challenge in our efforts to correlate the ISS and USS curves. We will revisit this issue later.

3.3.2 Scaling indentation strain

As noted earlier, it is necessary to examine the ISS curves for materials exhibiting hardening to extract a scaling relationship between the indentation plastic strain and the

uniaxial plastic strain. For this purpose, FE indentation simulations were performed for the soft material (see Table 3.1) with different levels of constant strain hardening rates, h_o. In other words, the uniaxial stress-strain behavior of the sample in these simulations is defined to be bi-linear: the first linear segment reflects the purely elastic behavior, and the second linear segment with a slope of h_o reflects a regime of constant strain hardening rate. This bilinear stress-strain description (in the uniaxial stress mode) is provided as input to the FE indentation simulations. The corresponding ISS curves obtained using the protocols described earlier are shown in Figure 3.7.

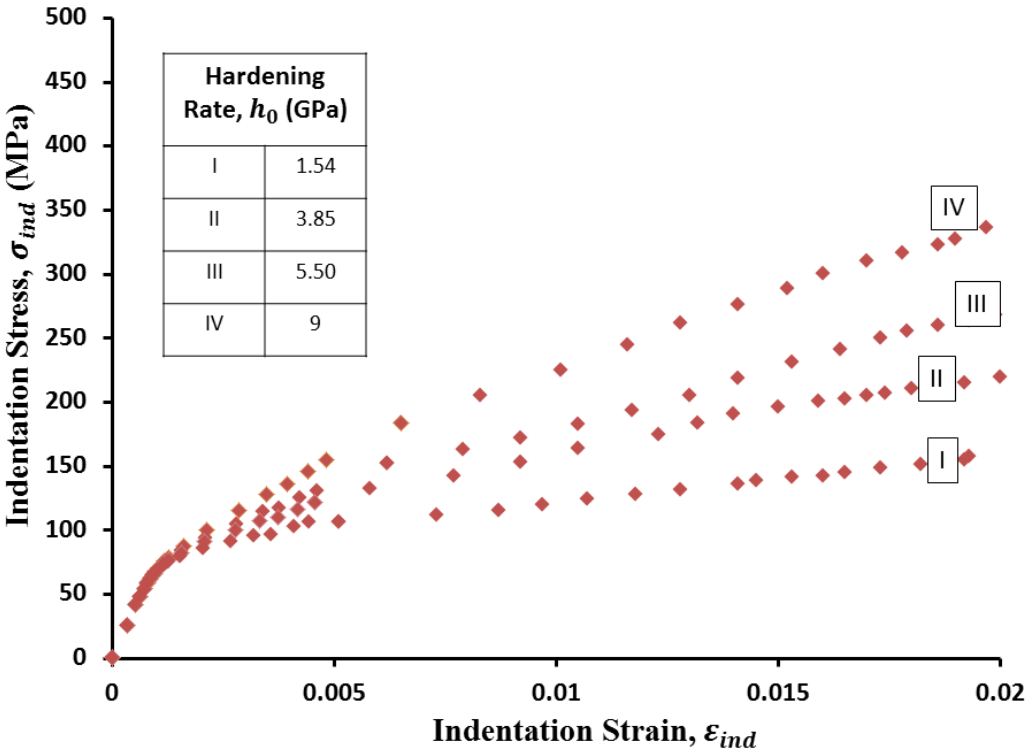

Figure 3.7. Indentation stress-strain curves for soft material (see Table 3.1) depicting linear-hardening behavior for different hardening rates.

It is seen that the ISS curves in the plastic regime exhibit a linear hardening response, except for some oscillations that are fairly characteristic of the numerical instabilities involved in these simulations (as discussed earlier). The fact that the ISS

curves reflect a linear hardening response lends additional support to the validity of the analyses protocols described and employed in this work.

The results presented in Figure 3.7 also suggest that it should be possible to establish a simple scaling factor between the indentation plastic strain and the uniaxial plastic strain. There is, however, no reason to expect that this scaling factor would be the same as the one introduced earlier for the elastic strain. The following set of equations is formulated to describe this equivalence:

$$\varepsilon_{ind} = \varepsilon_{ind}^{e} + \varepsilon_{ind}^{p} = \frac{\sigma_{ind}}{E_{eff}} + \varepsilon_{ind}^{p} \tag{3.4}$$

$$\varepsilon_{sc} = \frac{\varepsilon_{ind}^{e}}{2.0} + \frac{\varepsilon_{ind}^{p}}{\alpha} \tag{3.5}$$

In Eqs. (3.4) and (3.5), ε_{sc} denotes the equivalent simple compression strain corresponding to ε_{ind} and the superscripts e and p refer to the elastic and plastic components, respectively. The value of the scaling factor α was established as ~1.3 by matching the ISS and USS curves for all the FE simulations conducted in this work imposing linear hardening. It is noted here that the scaling factor α established in this study is also the same as the scaling factor for the ratio between the hardening rates in ISS and USS responses reported previously by Donohue et al. (Donohue et al., 2012) and confirmed once again in this study. The corresponding scaled ISS curves are compared with the USS curves in Figure 3.8. It is seen that there is excellent agreement between these curves, except in the elastic-plastic transition regime. As noted earlier, it is very difficult to make a correspondence in this transition regime and we shall revisit this issue later in this paper.

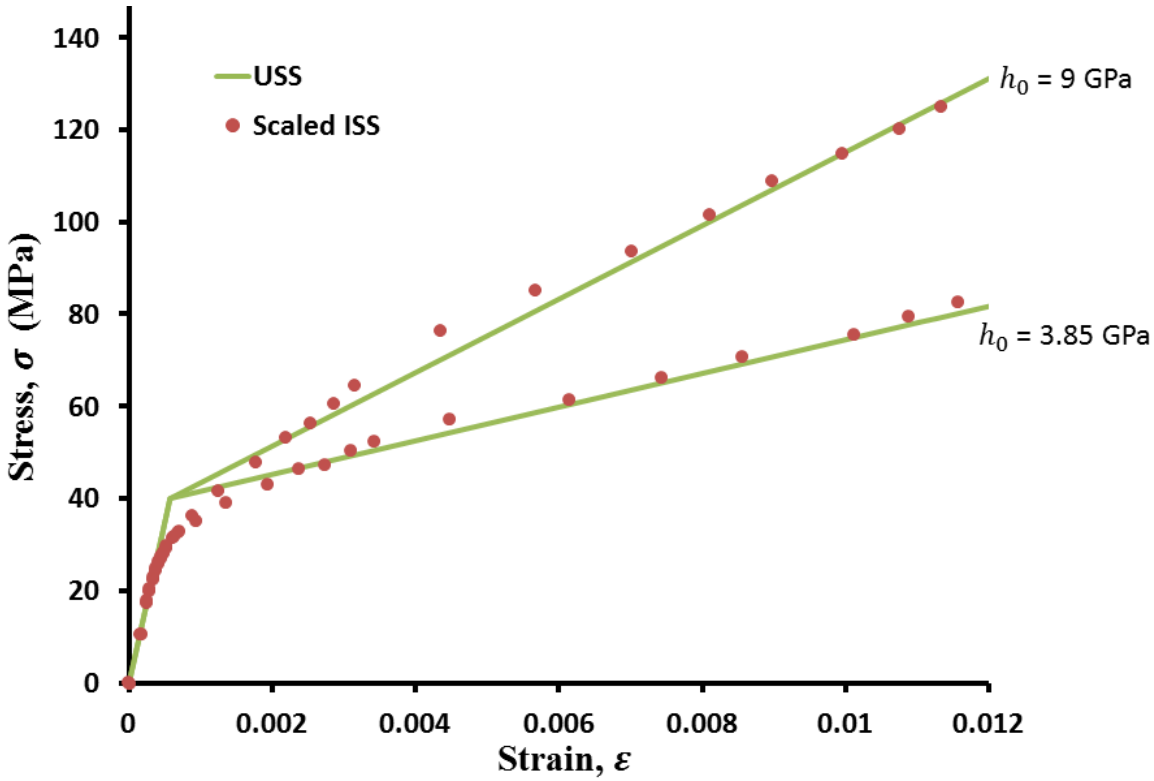

Figure 3.8. USS curve vs. scaled ISS curve for soft material (see Table 1) with different linear strain hardening rates.

3.4 Demonstration of the scaling relationships

As a critical evaluation of the protocols established in the previous section, we examine a material constitutive behavior where the plastic response is described by power-law hardening described as

$$\sigma = \sigma_y + K(\varepsilon^p)^n \tag{3.6}$$

where K and n are the strength coefficient and the strain hardening exponent. For the present case study, we choose two distinct sets of material parameters with different strength coefficients and strain hardening exponents to describe the uniaxial stress-strain behavior of the sample. The material parameters selected are the ones reported for Tantalum ($n = 0.5$ and $K = 562$ MPa) and Aluminum ($n = 0.2$ and $K = 180$ MPa)

(Kalpakjian and Schmid, 2008). These power-law descriptions were provided as input to the FE indentation simulations.

The ISS and USS curves for the selected materials are compared in Figure 3.9. It is seen that scaling protocols described earlier are highly applicable to the both high and low hardening behaviors. This result is significant as the scaling factors were extracted from two very simple hardening laws: (i) perfectly plastic (non-hardening), and (ii) linear hardening, and are observed to provide excellent correspondence in the case of the much more complex saturation-type hardening law used in the validation example. Indeed, the excellent agreement between the scaled ISS and the USS responses, using the scaling factors from the simpler hardening laws, attest clearly to their general applicability to a range of materials behaviors of interest in actual practice.

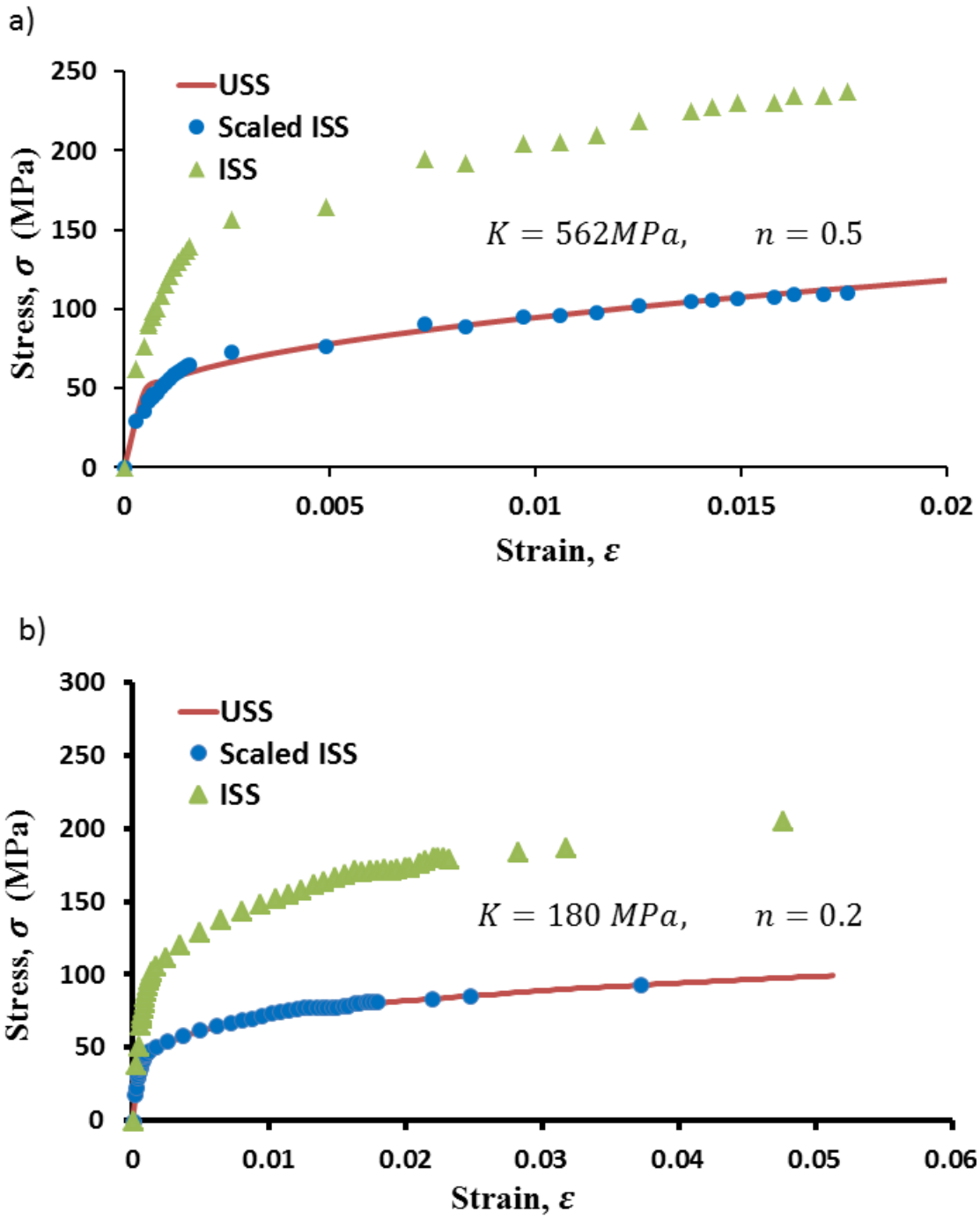

Figure 3.9. Comparison of the ISS, Scaled ISS, and USS responses for materials exhibiting power-law hardening behavior.

3.5 Extracting uniaxial mechanical properties from indentation

As clearly evident from the case studies presented so far, reliable identification of the indentation yield strength is severely compromised by the unavoidable elastic-plastic transition in the indentation test method. Of course, this challenge has long been recognized in prior literature. As a prime example, Herbert et al. (Herbert et al., 2001) explored several alternatives and could not arrive at any conclusive correlation between the uniaxial yield strength and the indentation yield value. Instead, they simply reported a lower limit and an upper limit based on the theoretical Tresca yield criterion ($1.07\sigma_y$) and Tabor's finding (~$2.8\sigma_y$), respectively.

A common and standard approach in defining a yield point is to employ an offset strain. Indeed, a tensile or compressive yield strength is often defined as 0.2% offset yield strength (ASTM, 2015). Close inspection of Figure 3 for the soft and stiff material clearly shows that a fairly large offset is needed if one were to define the indentation yield strength on the plateau region of the ISS curve. However, at the same time, the ISS curves in Figure 3.7 indicate that the value extracted using a high offset is likely to be strongly influenced by the hardening behavior of the material. So, the practical way forward is some form of a compromise on the offset value.

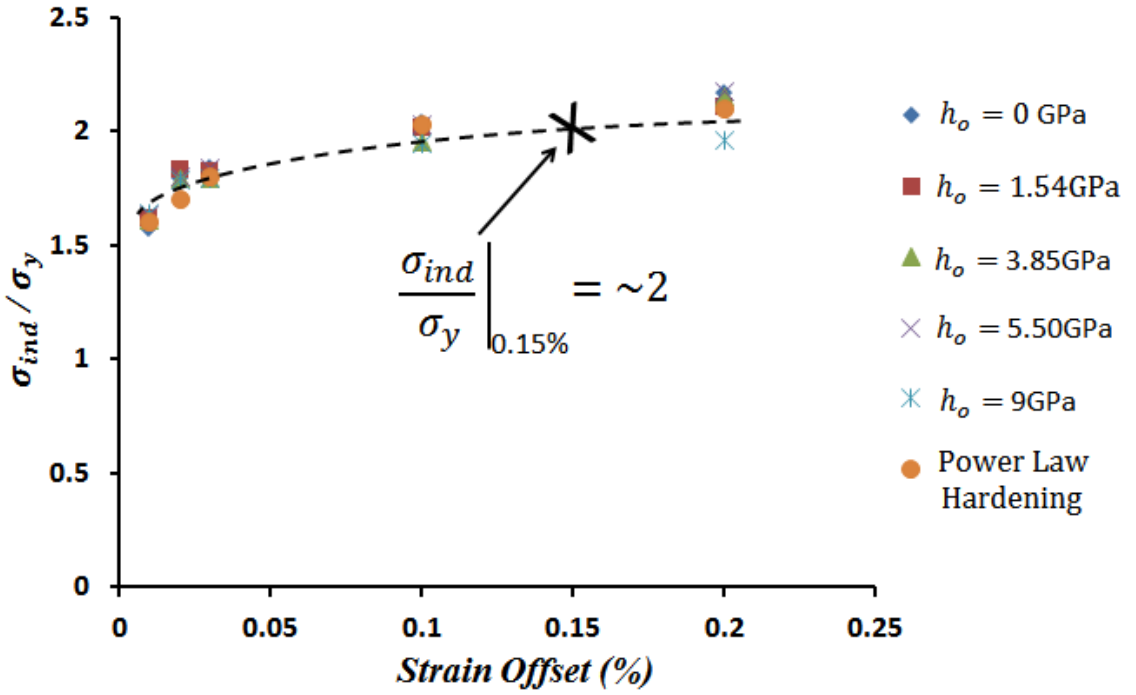

Figure 3.10. Ratio of indentation stress to the 0.2% offset uniaxial yield strength for all FE simulations performed on the soft material.

In order to establish a practically useful offset value of the indentation yield strength, we plotted the offset value indentation stress normalized by the 0.2% offset uniaxial yield strength for different values of the offset in the ISS curves for the FE simulations performed on the soft material in Figure 3.9. Based on this plot, it is clear that this ratio exhibits a plateau (more or less constant value) in the range of 0.1%-0.2% offset in the indentation strain. Also, based on the scaling factors we established earlier between the indentation plastic strain and the uniaxial plastic strain, a 0.2% strain offset for the uniaxial test corresponds approximately to 0.15% offset indentation strain, which falls right in the middle of the plateau seen in the plot in Figure 3.10. Note that Figure 3.10 includes the non-hardening case, the different linear hardening rates, and the power-

law hardening discussed earlier. Consequently, we believe 0.15% offset strain is the best choice for establishing an indentation yield strength for the material. With this definition, the scaling factor for the 0.2% offset yield strength typically recovered from uniaxial stress-strain responses will be 2.0 (see Figure 3.10). In other words, this would be the constraint factor for the offset definition of the yield point.

CHAPTER 4

EXTRACTING SINGLE CRYSTAL ELASTIC STIFFNESS CONSTANTS FROM POLYCRYSTALLINE SAMPLE USING INDENTATION

Development of robust, physics-based, multiscale materials models are largely hampered by lack of validated tools and protocols for characterizing reliably the local (anisotropic) properties at length scales at or below a micron. Although numerical techniques such as the Finite Element Method (FEM) have been shown to be successful in simulating complex interactions between microscale constituents of a composite material system (Anand and Kalidindi, 1994; Bachu and Kalidindi, 1998; Bhattacharyya et al., 2001; Bronkhorst et al., 1992; Haddadi et al., 2006; Kalidindi, 2004; Kalidindi and Anand, 1994; Kalidindi et al., 2004; Kalidindi et al., 1992; Kalidindi and Schoenfeld, 2000; McDowell, 2010; Raabe et al., 2002; Roters et al., 2011; Zhao et al., 2001), their predictive capabilities are strongly affected by the assumptions made about the constitutive laws used to describe the local response of the microscale constituents present in these systems. This chapter describes a new approach for the extraction of the single crystal elastic stiffness parameters from polycrystalline samples using spherical nanoindentation and orientation measurements combined with finite element simulations.

4.1 Introduction

It is often very expensive, and sometimes impossible, to produce sufficiently large volumes of the microscale constituents of interest in their pure form to allow the application of traditional mechanical testing methods (such as compression or tensile testing). One approach explored in literature involves the fabrication of micro-pillars (Li et al., 2011; Shan et al., 2008; Uchic et al., 2004) using focused ion-beam and testing them in a scanning electron microscope. However, this approach requires access to highly sophisticated equipment and is not particularly well suited for extracting the elastic properties of the microscale constituents in composite material systems.

In this work, a new approach for estimating single crystal elastic properties from polycrystalline samples using indentation methods, orientation measurements (by electron back-scattered diffraction), and finite element models is developed. The approach presented here is formulated to solve the following inverse problem: Find the values of the fundamental single crystal elastic stiffness parameters (for a selected material phase) that are most consistent with a set of in-grain indentation measurements obtained on a range of lattice orientations in a polycrystalline sample. This work builds on prior work (Donohue et al., 2012; Kalidindi et al., 2008; Pathak et al., 2008; Pathak et al., 2009; Proust G, 2004) from our research group. As noted above, the challenge posed in the present work is essentially an inverse problem. In the forward direction, it is relatively easy to build a finite element model (Bhattacharya and Nix, 1988; Donohue et al., 2012; Suresh and Giannakopoulos, 1998) that predicts the indentation modulus for a selected crystal lattice orientation and a selected combination of single crystal elastic stiffness parameters. Such finite element models are not ideally suited for addressing the

inverse problem stated above. A new approach is introduced for addressing the inverse problem described above, which is built on the compact Fourier representations used extensively in our prior work in the development of the microstructure sensitive design (MSD) framework (Adams et al., 2012; Kalidindi, 2004; Li et al., 2003). This new approach is developed and presented first in a general framework that is applicable to any crystal lattice symmetry.

4.2 Elastic anisotropy in indentation

Spherical nanoindentation data analyses procedures are largely based on Hertz's theory (H., 1896; Johnson and Johnson, 1987; Willis, 1966) which assumes frictionless, elastic, contact between two isotropic quadratic surfaces. The main result of this theory can be expressed as

$$P = \frac{4}{3} E_{eff} R_{eff}^{\frac{1}{2}} h_e^{\frac{3}{2}} \tag{4.1}$$

where P is the indentation load at the elastic penetration depth, h_e. R_{eff} and E_{eff} denote the effective radius and the effective indentation modulus of the sample and the indenter system, defined as

$$\frac{1}{E_{eff}} = \frac{1-\upsilon_s^2}{E_s} + \frac{1-\upsilon_i^2}{E_i}, \qquad \frac{1}{R_{eff}} = \frac{1}{R_s} + \frac{1}{R_i} \tag{4.2}$$

In Eq. (4.2), E and ν denote the Young's modulus and Poisson's ratio of the indenter (subscript *i*) and the specimen (subscript *s*), and R denotes the radius. In the purely elastic indentation of a perfectly flat surface, $R_{eff} = R_i$.

Although the theory for elastic indentation of isotropic materials is well established, it is not directly applicable to most in-grain nanoindentation studies on

polycrystalline materials since the indentation zone size in such measurements is typically much smaller than the grain size in the sample. At this length scale, most crystalline materials exhibit significant anisotropy in their elastic response. A number of different approaches have been explored in literature (Cammarata et al., 1990; Farthing et al., 1988) to take the elastic anisotropy into account in the analyses of the indentation measurements. Vlassak and Nix (Vlassak et al., 2003; Vlassak and Nix, 1993, 1994) have developed a rigorous analytical framework based on Hertz theory to address the elastic indentation of anisotropic samples. Their theory indicates that the inclusion of a crystal lattice orientation dependent parameter, β, into the definition of the effective indentation modulus will adequately capture the anisotropic elastic indentation response of cubic crystals for any arbitrary orientation of the crystal lattice in the indentation zone. More specifically, they suggest

$$\frac{1}{E_{eff}} = \beta\left(\frac{1-\upsilon_s^2}{E_s}\right) + \left(\frac{1-\upsilon_i^2}{E_i}\right), \tag{4.3}$$

where E_s and ν_s denote the effective Young's modulus and Poisson's ratio, respectively (Vlassak and Nix, 1993, 1994), for a randomly textured polycrystalline sample.

4.3 FE model of spherical indentation for elastic anisotropic materials

The first goal is to establish the underlying features of Vlassak and Nix (Vlassak and Nix, 1993, 1994) theory that are central to the indentation analyses protocols discussed here. More specifically, Eq. (4.3) combined with Eq. (4.1) implies that the indentation load, P, continues to be directly proportional to $h_e^{3/2}$, even with anisotropic elastic response of the sample. For establishing whether or not an indentation modulus

can be defined for any crystal lattice orientation (from the expected linear relationship between P and $h_e^{3/2}$), we developed and employed a finite element model.

The three-dimensional finite element (FE) model to simulate elastic spherical indentation of anisotropic crystals was produced using the commercial finite element code ABAQUS (ABAQUS, 2014). The finite element model developed for this study is comprised of two three-dimensional bodies: (i) an elastically deformable sample with an initially flat surface discretized into ~57,000 eight-noded, three-dimensional, continuum (C3D8) elements, and (ii) a rigid hemi-spherical indenter of radius 13.5μm (size of the indenter in prior experimental studies in our group). The size of the sample was selected as 18μm x 18μm x 9μm to ensure that it is much larger than the typical indentation zone size (observed to be about ~1.2μm from our simulations). The sample has been discretized into seven regions as shown in Fig. 4.1a to permit the use of a progressively higher mesh density as we approach the indentation zone directly below the indenter-sample contact surface. Discretizing the mesh in this manner allowed us to capture the stress and strain fields to sufficient accuracy while keeping the total number of elements in the FE model (as well as the computational cost) relatively low. Significant computational resources were required and utilized to keep the runtime to just under ~30 minutes per simulation. The FE simulations described in this work were executed on 2 nodes (32 cores per node) provided by Trestles (part of XSEDE supercomputing facility). A hard surface-to-surface, frictionless, contact definition was used to model the contact behavior between the indenter (master) surface and the elastically deformable sample (slave) surface.

Displacement boundary conditions in the z-direction were imposed on the reference node (placed at the center of the indenter), which is tied rigidly to the entire surface of the indenter. The top surface of the sample was free to move while the bottom surface of the sample was constrained along the z-direction (indentation direction). The inputs to the FE model are the single crystal elastic stiffness constants of the material of interest in the crystal frame (i.e., C_{11}, C_{12}, and C_{44}) and the crystal lattice orientation, (Φ, φ_2).

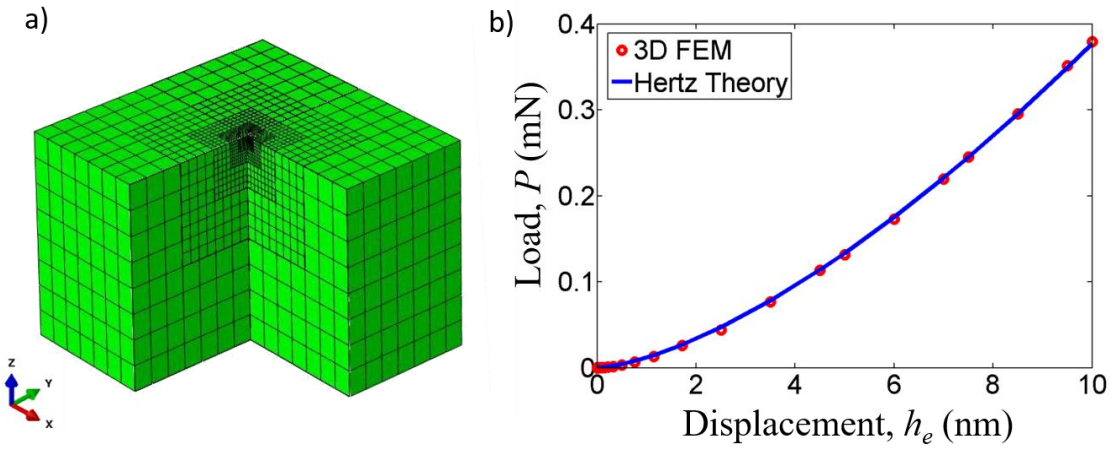

Figure 4.1. a) The 3-D FE mesh used to simulate elastic anisotropic response under the indenter (isometric view of the region under the indenter tip). b) Load-displacement response of FE simulation vs. Hertz theory for the isotropic response case.

Finite displacement in the z-direction was imposed on the indenter and the corresponding total reaction force exerted by the slave surface on the indenter is predicted and used to determine the effective indentation modulus of the sample. The finite element model developed in this study was validated by comparing the simulated

load-displacement curves against the analytical prediction from Hertz's theory for purely isotropic elastic deformation (see Fig. 4.1b). Additionally, a detailed sensitivity study was conducted to ensure that the details of the mesh and the details of the far-field boundary conditions did not influence significantly the predicted load-displacement response.

The finite element model developed in this study was validated by comparing the predicted indentation modulus against the analytical expression reported by Vlassak and Nix (Vlassak and Nix, 1994) in Table 4.1.

Material and corresponding elastic constants (GPa)	Orientation Direction *(h,k,l)*	Theoretical E_{ind} (GPa)	FE Prediction E_{ind} (GPa)
Aluminum$^{\curlywedge}$ C_{11} =107.3 C_{12} = 60.90 C_{44} = 28.3	(100)	79	78.96
	(110)	80	80.93
	(111)	81	80.25
Copper$^{\curlywedge}$ C_{11} = 170.2 C_{12} = 114.9 C_{44} = 61.0	(100)	129	129.65
	(110)	138	137.19
	(111)	141	141.05
β -Brass$^{\perp}$ (CsCl) C_{11} = 126.5 C_{12} = 107.7 C_{44} = 80.3	(100)	95	93.87
	(110)	112	109.40
	(111)	117	115.47

$^{\perp}$ Taken from Vlassak and Nix
$^{\curlywedge}$ Taken from Simmon and Wang

Table 4.1. Indentation moduli values for the cubic crystals predicted from Finite Element model and theoretical values reported in Vlassak and Nix for selected orientations.

It is clear that the finite element predictions are in excellent agreement with the theoretically expected values. Furthermore, the FE models predicted that a linear relationship between P and $h_e^{3/2}$ holds for the anisotropic elastic indentations, in full accord with the theories presented by Vlassak and Nix (Vlassak and Nix, 1993, 1994). Some examples of the FE predicted load–displacement relations are presented in Fig. 4.2.

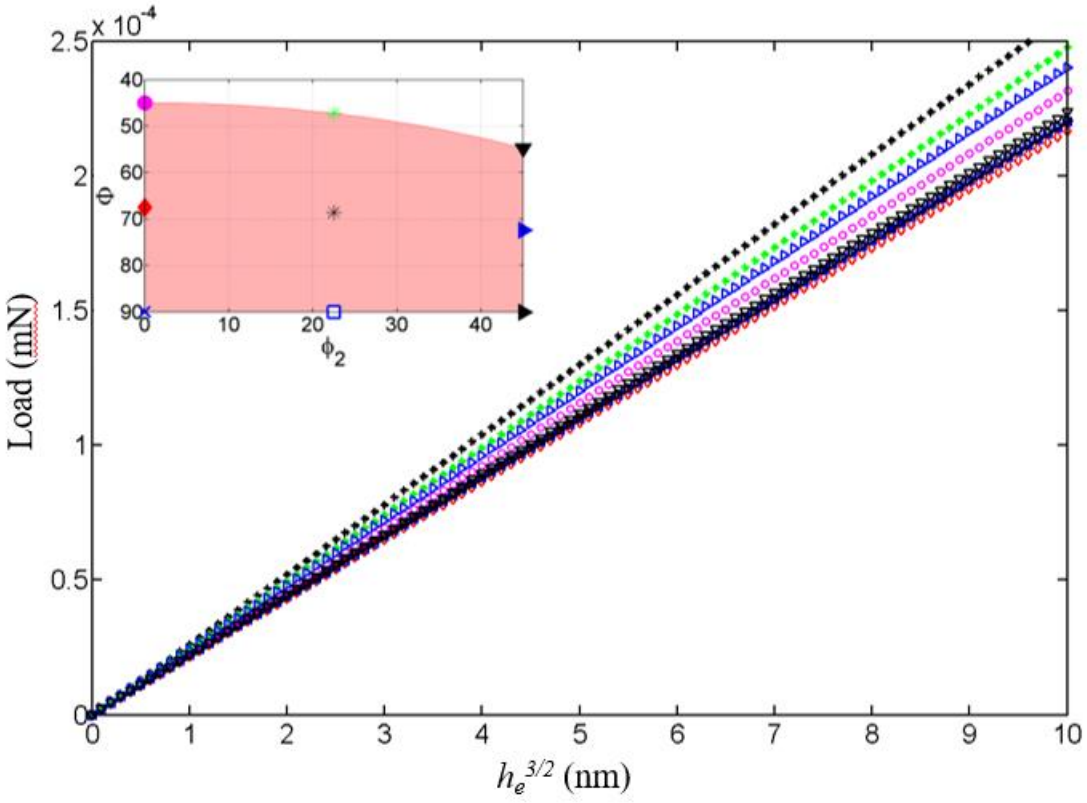

Figure 4.2. P vs. $(h_e)^{(3/2)}$ plots obtained for indentation of copper in different crystal orientations spread over the cubic-transversely isotropic FZ (highlighted area in the subplot).

Since this relationship holds true for any arbitrary orientation of the crystal, then it allows us to extract an orientation dependent indentation modulus (the parameter β is

expected to be orientation dependent) from the indentation measurement on any crystal in the sample.

4.4 Protocols to estimate single crystal elastic constants

In this section, we present the proposed approach as a general framework. In the next section, we demonstrate a specific application and provide many more details of the computations involved.

4.4.1 Spectral representation of indentation modulus

The first step of the proposed protocol involves establishing the functional dependence of the effective indentation modulus on the single crystal elastic constants and the crystal lattice orientation. In order to establish this functional dependence, a large number of data points can be accumulated from the finite element model predictions. Each FE simulation provides one data point which is an estimate of the indentation modulus for a specific combination of one crystal orientation and one set of values for the elastic constants.

A least-squares fit between the FE predicted values of P and $h_e^{3/2}$ in each simulation yields an estimate of the indentation modulus (E_{ind}) (see Eq. (1)). Implicitly, the indentation modulus so obtained depends on the crystal lattice orientation (applied here uniformly to all elements in the sample) and the values of the single crystal elastic constants used for the sample material (e.g., C_{11}, C_{12}, and C_{44} for cubic crystals) (Simmons and Wang, 1971). Therefore, the different measurements on the differently oriented grains in the polycrystalline sample can be interpreted as results of probing single crystals of a selected phase through indentations in different crystallographic

directions. The functional dependencies of the indentation modulus described above can therefore be succinctly expressed as $E_{ind}(g, C_{11}, C_{12}, C_{44})$.

The first goal is to capture this functional dependence of the indentation modulus using highly efficient spectral representations. In this paper, we have employed the spherical surface harmonics (SSH) (H, 1982) denoted as K_l^m(g) to serve as a Fourier basis for compact representation of this function over the orientation space of interest. The advantages and compactness of using basis functions on the orientation space have already been discussed in our prior publications (Fast et al., 2008; Fullwood et al., 2010). For the variables denoting the elastic stiffness constants, we explore here the use of Legendre polynomials, $P_n(\,)$ (Copson, 1950) as Fourier basis. Note that the Legendre polynomials form a Fourier basis over the range [-1,+1], and therefore the stiffness parameters need to be suitably rescaled. Each rescaled elastic stiffness constant can be defined as

$$\tilde{C} = \frac{2C - C_{min} - C_{max}}{C_{max} - C_{min}} \tag{4.4}$$

where C_{min} and C_{max} are the respective minimum and maximum values for the specific elastic stiffness constant. The function of interest, $E_{ind}\left(g, \tilde{C}_{11}, \tilde{C}_{12}, \tilde{C}_{44}\right)$ is then expressed as

$$E_{ind}\left(g, \tilde{C}_{11}, \tilde{C}_{12}, \tilde{C}_{44}\right) = \sum_{l=0}^{\infty} \sum_{m=1}^{M(l)} \sum_{q,r,s=0}^{\infty} A_l^{mqrs} K_l^m(g) P_q\left(\tilde{C}_{11}\right) P_r\left(\tilde{C}_{12}\right) P_s\left(\tilde{C}_{44}\right) \tag{4.5}$$

In Eq. (4.5), A_l^{mqrs} represent the Fourier coefficients. The function $M(l)$ denotes the number of terms needed in the enumeration of index, *m*; these numbers are a function of the index *l* and are determined by crystal symmetries (H, 1982).

The most common approaches used in literature for establishing the Fourier coefficients generally exploit the orthonormal properties of the Fourier basis (Adams et al., 2012; Kalidindi et al., 2006; Kalidindi et al., 2008; Knezevic et al., 2009). However, such approaches require evaluation of the function at an extremely large number of locations in the compounded space of the complete ranges of all the independent variables involved. Since the function evaluation here is being attempted through a computationally expensive finite element model, the traditional approach of establishing Fourier coefficients is not very practical for the present problem. Consequently, we explore in this work an approach for establishing the values of the Fourier coefficients in Eq. (4.5) using Ordinary Least Squares (OLS) regression analysis. In order to use a regression technique, it is necessary to truncate the Fourier series in Eq. (4.5) to a finite number of terms in the expansion. Simplifying the notation a little, Eq. (4.5) can be expressed as

$$E_{ind}\left(g, \tilde{C}_{11}, \tilde{C}_{12}, \tilde{C}_{44}\right) \approx \sum_{L=0}^{\tilde{L}} \sum_{q,r,s=0}^{\tilde{q}} A_L^{qrs} K_L\,(g) P_q\left(\tilde{C}_{11}\right) P_r\left(\tilde{C}_{12}\right) P_s\left(\tilde{C}_{44}\right) \tag{4.6}$$

where L enumerates each distinct combination of (m, l) in the SSH series expansion, and $\tilde{L}$ and $\tilde{q}$ denote the truncation limits in the SSH and the Legendre polynomial expansions. Note also that a single limit was selected in Eq. (4.6) for all three Legendre polynomial bases used in this equation. This was merely done for simplicity here, and different limits can be selected for the different variables as needed in any specific application.

As described earlier, each FE simulation of the indentation produces one discrete data point for a combination of one crystal orientation and one set of values for the cubic elastic stiffness constants. Consider a dataset with N such data points collected from

multiple runs of the FE simulations for different combinations of crystal orientations and cubic elastic stiffness constants. Such a FE generated dataset can be denoted as $\left\{\left(E_{ind}^{FE\ (n)}, g^{(n)}, \tilde{C}_{11}^{(n)}, \tilde{C}_{12}^{(n)}, \tilde{C}_{44}^{(n)}\right), n = 1, 2, \ldots, N\right\}$. Regression analysis is then formulated as a minimization of the difference (sum of the squares of the residual) between the FE generated dataset and the truncated Fourier representation shown in Eq. (6). In other words, OLS (Bishop, 2006; Press, 2007) aims to solve the following minimization problem:

$$\min_{A_L^{qrs}} \left(\sum_{n=1}^{N} \left| E_{ind}^{FE\ (n)} - \sum_{L=0}^{\tilde{L}} \sum_{q,r,s=0}^{\tilde{q}} A_L^{qrs} K_L\left(g^{(n)}\right) P_q\left(\tilde{C}_{11}^{(n)}\right) P_r\left(\tilde{C}_{12}^{(n)}\right) P_s\left(\tilde{C}_{44}^{(n)}\right) \right|^2 \right) \quad (4.7)$$

Note that the values of the Fourier coefficients established using the regression method described above can be sensitive to the truncation levels used, i.e., the values of $\tilde{L}$ and $\tilde{q}$. Since we do not generally know a priori the right values of $\tilde{L}$ and $\tilde{q}$ in any specific application, this approach needs a few repeated trials. Although higher values of $\tilde{L}$ and $\tilde{q}$ will generally produce a lower error (difference between the FE dataset and the fitted Fourier expansion), they may also result in over-fitting of the dataset. Over-fitting needs to be avoided as it will likely produce unreliable estimates in subsequent application of the Fourier function (especially for new data points not included in the calibration dataset).

In order to track the potential for over-fitting of the Fourier coefficients obtained at each level of truncation (i.e., selection of $\tilde{L}$ and $\tilde{q}$), leave-one-out-cross validation (LOOCV) can be employed (Çeçen et al., 2014). LOOCV allows an objective selection of the truncation levels by establishing the fit N times (this is size of the dataset), while

leaving one data point out of the regression each time. In doing so, LOOCV will quantify the contribution of each data point to the Fourier coefficients established in each regression. Given a large N, for an over-fitted Fourier expansion, the exclusion of a single data point will cause significant change in the coefficients, whereas for a good fit this change will be negligible. In order to quantify the robustness of the fit, the following objective measures could be utilized:

I. Mean absolute error of the fit, $\bar{e}$, defined as

$$\bar{e} = \frac{1}{N}\sum_{n=1}^{N}\left|e^{(n)}\right| = \frac{1}{N}\sum_{n=1}^{N}\left|E_{ind}^{FE\ (n)} - \sum_{L=0}^{\tilde{L}}\sum_{q,r,s=0}^{\tilde{q}} A_L^{qrs} K_L\left(g^{(n)}\right) P_q\left(\tilde{C}_{11}^{(n)}\right) P_r\left(\tilde{C}_{12}^{(n)}\right) P_s\left(\tilde{C}_{44}^{(n)}\right)\right| \tag{4.8}$$

Median absolute deviation (MAD) of error of the fit as

$$MAD_e = \text{Median}\left(\left|e^{(n)} - \text{Median}\left(e^{(1)}, e^{(2)}, \ldots, e^{(N)}\right)\right|\right), \quad n = \{1,2,..,N\} \tag{4.9}$$

I. Mean absolute error of LOOCV, $\bar{e}_{CV}$, and MAD of LOOCV, MAD_{CV}, defined analogously as the mean and median of the error for the test data point in each of the *N* repeated fits.

The two measures of error of fit defined above will show improvement of fit with higher values of $\tilde{L}$ and $\tilde{q}$, whereas the two measures of error of LOOCV are expected to show a decline in robustness of fit with higher values of $\tilde{L}$ and $\tilde{q}$ accounting for over-fit of data. Therefore, a compromise is often made in choosing the best fit based on the values of all four measures defined above. In the next step, Eq. (4.6) can be used to address the inverse problem of estimating the unknown single crystal elastic stiffness constants for a selected phase in a polycrystalline sample.

4.4.2 Protocol to extract single-crystal elastic constants

As described earlier, developing and validating an inverse solution methodology to extract grain scale elastic properties for a selected materials phase in a polycrystalline material is the main objective of this work. The protocol described here aims to match the measurements of a set of indentation moduli on differently oriented grains (typically measured using Orientation Imaging Microscopy (Proust G, 2004)) of a selected phase whose independent elastic stiffness constants are unknown (denoted as C^*) with the function established in the previous step (Eq. (4.6)). For cubic materials, for simplicity of notation, let $(\tilde{C}_1^*, \tilde{C}_2^*, \tilde{C}_3^*)$ correspond to rescaled unknown elastic constants $(\tilde{C}_{11}^*, \tilde{C}_{12}^*, \tilde{C}_{44}^*)$ using Eq. (4.4). Let $\{g^{(j)}, j = 1, 2, \dots J\}$ denote the specific orientations where the indentation measurements were made, and $E_{ind}^{(j)}$ denote the corresponding measurements of the indentation moduli. Let the corresponding theoretical value for each of the measurement, predicted from the Fourier representation (Eq. (4.6)) be denoted as, $E_{ind}^{(j)*}(g^{(j)}, \tilde{C}_1^*, \tilde{C}_2^*, \tilde{C}_3^*)$. The task of estimating the unknown single crystal elastic constants then reduces to minimizing the difference between the values of $E_{ind}^{(j)*}(g^{(j)}, \tilde{C}_1^*, \tilde{C}_2^*, \tilde{C}_3^*)$ and $E_{ind}^{(j)}$ for all of the available measurements on the selected material phase. The corresponding minimization problem can be expressed as

$$\min_{\tilde{C}_1^*, \tilde{C}_2^*, \tilde{C}_3^*} f\left(\tilde{C}_1^*, \tilde{C}_2^*, \tilde{C}_3^*\right) = \min_{\tilde{C}_1^*, \tilde{C}_2^*, \tilde{C}_3^*} \sum_{j=1}^{J} [E_{ind}^{(j)} - E_{ind}^{(j)*}(g^{(j)}, \tilde{C}_1^*, \tilde{C}_2^*, \tilde{C}_3^*)]^2 \tag{4.10}$$

The above minimization problem can be addressed by evaluating and equating the relevant derivatives of the function to zero:

$$F_i\left(\tilde{C}_1^*, \tilde{C}_2^*, \tilde{C}_3^*\right) = \frac{\partial f}{\partial \tilde{C}_i^*}$$

$$= -2\sum_{j=1}^{J}\left[E_{ind}^{(j)} - E_{ind}^{(j)*}\left(g^{(j)}, \tilde{C}_1^*, \tilde{C}_2^*, \tilde{C}_3^*\right)\right]\frac{\partial E_{ind}^{(j)*}\left(g^{(j)}, \tilde{C}_1^*, \tilde{C}_2^*, \tilde{C}_3^*\right)}{\partial \tilde{C}_i^*} \quad (4.11)$$

$$= 0.$$

The system of nonlinear equations in Eq. (4.11) can be solved using various numerical approaches. In this paper, we have employed an iterative Newton-Raphson algorithm to solve this system of non-linear equations. This approach can be summarized as

$$\tilde{C}_i^{*(k+1)} = \tilde{C}_i^{*(k)} - \left[J_{ij}\right]^{-1} F_j$$
$$J_{ij} = \left.\frac{\partial F_i}{\partial \tilde{C}_j^*}\right|_{\tilde{C}_n^* = \tilde{C}_n^{*(k)}} \quad (4.12)$$

where the superscript *(k)* denotes the iteration number.

5. Case study: polycrystalline as-cast Fe-3%Si

The new protocols presented in this paper to extract the single crystal elastic stiffness parameters have been applied to an as-cast polycrystalline sample of Fe-3%Si. As described in the previous section, the first step involves establishing the function $E_{ind}\left(g, \tilde{C}_{11}, \tilde{C}_{12}, \tilde{C}_{44}\right)$ in a spectral form (see Eq. (4.6)) using regression methods on datasets assembled from results produced by the FE models described in Section 3. As described earlier, each FE simulation of the spherical indentation for a selected combination of crystal orientation and cubic elastic stiffness parameters, yields one data point. In the present example, the desired dataset was accumulated by executing a total of 2700 FE simulations that employed 300 distinct sets of the cubic elastic stiffness

constants (Simmons and Wang, 1971) compounded with nine distinct crystal orientations. The elastic stiffness constants were selected in the ranges of $50 \leq C_{11} \leq 250$, $40 \leq C_{12} \leq 150$, and $15 \leq C_{44} \leq 125$ (see Fig. 4.3), which were chosen so that they cover the typical ranges for most structural cubic metals and alloys of interest. This set covers a cubic anisotropy ratio, defined as $A = 2C_{44}/(C_{11} - C_{12})$, in the range $(0 < A < 8)$.

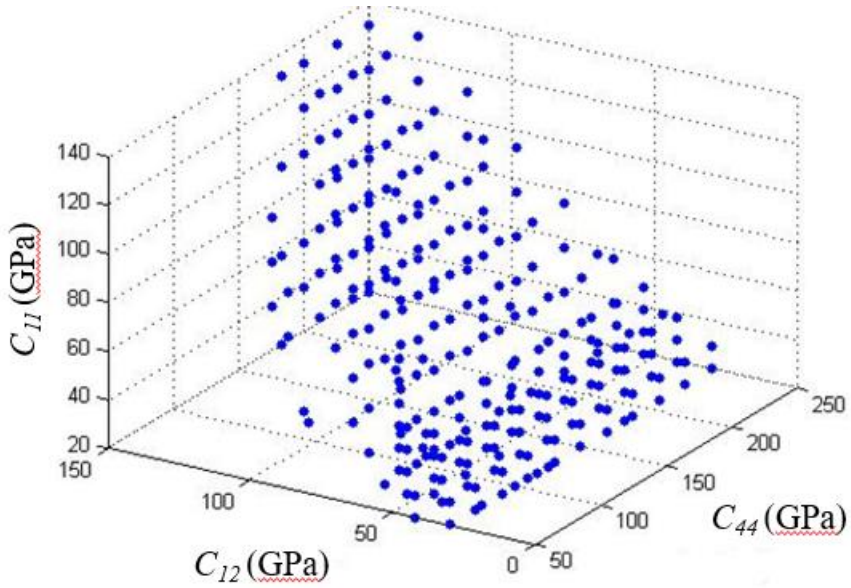

Figure 4.3. 300 distinct sets of independent elastic stiffness constants (C_{11}, C_{12}, C_{44}) used in the present study to establish the spectral representations.

The crystal orientations were selected such that they cover the relevant fundamental zone (FZ) of orientations of interest for the present application (Adams et al., 2012) (see the inset of Figure 4.2):

$$FZ = \left[(\Phi, \varphi_2) \mid cos^{-1}\left(\frac{\cos\varphi_2}{\sqrt{1+cos^2\varphi_2}}\right) \leq \Phi \leq \frac{\pi}{2}, \ 0 \leq \varphi_2 \leq \frac{\pi}{4}\right]. \tag{4.13}$$

The symmetrized spherical surface harmonics basis functions exhibiting cubic-transversely isotropic symmetry denoted as $K_l^m(g)$ are used for this case study. In this description of symmetry, the first term reflects the crystal symmetry and the second term reflects the sample symmetry (arises because the indentation direction is unaffected by any in-plane rotation of the sample). As described in the previous section, the Fourier coefficients of Eq. (4.6) can be determined using OLS regression (Eq. (4.7)).

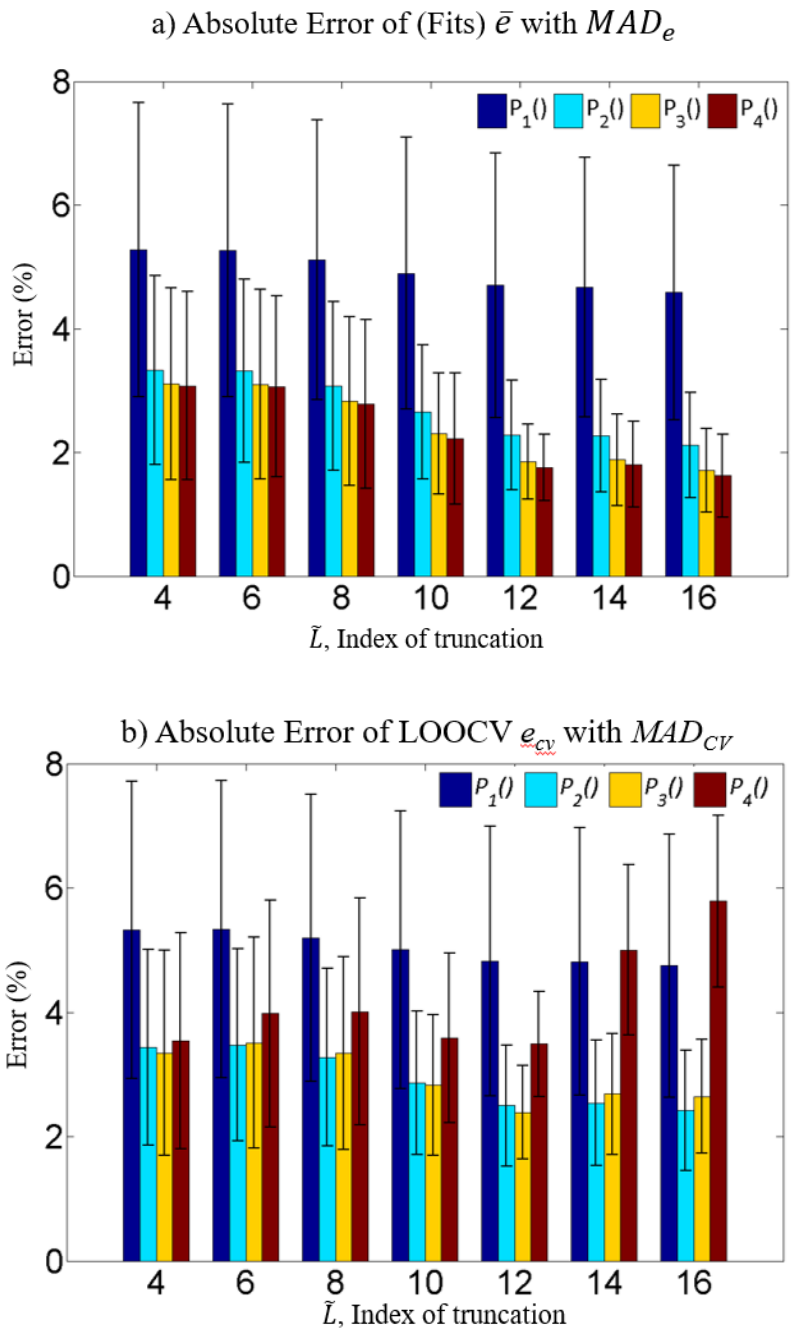

Figure 4.4 a) The mean absolute error for varying numbers of SSH basis functions ($\tilde{L}$) and degree of Legendre polynomial ($\tilde{q}$) with MAD of absolute error as the error bars. b) The mean absolute error of LOOCV for varying numbers of SSH basis functions ($\tilde{L}$) and degree of Legendre polynomial ($\tilde{q}$) with MAD of absolute error of LOOCV as the error bars.

The values of $\bar{e}$ (Eq. (4.8)) and MAD_e (Eq. (4.9)) were computed for the training set for different selections of $\tilde{q}$ and $\tilde{L}$, and are summarized in Fig. 4.4. The mean and median measures of the error decreases with increasing values of $\tilde{q}$ and $\tilde{L}$ as expected (see Fig. 4.4a). The LOOCV analyses (Fig. 4.4b) indicates over-fitting of the data points at high values of both $\tilde{q}$ and $\tilde{L}$. For instance, the $\bar{e}_{CV}$ values for the fits obtained using $\tilde{L} > 12$ and $\tilde{q} > 3$ start to increase significantly. Examination of the error measures shown in Figs. 4a and 4b suggests that $\tilde{L} = 12$ and $\tilde{q} = 3$ provide a good fit for the dataset acquired in this study using FE simulations. This level of truncation produces a total of 348 Fourier coefficients; these are utilized in this study to describe the functional dependence of indentation modulus on orientations and the independent elastic constants. The accuracy of the truncated spectral representation of the indentation moduli over the selected range of cubic elastic constants for several orientations was compared against the values predicted by the previously validated FE model and the analytical solution provided by Vlassak and Nix (Vlassak et al., 2003). Representative results are shown in Fig. 4.5 for a selected range of elastic anisotropic ratios for two orientations that provide the extremal responses. The indentation modulus in this plot was normalized by the indentation modulus of a polycrystalline aggregate, following the approach outlined by Vlassak and Nix (Vlassak and Nix, 1993) and using the expressions provided by Hashin and Shtrikman (Hashin and Shtrikman, 1962). The error between the FE prediction and the spectral representation for any given set of cubic elastic constants (within the selected bounds mentioned earlier) and any orientation was found to be within 4%. It is clear that the spectral representation developed in this work captures well the variations in the

indentation moduli for different orientations and different degrees of elastic anisotropy in the sample.

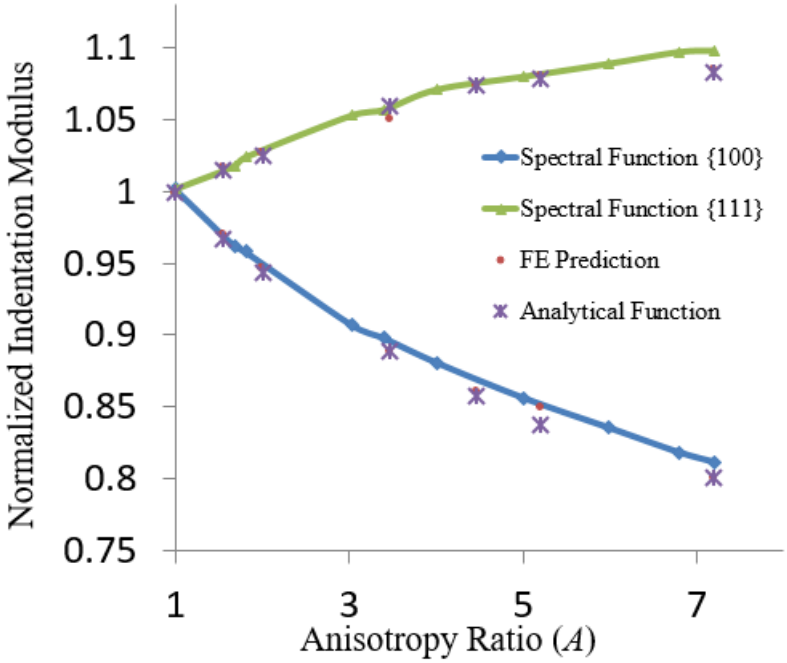

Figure 4.5 Comparison of the spectral representation of normalized indentation modulus as a function of anisotropic ratio against the predictions of the FE model and the analytical model of Vlassak and Nix.

We now turn our attention to estimating the single crystal elastic stiffness parameters of Fe-3%Si, for which indentation measurements on differently oriented single crystals were already reported in prior work (Pathak et al., 2009) . These results are summarized in Table 4.2, where the orientations are also plotted on the standard inverse pole figure. The effective indentation moduli reported in this table for Fe-3%Si were computed using Eqs. (4.1-4.3), where the Young's modulus and Poisson ratio of the indenter were taken as 1000 GPa and 0.07, respectively (Field and Swain, 1993) . Estimating the single crystal constants of Fe-3%Si then reduces to minimizing the difference between the values predicted by the Fourier function established earlier and

the discrete measured indentation moduli reported in Table 4.2. This minimization was accomplished using a Newton-Raphson scheme described in the previous section (see Eqs. (4.10-4.12)). The estimated values of the single crystal elastic constants for the as-cast Fe-3%Si polycrystalline sample from this study are $C_{11} = 215.7$ GPa, $C_{12} = 131.6$ GPa, and $C_{44} = 122.2$ GPa. The single crystal elastic constants obtained using the inverse solution approach described in this paper are within 5% of the typical values reported in literature for Fe-3%Si ($C_{11} = 225.28$ GPa, $C_{12} = 135.1$ GPa, $C_{44} = 102.2$ GPa) (Alberts and Wedepohl, 1971; Machova and Kadečková, 1977; Routbort et al., 1971).

a)

Fe-3%Si As-cast			
	Grain No.	**Orientation (φ_1, Φ, φ_2)**	**Experimental E_{eff}, GPa**
Near (111)	**2**	339.8, 54.4, 46.1	202.9
	7	103.7, 121.6, 49.9	199.3
	10	232.5, 53.1, 324.0	197.7
	6	83.2, 125.4, 30.4	195.9
Near (101)	**3**	3.0, 41.3, 76.4	194.0
	5	194.7, 79.7, 317	191.1
	9	50.0, 38.1, 250.1	190.5
Near (001)	**1**	114.2, 85, 173.5	173.2
	8	170.0, 102.6, 357.9	178.3
	4	163.6, 78.8, 168	181.2
	11	259.9, 238.0, 145.8	189.6

b)

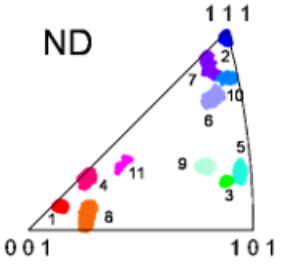

Table 4.2. a) Measured values of the effective indentation modulus, E_{eff}, for eleven different orientations, and b) representation of the orientations in an inverse pole figure map.

The accuracy of the spectral framework mentioned above can be improved with additional measurements of indentation moduli on additional crystal orientations. Note that we used only eleven measured indentation moduli in the present case study. One might actually argue that we need only three measurements (on three distinct crystal orientations) to estimate the three unknown elastic stiffness constants in cubic crystals. However, because of the regression methods used in the approach described here, it is important to measure indentation moduli for orientations that are well spread out in the fundamental zone of orientations. For example, if we were to repeat the inverse solution presented here by considering only three orientations clustered in any one of the corners of the inverse pole figure (depicts a certain projection of the fundamental zone of orientations) shown in Table 4.2, it would produce highly erroneous estimates of the single crystal elastic stiffness constants. In fact, it is best to ensure that there at least some measurements in each of the three corners of the inverse pole figure shown in Table 4.2, as these orientations typically produce the maximum contrast in the indentation moduli.

It is also likely that there are better representations of the indentation modulus as a function of the orientation and the elastic stiffness constants. Although we have had a lot of experience with the use of SSH as a Fourier basis for the orientation variable, we only have very limited prior experience in spectral representation of the elastic stiffness parameters. Therefore, it is entirely possible that one might accomplish a more accurate representation of the indentation modulus function (Eq. (4.5)) with a different Fourier basis, which might in turn improve the accuracy of the estimates of the elastic stiffness constants.

CHAPTER 5

EXTRACTING SINGLE CRYSTAL EFFECTIVE SLIP RESISTANCE PARAMETER FOR CUBIC POLYCRYSTALLINE METALS

Successful deployment of polycrystalline metals in demanding engineering applications requires a detailed understanding of their microscale deformation behavior. The deformation behavior of these materials is characterized and controlled by dislocation slip at the level of individual grains (i.e., crystals) in the polycrystalline sample. Accurate characterization of the slip resistance and other slip parameters (Asgari et al., 1997; Beyerlein and Tomé, 2007; Gambin and Barlat, 1997; Kalidindi et al., 2004; Knezevic et al., 2009; Pathak et al., 2009; Sarma and Dawson, 1996; Vachhani et al., 2016) is essential to determining the macroscopic constitutive response of a polycrystalline aggregate subjected to finite plastic deformation. In this chapter, a two-step protocols formulated in the previous chapter is utilize to estimate the average slip resistance for cubic polycrystalline metal.

5.1 Introduction

Considerable attention has been paid to measure or estimate the slip resistance values and the slip hardening parameters from polycrystalline samples. A common practice in literature has been to extract these values by calibrating the polycrystalline deformation experiments with their corresponding simulations. For instance, the slip resistance values are estimated by calibrating the predicted macroscopic yield for different textures to the measured yield in multiple loading conditions (Barlat et al., 1997; Bron and Besson, 2004; Kalidindi and Anand, 1992; Kalidindi et al., 1992). Such approaches necessarily employ a homogenization scheme to relate the single crystal slip parameters to the effective polycrystalline response. Examples of such homogenization schemes range from the simple Taylor-type models (Taylor, 1934, 1938) to self-consistent models (Lebensohn and Tomé, 1993; Segurado et al., 2012; Tomé et al., 2002; Tomé et al., 2001) to micromechanical crystal plasticity finite element models (CPFEM) (Bachu and Kalidindi, 1998; Becker, 1991; Delannay et al., 2009; Kalidindi and Anand, 1992; Kalidindi et al., 1992; Tikhovskiy et al., 2007). Consequently, the slip parameters extracted using these approaches are meant to be used exclusively with the specific homogenization schemes employed in estimating them in the first place. In other words, the calibrated slip parameters extracted in these approaches reflect an inherent bias introduced by the use of the homogenization model. Furthermore, since each test (combination of each texture and loading condition imposed on the sample) constitutes one data point, one typically needs to expend a substantial amount of time and effort to generate a sufficiently large dataset that provides robust values of the slip parameters of interest.

Alternately, it is possible to grow and test single crystals of many metals to estimate the values of the slip resistance. Such single-crystal experiments are effort and time intensive, as they require carefully controlled growth of preferentially oriented grains, their characterization via electron backscatter diffraction (EBSD) method, and the preparation of oriented test samples excised from these crystals. In practice, it is often impractical to produce sufficiently large volumes of the microscale constituents of interest in their pure form to allow the application of standardized mechanical testing methods (such as compression and tensile testing). Another approach explored in literature involves the compressive testing of micro-pillars fabricated using focused ion-beam (FIB) in a scanning electron microscope (SEM) (Li et al., 2011; Shan et al., 2008; Uchic et al., 2004) . All of the techniques described above generally demand effort intensive sample preparation protocols and highly specialized test equipment.

Among the different experimental techniques explored thus far in literature, instrumented indentation (Doerner and Nix, 1986; Oliver and Pharr, 1992) exhibits tremendous potential as a low cost, high throughput, approach because of its capability to probe quickly multiple local volumes in a small sample. Indeed, indentation techniques have been employed successfully to characterize the local mechanical responses in individual grains in a polycrystalline sample (i.e., at length scales significantly lower than typical grain sizes). Although one can measure directly the local response at selected locations in a sample, one still needs a sophisticated strategy to extract the values of the slip parameters of interest from the measured load-displacement curves. The general approach for addressing this challenge has been to employ optimization strategies that minimize a suitably defined error between the measurements (typically the load-

displacement curves) and the corresponding predictions from a finite element (FE) simulation of the indentation experiment, by fine-tuning the model parameters of interest (such as slip resistances). Examples of such efforts have included the extraction of the average slip resistance value for single crystal copper (Liu et al., 2008; Zaafarani et al., 2006) and the hardening rate for low-alloy steels (Dao et al., 2001; Kucharski and Mróz, 2001). Since the entire elastic-plastic transition occurs over a very short regime in the indentation load-displacement curve (Kalidindi and Pathak, 2008; Pathak and Kalidindi, 2015) , it is generally very difficult to identify this regime precisely on the measured load-displacement curve. Consequently, values of the slip parameters estimated using such approaches are generally not robust (i.e., very sensitive to small changes in the protocols employed). Indeed, it is much more practical and insightful to compare the indentation stress-strain curves instead of the load-displacement curves in calibrating the material constitutive laws (Donohue et al., 2012). In this regard, the recently developed spherical nanoindentation data analysis protocols have shown tremendous potential (Kalidindi and Pathak, 2008; Pathak and Kalidindi, 2015). These new data analysis protocols convert the load-displacement data obtained during spherical nanoindentation into a meaningful indentation stress-strain (ISS) curve (details discussed in chapter 2), which exhibits a clear initial elastic regime followed by an elastic-plastic transition (Kalidindi and Pathak, 2008; Pathak et al., 2008; Pathak et al., 2009).

5.2 CPFEM of spherical nanoindentation

The central goal of this investigation is to extend the recently developed protocols for estimating elastic parameters to estimate the effective slip resistance, *s*, in cubic

polycrystalline samples. Assuming that this value is uniform on all the slips systems in the indentation zone, the desired function (analogous to Eq. (4.5)) can be expressed as

$$\tilde{Y}_{ind}(g) = \frac{Y_{ind}(g)}{s} = \sum_{l=0}^{\infty} \sum_{m=1}^{M(l)} B_l^m K_l^m(g) \tag{5.1}$$

where Y_{ind} is the indentation yield strength, and $\tilde{Y}_{ind}(g)$ is a normalized indentation yield strength. Note that these two definitions of the indentation yield strength are linearly related through the slip resistance. Therefore, in many ways, it should actually be much easier to establish the function described in Eq. (5.1) compared to what was done earlier for Eq. (4.5) in the previous chapter. However, the central challenges are: (i) the CPFEM simulations needed to establish the SSH coefficients, B_l^m, are computationally much more demanding, and (ii) the number of coefficients needed are expected to be significantly higher (plastic properties are known to require many more terms compared to elastic properties in the Fourier representations; cf. (Adams et al., 2012; Fullwood et al., 2010).

The first step in our protocol requires the generation of a dataset that can be used to estimate the Fourier coefficients in Eq. (5.1). It is important to build a computationally efficient crystal plasticity-based FE model of the spherical indentation for this purpose. Since we intend to use this model to simulate indentations over a broad range of crystal orientations, the computational efficiency of the model is of utmost importance. In this work, we have employed a previously established and validated model (Kalidindi and Anand, 1992) as a UMAT (user material subroutine) in ABAQUS (ABAQUS, 2014) to simulate the spherical indentation test. A complete description of this model along with the implementation details have already been published in prior literature (Bachu and

Kalidindi, 1998; Bhattacharya and Nix, 1988; Kalidindi and Anand, 1992; Kalidindi and Schoenfeld, 2000). A brief description of the FE model of indentation is being described in this section.

Because the sample in the indentation simulations is likely to be assigned an arbitrary lattice orientation, we cannot take advantage of any symmetry in the indenter geometry (the sample response is fully anisotropic). Consequently, it is necessary to develop a complete three-dimensional FE model of the indenter-sample system for the present study. In general, a fine mesh density is needed to capture reliably the evolving elastic-plastic response under the indenter. However, it is important to note that increasing the number of finite elements in the mesh increases the computational cost per simulation significantly. A large number of different meshing schemes were explored in this study before settling on the final model.

The FE model developed and employed for this study is shown in Fig. 5.1 and comprises of two three-dimensional solids: (i) an elastic-plastic deformable sample with an initially flat surface, and (ii) a rigid hemi-spherical indenter of radius 13.5μm (typical size of the indenter in prior experimental studies (Kalidindi and Pathak, 2008; Pathak and Kalidindi, 2015; Pathak et al., 2008; Pathak et al., 2009). Eight-noded, three-dimensional, continuum elements (C3D8 in ABAQUS) were used to mesh the deformable part. The size of the sample was selected as $10\mu mX10\mu mX10\mu m$ to ensure that the stress-strain fields are well within the primary indentation zone size. There were a total of $17K$ elements within the indentation zone, whose overall length scale was observed to be about ~2.5μm from our simulations. The indentation zone has been discretized into seven regions as shown in Fig. 5.1a to permit the use of progressively higher mesh density as

we approach the indentation zone directly below the indenter-sample contact surface. This partitioning allows highest mesh densities in the regions where steepest gradient in the stress (or strain) fields are expected in the sample. With this meshing scheme, the innermost region ($0.1\mu mX0.1\mu mX0.07\mu m$) has an element size of ($3.9nmX3.9nmX4.4nm$). The aspect ratio of the element in the indentation zone was 1.8. The aspect ratio of the elements outside the indentation zone is larger, but these regions experience fairly minimal stresses and strains. A hard surface-to-surface, frictionless, contact was defined between the sample and indenter. A vertical displacement boundary condition was imposed on the indenter. The bottom surface of the sample was constrained along the z-direction (indentation direction). Encastre boundary condition is defined at the center of the bottom surface of the sample to arrest rigid body translations and rotations. The lateral surfaces of the sample material are kept free throughout the simulation. The displacement of the indenter and the total force applied on the sample are recorded at every time increment from the simulation.

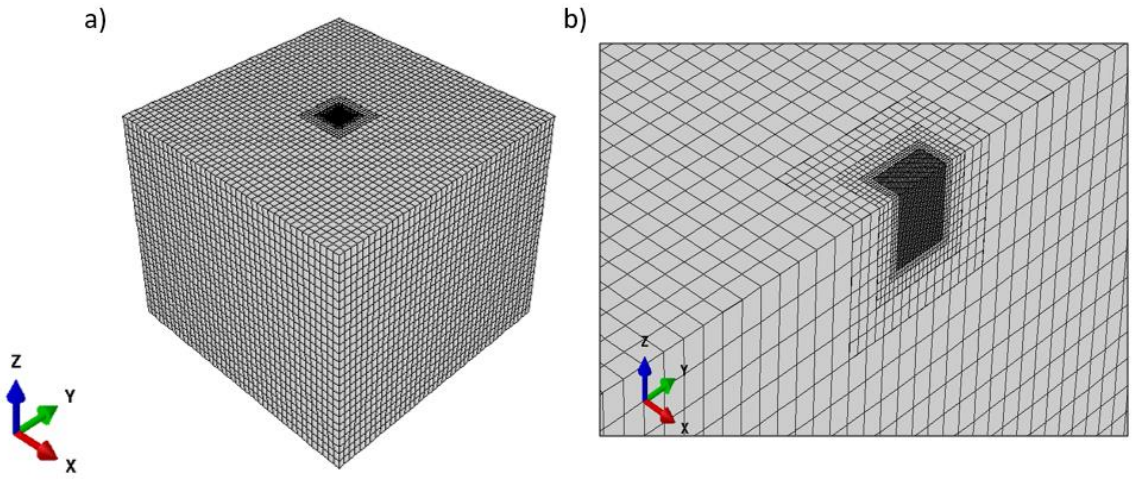

Figure 5.1. a) Finite element mesh of the sample in the spherical nanoindentation. b) Close-up view of a midsection through the indentation zone under the indenter tip.

The finite element model developed in this study was validated by comparing the indentation stress-strain curve for isotropic perfectly-plastic material constitutive behavior with the previously published result obtained using a 2-D FE model (see Fig 5.2). The FE mesh developed and utilized in this work enabled a relatively fast computation of the ISS curves using the crystal plasticity constitutive model. The final mesh employed in this work executed in about 5 hours per simulation on 20 CPUs provided by Partnership for Advanced Computing Environment (PACE) facility.

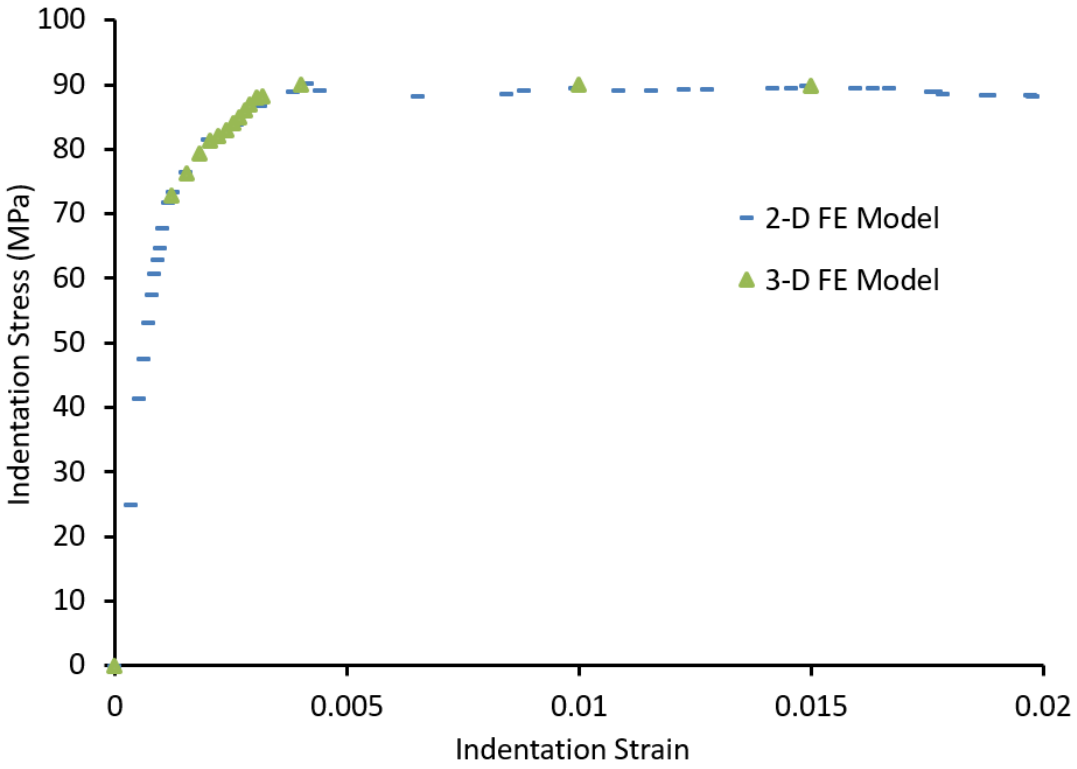

Figure 5.2. Comparison of the predicted ISS response from FE simulation against the corresponding prediction of ISS curve using 2-D FE simulations of indentation for isotropic perfectly plastic response

5.3 Orientation dependence of indentation yield in BCC crystals

As discussed earlier, our first goal in this work is to establish the Fourier coefficients, B_l^m, in Eq. (5.1). Our strategy will be to numerically evaluate $\tilde{Y}_{ind}(g)$ for a sufficiently large number of crystal orientations using the crystal plasticity FE model described in the previous section, and to use this data to estimate (or calibrate) the Fourier coefficients, B_l^m, using a linear regression method. The inputs to the crystal plasticity FE simulations of spherical indentation are the single crystal elastic stiffness constants, the crystal lattice orientation (g), and arbitrarily chosen average initial slip resistance parameter, $s_0 =$ 8 MPa for all 48 slip systems (Kocks et al., 2000). It is important to note that the sample is assumed to initially be a single crystal region (i.e., all elements are assigned the same initial crystal lattice orientation) and is assumed to be non-hardening (as this has no relevance to our goal of establishing the function defined in Eq. (5.1)). The crystal orientation is described by a set of three Bunge-Euler angles (H, 1982) denoted as $(\varphi_1, \Phi, \varphi_2)$. Since, any arbitrary rotation of the sample about the axis of the spherical indenter does not influence the indentation response, the extracted ISS curves and the value of Y_{ind} only depend on two of the three Bunge-Euler angles, (Φ, φ_2). Considering the inherent crystal cubic symmetry and the transversely-isotropic sample symmetry, the crystal lattice orientations for different simulations were selected from the fundamental zone (FZ) defined by

$$FZ = \left[(\Phi, \varphi_2) \mid cos^{-1}\left(\frac{\cos\varphi_2}{\sqrt{1+cos^2\varphi_2}}\right) \leq \Phi \leq \frac{\pi}{2}\,, \qquad 0 \leq \varphi_2 \leq \frac{\pi}{4}\right].$$

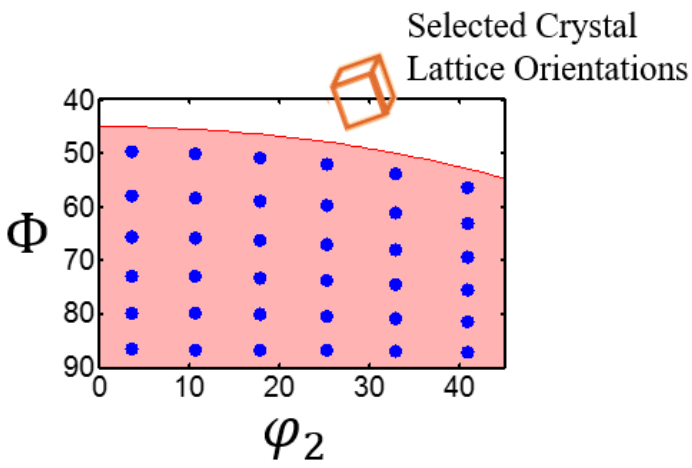

Figure 5.3. Distinct set of selected crystal lattice orientations spanning the cubic-transversely isotropic fundamental zone (highlighted area).

For the present study, 36 crystal lattice orientations were selected from the FZ by discretizing the orientation space in a way that ensures that the bins size has the same invariant measures (see Fig. 5.3; cf. (Fullwood et al., 2010)). The indentation yield strength is extracted from the ISS curve using a 0.2% offset indentation plastic strain as shown in Fig 5.4.

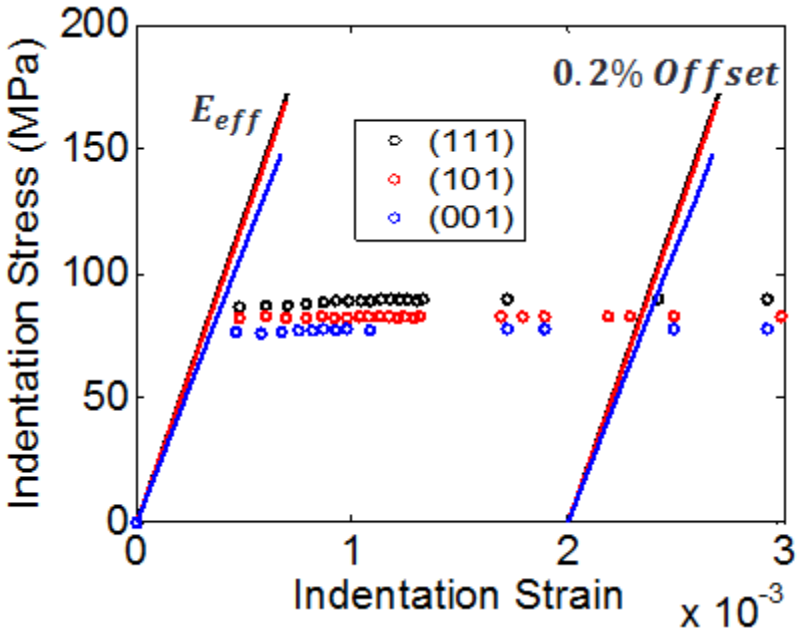

Grain	Effective Modulus (GPa)	Indentation Yield (MPa)
(111)	202.5	~89.5
(101)	196	~82.5
(001)	170.2	~77.5

Figure 5.4. Indentation stress-strain curves predicted using CPFEM of nanoindentation for three different grains.

An ordinary least square approach described in our previous work (Patel et al., 2014) has been used to calibrate the Fourier coefficients, B_l^m (see Eq. (5.1)). Through repeated trials, it was found that truncating the Fourier representation at l = 6 provided a good representation. This truncation level results in a total of 23 Fourier coefficients. The truncation error was observed to be less than 5%. This is consistent with prior work on the microstructure-sensitive design (MSD) framework, where plastic properties such as

tensile and shear yield strength showed similar error levels when truncated at l = 6 (Proust G, 2004).

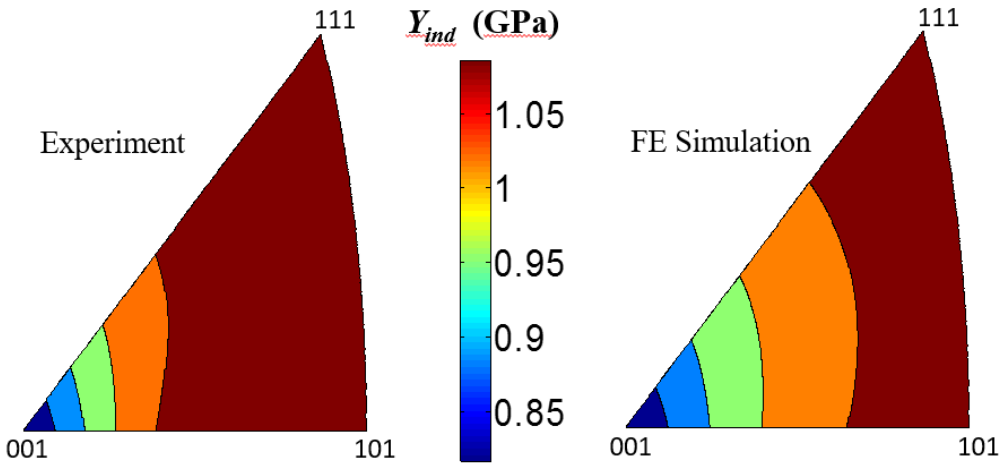

Figure 5.5. Inverse pole figure (IPF) map showing the surface contours of the variation in the indentation yield strength over the orientation space based on experimental observations and FE simulations.

As another validation, we present in Figure 5.4 a comparison between $\tilde{Y}_{ind}(g)$ established in this work and the $Y_{ind}(g)$ measured experimentally in prior work on an as cast Fe-3%Si BCC polycrystalline sample (Pathak et al., 2009). Note that it is not possible to compare directly the predicted and measured indentation yield strengths, since the value of the slip resistance for the sample used in the experiment is unknown. However, this is precisely the main point of this paper. The excellent agreement in the shapes of the contours shown in Figure 5.5 suggests that we should be able to extract the value of the slip resistance simply by calibrating the experimental results to the FE predicted results. This is pursued next.

5.4 Estimating the initial slip resistance

The main goal of this work is to develop and validate a robust methodology to extract the value of the local (i.e., length scales well below the typical grain size) slip resistance from a polycrystalline bcc sample. This will be accomplished by minimizing the difference between CPFEM predicted indentation yield values and the corresponding measured values on a selected set of grain orientations in the given polycrystalline sample. A suitable definition of the error for such a regression analyses can be expressed as

$$\chi^2(s) = \sum_{j=1}^{N} \left[\frac{Y_{ind}^{Exp}(g_j) - \left(s\tilde{Y}_{ind}(g_j)\right)}{\sigma_j} \right]^2 \tag{5.2}$$

where j enumerates the grain orientations where the measurements were made, N is total number of grain orientations studied in the given sample, and σ_j denotes the standard deviation for multiple measurements on a single grain (this allows us to account for potentially different levels of variance in the measurements in the differently oriented grains). The value of the slip resistance, s, can then be determined easily by minimizing the χ^2 function (i.e., setting its derivative with s to zero). This value can be computed as

$$s = \frac{\sum_{j=1}^{N} \frac{\tilde{Y}_{ind}(g_j) Y_{ind}^{Exp}(g_j)}{{\sigma_j}^2}}{\sum_{j=1}^{N} \frac{\tilde{Y}_{ind}(g_j) \tilde{Y}_{ind}(g_j))}{{\sigma_j}^2}}. \tag{5.3}$$

It is possible to compute the variance on the estimated value of the slip resistance (as a measure of the uncertainty involved in the estimated value) as (Press, 2007)

$$\sigma_s^2 = \sum_{j=1}^{N} {\sigma_j}^2 \frac{\partial s}{\partial Y_{ind}^{Exp}(g)\big|_{g=g_j}} = \frac{\sum_{j=1}^{N} \tilde{Y}_{ind}(g_j)}{\sum_{k=1}^{N} \frac{\tilde{Y}_{ind}(g_k)\tilde{Y}_{ind}(g_k))}{{\sigma_k}^2}} \tag{5.4}$$

5.5 Case study: As-cast Fe3%Si Polycrystalline Sample

The protocols described in the earlier sections will now be demonstrated on measurements reported previously on an as-cast Fe-3%Si polycrystalline steel sample. These previously reported measurements are summarized in Table 5.1 (Pathak et al., 2009). The regression techniques described in the previous section produced an estimated value (along with estimated variance) of the slip resistance as 155.4 ± 3.5 MPa for the as-cast Fe-3%Si polycrystalline material. This estimated value lies within the range of values reported in prior literature for Fe-3% Si using a variety of protocols. For example, a value of 146.12 MPa (Hull, 1963) was obtained from single crystals deformed in tension. A value of 161 MPa (Klusemann et al., 2012; Orlans-Joliet et al., 1990) was obtained from calibrating the tensile test data on single crystals of Fe-3% Si for different lattice orientations via crystal plasticity finite element analysis. Additionally, the effective slip resistance value was also estimated from measurements on polycrystalline samples of Fe-3%Si. These values fall within the range of values obtained from the single crystals studies. For instance, from tensile studies on fine (20μm) and coarse (170μm) grain sized Fe-3%Si (Suits and Chalmers, 1961), it was deduced that the yielding is independent of the grain size and the value of slip resistance was estimated to be in the range of 130.42 MPa and 157.9 MPa. Clearly, the values obtained in this study are in good agreement with those obtained in prior studies described above.

a)

As-cast Fe-3%Si			
	Grain No.	**Orientation (φ_1, Φ, φ_2)**	**Experimental Y_{ind} (GPa)**
Near (111)	**2**	339.8, 54.4, 46.1	1.13 ± 0.04
	7	103.7, 121.6, 49.9	1.12 ± 0.02
	10	232.5, 53.1, 324.0	1.12 ± 0.16
	6	83.2, 125.4, 30.4	1.10 ± 0.02
Near (101)	**3**	3.0, 41.3, 76.4	1.09 ± 0.04
	5	194.7, 79.7, 317	1.07 ± 0.01
	9	50.0, 38.1, 250.1	1.06 ± 0.02
Near (001)	**1**	114.2, 85, 173.5	0.85 ± 0.04
	8	170.0, 102.6, 357.9	0.91 ± 0.06
	4	163.6, 78.8, 168	0.93 ± 0.04
	11	259.9, 238.0, 145.8	1.0 ± 0.06

b)

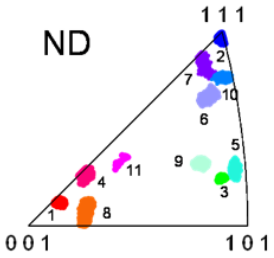

Table 5.1. a) Measured values of the indentation yield, Y_{ind}, for eleven different orientations, and b) representation of the orientations in an inverse pole figure map (Pathak et al., 2009).

5.4 Robustness of the approach

The robustness of the estimated value of the slip resistance from the protocols described in this paper (i.e., sensitivity of the estimated value to the choices made in the estimation protocols) depends critically on the number and quality of the indentation yield measurements available, and the orientation space they cover. Note that indentation yield measurements were available from only 11 distinct grain orientations for this study. In general, a critical selection of the grain orientations for the indentation measurements is essential for a reliable estimation of the slip resistance value. Because of the regression

method used in the approach described here for the estimation of the effective slip resistance, it is important to select orientations that produce robust estimates of the slip resistance.

In order to systematically evaluate the robustness of the estimated value of the slip resistance, one can subsample the measurements and repeat the entire estimation protocol. Let N (in the present case study, N =11) denote the total number of grain orientations studied using indentation protocols described in this paper. If one were to decide to make indentation measurements on only k grain orientations ($k \leq N$), it would be possible to identify $\left\langle {N \atop k} \right\rangle = \frac{N!}{k!(N-k)!}$ distinct ensembles (i.e., subsamples) of potential datasets that might have been collected. As an example, if k = 1, the number of distinct ensembles is 11 for the present case study. For k = 2, the number of distinct ensembles is 55. A study of the estimated values of the slip resistance from each such ensemble will provide insights into how many grain orientations are needed to obtain reliable results. It will also provide some insights on how to select the grain orientations for the indentation measurements.

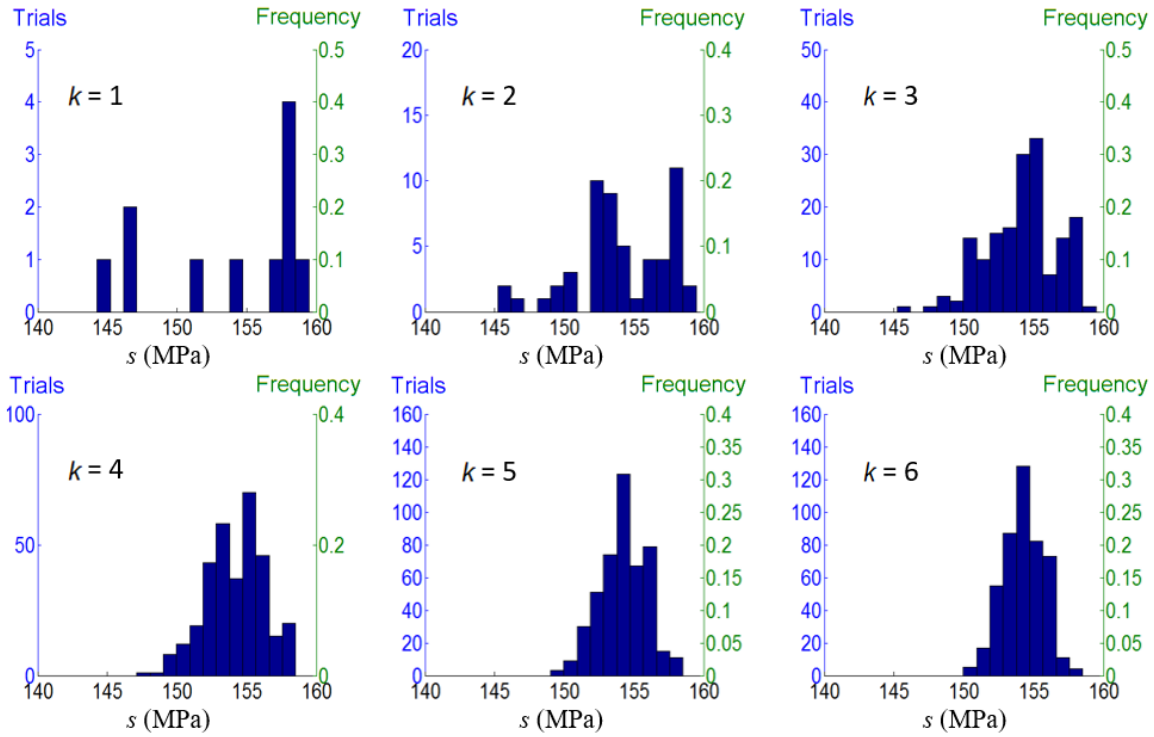

Figure 5.6. The frequency distribution of the estimated slip resistance values using various ensembles of subsamples.

The estimated values of the slip resistance for the different choices of k from the ensembles created as described above are summarized in Figure 5.6 as frequency plots. As expected, the distribution of the estimated value of the slip resistance sharpens significantly with an increase in k. Interestingly, as stated earlier, the distribution of the estimated values is mostly within 155.4 MPa $\pm$ 3.5 MPa for the higher values of k (see k = 6 in Figure 5.6). One might look at the percentage of estimated values within 3% of the mean estimated value for each value of k to determine how many grain orientations are needed to establish a reliable value of the slip resistance using the protocols described in this paper. This value increases from 72% for k = 1, to 87% for k = 2, to 93% for k = 3, to 96% for k = 4. This simple analysis suggests that there is a high likelihood of obtaining a reliable value of the slip resistance with indentation measurements in as few as four

different grain orientations. Figure 5.7 shows the specific ensembles (i.e., selections of four grain orientations) that produced the closest estimates to the value of 155.4 MPa estimated in this study. From a review of these inverse pole figures, the following guidelines emerge for the selection of the grain orientations for the indentation measurements: (i) select grains with orientations close to each of the corners of the inverse pole figures, and (ii) distribute the orientations as uniformly as possible to cover the fundamental zone of the orientation space.

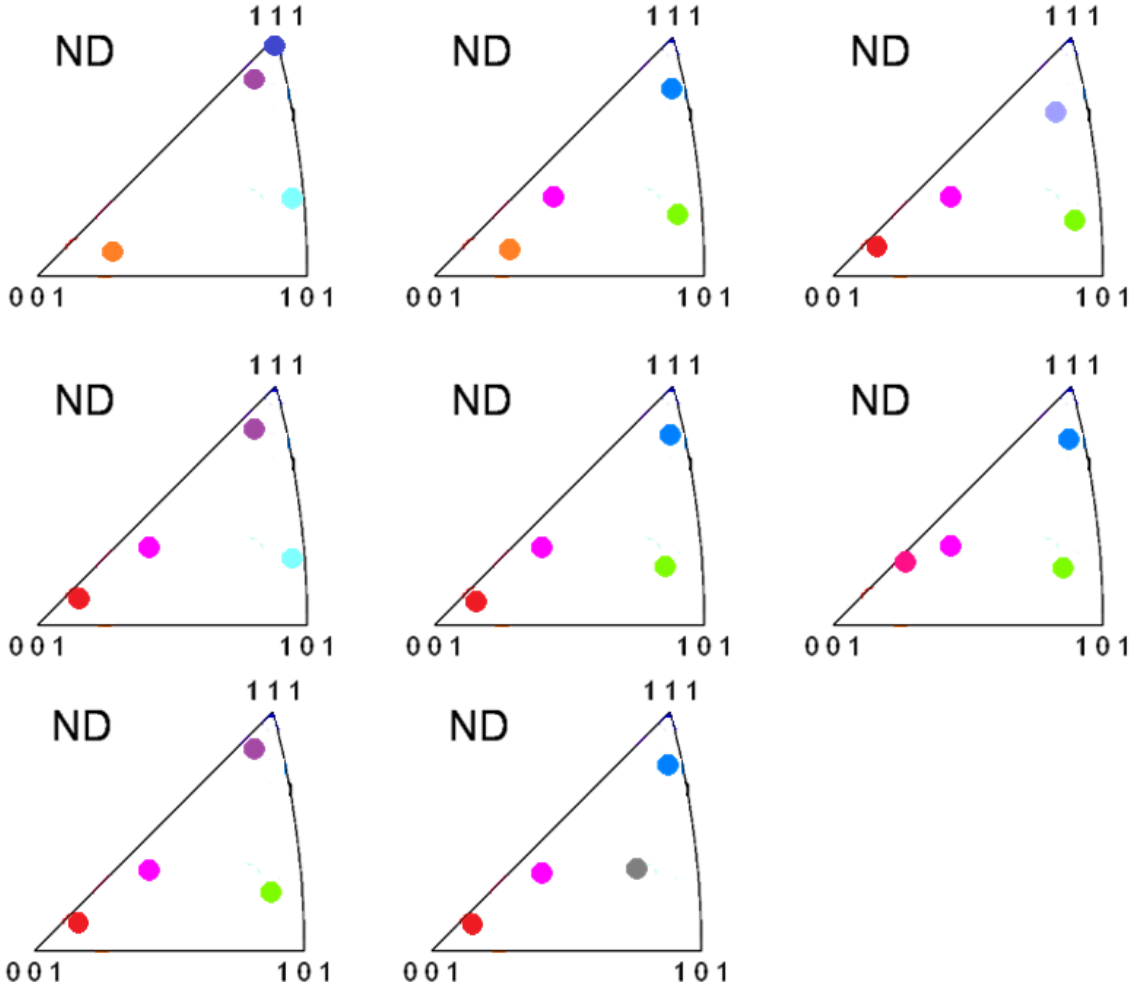

Figure 5.7. Ensembles from k = 4 (four grain orientations selected randomly) that produced values closest to the estimated slip resistance of 155.4 MPa from the entire collection of eleven grain orientations.

CHAPTER 6

CONCLUSION

Successful development and deployment of polycrystalline metals in demanding engineering applications requires a detailed understanding of their microscale and macroscale deformation behavior by using physic-based constitutive theories coupled with finite element simulations tools. Such models require relevant physical material parameter at those length scales. In this thesis, robust protocols are developed to characterized macroscale and microscale elastic-plastic parameters at significantly lower effort and cost by combining the mechanical information obtained from indentation measurements and FE simulations.

At macroscale, this work addressed the longstanding problem of recovering uniaxial mechanical response from instrumented indentation experiments, with the central challenge being the lack of validated protocols for converting indentation stress and strain values to equivalent values in uniaxial stress states such as simple compression. This study has developed new protocols to address this critical gap for materials exhibiting isotropic plasticity. The protocols presented in this study were validated using FE models of indentation with a broad range of isotropic elastic-plastic constitutive response following J_2-flow theory. In the study, the following key advances are made.

a.) A novel framework and protocols are formulated to correlate indentation stress-strain curves and the simple compression stress-strain curves. This protocol involves different scaling factors for indentation stress, elastic indentation strain,

and plastic indentation strain. This paper represents the first report of such a comprehensive protocol that specifically addresses all of the components of a stress-strain curve. Furthermore, the protocol developed here involves very simple scaling relationships to scale indentation stress-strain curve to uniaxial stress-strain curves and vice-versa.

b.) An elastic-plastic finite element model of indentation was developed and validated. The new protocols for mapping indentation stress-strain measurements into compression stress-strain curves are validated for a variety of materials exhibiting a broad range of hardening behaviors using the finite element model as a surrogate for the experiment.

c.) A specific protocol was developed to reliably identify offset indentation yield strength from experimental measurements and to correlate it to 0.2% offset uniaxial yield strength used extensively in current literature. The right offset indentation strain level was identified as 0.15% and the corresponding scaling factor (also called constraint factor) was identified as 2.0. The identification of this protocol now fills a critical gap in our ability to extract meaningful material properties from instrumented indentation experiments.

At microscale development of robust, physics-based multi-scale materials model is significantly hampered by the lack of validated tools and protocols for characterizing reliably the local anisotropic properties at sub-micron length scale. Here, I developed inverse methodology to extract grain scale elastic-plastic properties using spherical indentation measurements and finite element models. In particular, a two-step protocols are developed to extract the elastic stiffness constants for cubic polycrystalline metal

sample from a collection of spherical nanoindentation and lattice orientation measurements.

a.) In the first step, a suitable FE model of nanoindentation is developed as a surrogate to the experiments to capture the functional dependence of the property of interest on the crystal lattice orientation at the indentation site and the relevant physical material parameters. This functional dependence is captured in a compact spectral representation using surface spherical harmonics functions.

b.) In the second step, measured values of the property of interest and the crystal lattice orientation at the indentation site from a polycrystalline sample are fitted to the spectral function established in the first step to provide a robust estimate of the elastic-plastic material parameters.

c.) The validity of this approach is demonstrated for annealed Fe-3%Si polycrystalline sample using measurements published in prior literature.

Similarly, a robust protocol has been formulated to extract the effective slip resistance value for cubic material system from spherical nanoindentation and orientation measurements. This protocol was developed through the following steps:

a.) A crystal plasticity finite element model of nanoindentation is developed in ABAQUS to capture the variation in the mechanical behavior of the differently (lattice) oriented grains in a simple analytical expression using spectral representations.

b.) The protocol was demonstrated on as-cast polycrystalline Fe-3%Si sample. The effective slip resistance value was estimated by matching the experimental measurements with the analytical expression established in (a). The estimated

value lies in the range of the reported literature values for Fe-3%Si using other protocols.

c.) The protocols provide guidelines for the selection of the grain orientations for the indentation measurements: (i) select grains with orientations close to each of the corners of the inverse pole figures, and (ii) distribute the orientations as uniformly as possible to cover the fundamental zone of the orientation space.

6.1 Future work

The lack of validated methods to characterize the changes in the local anisotropic elastic-plastic properties of the microscale constituents is a major impediment to attaining a deeper physics-based understanding on the material microstructure and its mechanical properties. This work is a crucial step in establishing methodologies and protocols for extracting reliable local mechanical properties from nanoindentation. The developed protocols here provide high-throughput reliable characterization technique which enables further physics-based understanding of materials behavior. While current research focuses only on cubic metallic materials, the techniques developed here can be easily extended to complex material systems such as hexagonal metals. The long term impact of this work is likely to result in fast characterization of complex material systems which is likely to result in accurate multi-scale physics-based model to predict materials behavior across multiple length scales.

APPENDIX A

SPECTRAL REPRESENTATION

The protocols to extract microscale properties developed in this work is built on prior Microstructure Sensitive Design (MSD) framework which allows a rigorous treatment of properties represented over an orientation space. This is accomplished through the proper utilization of the Fourier basis functions. There are several advantages in utilizing these basis functions: i) Fourier basis form a *complete* set of basis functions and are orthogonal; ii) properties can be expressed with a finite number of terms over orientation space; iii) invertible relationship exists between properties and microstructures.

Generalize surface spherical harmonic (SSH) functions, a subset of Fourier basis are employed to approximate the orientation dependence functions and the associated properties. SSH functions have already been demonstrated to produce highly efficient and compact spectral representation of desired functions over the orientation space, g (H, 1982) defined as

$$T_l^m(g) = T_l^m(\varphi_2, \Phi) = \sum_{l=0}^{\infty} \sum_{m=-l}^{+l} e^{im\varphi_2} P_l^m(\cos\Phi) \tag{A.1}$$

where P_l^m are associate Legendre functions. SSH functions forms a complete orthonormal basis

$$\int T_l^m(g)\, T_{l'}^{*m'}(g) dg = \delta_{ll'}\delta_{mm'} \tag{A.2}$$

where dg is the invariant measure of orientation space and "$*$" denotes complex conjugate. SSH functions is modified to reflect transverse isotropic symmetry realized in

an indentation. Symmetrized SSH functions for cubic transversely isotropic symmetry denoted as $K_l^m(g)$ are found as a linear combination of SSH functions:

$$K_l^m(g) = \sum_{m=-l}^{l} \alpha_l^m \, T_l^m(g) \tag{A.3}$$

where α_l^m are the coefficients that accounts for the cubic transversely isotropic crystal symmetry in the SSH functions. The orthonormal condition is preserved when SSH functions are symmetrized for a selected crystal system. As an example, Figure 2.10 shows the orthogonal relationship for symmetrized SSH for cubic crystals under indentation which exhibits transversely-isotropic cubic symmetry (see Figure 2.11) at truncation level of $l = 4$.

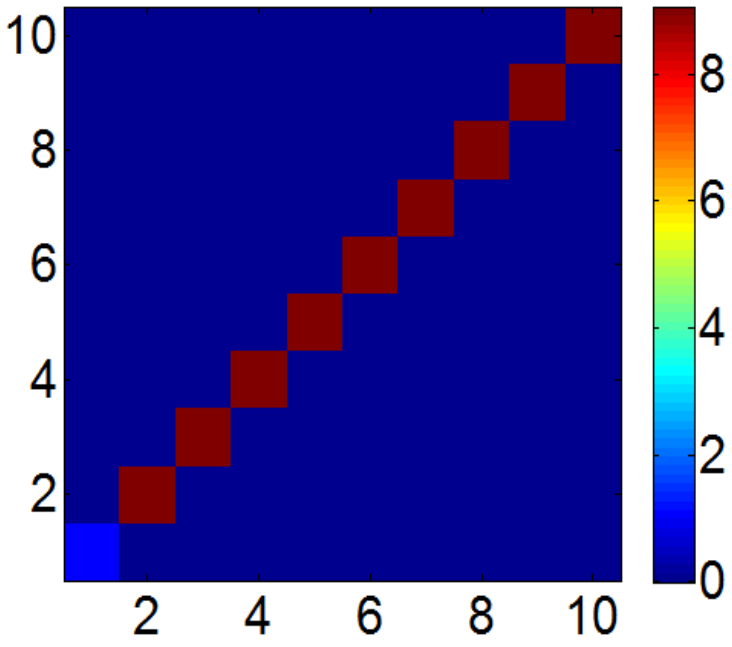

Figure A.1. Shows the symmetrized SSH basis functions are orthonormal for the truncation level, $l = 4$.

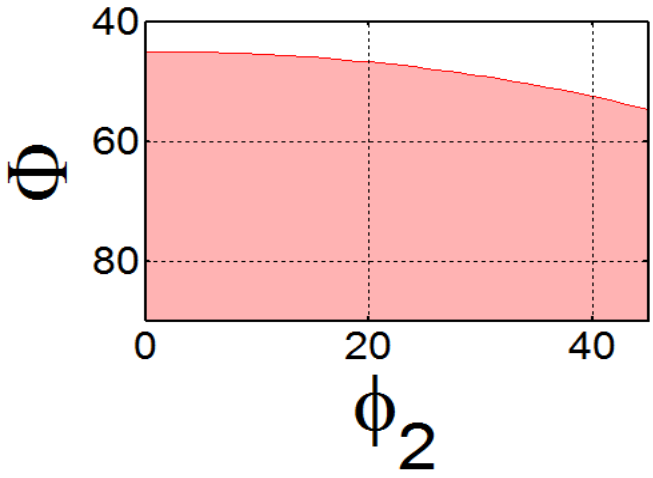

Figure A.2. The fundamental zone (shaded) for cubic lattice under indentation which possess transversely isotropic cubic symmetry.

The main advantage of utilizing Fourier representation is that an indentation response, $f(g)$ which depends on the lattice orientation, g can be represented as a Fourier series of symmetrize surface spherical harmonics, weighted with appropriate coefficients

$$f(g) = \sum_{l=0}^{\infty} \sum_{m=-l}^{+l} F_l^m \, K_l^m(g) \tag{A.4}$$

where F_l^m represents Fourier coefficients of the function $f(g)$. The most common approaches used in literature for establishing the Fourier coefficients involves exploiting the orthonormal properties of the Fourier basis (Adams et al., 2012; Kalidindi et al., 2006; Kalidindi et al., 2008; Knezevic et al., 2009). To determine the Fourier coefficient, F_l^m of a function $f(g)$, Eq. (A.4) is multiplied by the conjugate of one of the spherical harmonics function

$$f(g) = \sum_{l=0}^{\infty} \sum_{m=-l}^{+l} F_l^m \, K_l^m(g) \tag{A.5}$$

We then integrate each side over the fundamental zone (FZ) (unique orientations space for a selected crystal lattice structure),

$$\iint_{FZ} f(g) \, K_{l'}^{*m'}(g) dg = \iint_{FZ} \sum_{l=0}^{\infty} \sum_{m=-l}^{+l} F_l^m \, K_l^m(g) K_{l'}^{*m'}(g) dg \tag{A.6}$$

Exploiting the orthonormal relations, the Fourier coefficients can be expressed as

$$\iint_{FZ} f(g) \, K_{l'}^{*m'}(g) dg = \iint_{FZ} \sum_{l=0}^{\infty} \sum_{m=-l}^{+l} F_l^m \, \delta_{ll'} \delta_{mm'} = F_{l'}^{m'} \tag{A.7}$$

If the function $f(g)$ represents the microstructure of single crystal, it can be defined using a Dirac Delta function $\delta(g - g_0)$ such as

$$\iint_{FZ} \delta(g - g_0) \, dg = \begin{cases} 1, & if \; g_0 = g \\ 0, & otherwise \end{cases} \tag{A.8}$$

Hence, for single crystals the Fourier coefficients is defined as

$$F_l^m = (2l + 1) K_l^{*m}. \tag{A.9}$$

If the texture consists of several different crystals with orientation g_i, and volumes V_i, one thus obtains the coefficients as weighted average values

$$F_l^m = (2l + 1) \frac{\sum_i V_i K_l^{*m}}{\sum_i V_i}. \tag{A.10}$$

Let $\{g_i, i = 1, 2, \ldots i\}$ denote the specific orientations where the measurements are made. The function $f(g)$ then possesses a form as schematically represented in one dimension in Figure 2.12. If one extends the series expansion to very high, but finite, values of l the

discontinuous function $f(g)$ will be approximated by a continuous function. Thus, it will reproduce measurements at each individual orientation, g_i. Rather, it is generally preferable to have a smooth function which represents the distribution density of the orientation. In order to accomplish this, one has the simply truncate the series at appropriate value of l.

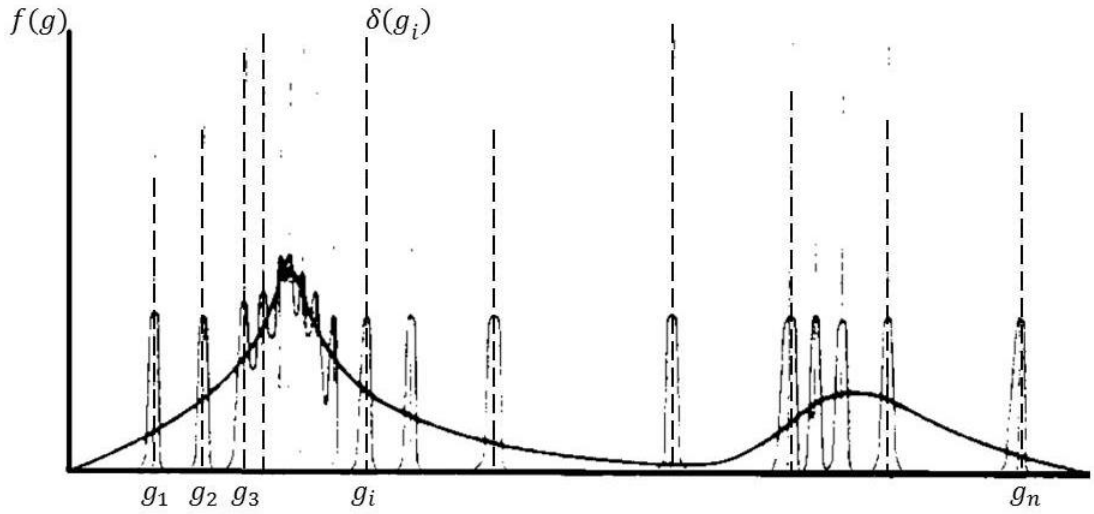

Figure A.3. Schematic of approximating a discontinuous function $f(g)$ by employing surface spherical harmonics functions in one-dimension. (Bunge, 1982)

APPENDIX B

CRYSTAL PLASTICITY FRAMEWORK

Crystal plasticity theory is used in many applications because of their ability to relate the local anisotropic response of polycrystalline materials to their microstructures (Kalidindi et al., 1992). The crystal plasticity constitutive equations described here are applied at crystal level and therefore predict the local response of each individual crystal orientation. In order to simulate the single crystal deformation behavior under the indenter in an experiment, the classical crystal plasticity constitutive equations described were used in the current work. In the FE model described in section 5.2, all integration points were assigned a single crystal orientation.

A detailed description of the implementation of the crystal plasticity modeled with a time integration implicit scheme of FE package ABAQUS through a user material subroutine (UMAT) is in Kalidindi et al. [ref]. A brief overview is given here describing the numerical work-flow of the crystal plasticity theory and its integration with ABAQUS.

At each time step, t ABAQUS outputs the total deformation gradient tensor $\boldsymbol{F}$ from which the trial stress ($\boldsymbol{T}^*$) is calculated

$$\boldsymbol{T}^* = \boldsymbol{\mathcal{L}}\boldsymbol{E}^*, \qquad \boldsymbol{E}^* = \frac{1}{2}(\boldsymbol{F}^{*T}\boldsymbol{F}^* - \boldsymbol{I}) \tag{B.1}$$

where $\boldsymbol{\mathcal{L}}$ is the fourth-order elasticity tensor. $\boldsymbol{T}^*$ and $\boldsymbol{E}^*$ are a pair of work conjugate stress and strain measures. Then the critical shear stress, τ^α is estimated as

$$\tau^\alpha = \left(\boldsymbol{F}^{*^T}\boldsymbol{F}\right)\boldsymbol{T}^* \cdot \boldsymbol{m}_0^\alpha \otimes \boldsymbol{n}_0^\alpha \approx \boldsymbol{T}^* \cdot \boldsymbol{m}_0^\alpha \otimes \boldsymbol{n}_0^\alpha. \tag{B.2}$$

The subscript "0" indicates a time invariant measure – i.e. the slip normal ($\boldsymbol{n}$) and slip direction ($\boldsymbol{m}$) remain constants throughout the deformation. In rate-dependent plasticity,

the shearing rate ($\dot{\gamma}^{\alpha}$) is iteratively calculated using the viscoplastic power law which phenomenologically describes the dependence of slip activity due to the imposed resolved shear stress on the slip system, α. The shear rate on the slip system, $\dot{\gamma}^{\alpha}$ is defined as

$$\dot{\gamma^{\alpha}} = \dot{\gamma}_0 \left|\frac{\tau^{\alpha}}{s^{\alpha}}\right|^{\frac{1}{m}} \mathrm{sgn}(\tau^{\alpha}) \tag{B.3}$$

where $\dot{\gamma}_0$ is the reference shear rate and m is the strain rate sensitivity parameter. For most metals at room temperature the value of m is assumed to be very small (~0.01). The evolution of the slip resistance can be described by a saturation type hardening law as

$$\dot{s}^{\alpha} = h_0 \left(1 - \frac{s^{\alpha}}{s_s}\right)^{a} \sum_{\beta} \left|\dot{\gamma^{\beta}}\right| \tag{B.4}$$

where h_0, s_s and a denote the slip hardening parameters. It should be noted that Eq. (B.3) assumes that all systems hardens equally. Once a shearing rate is determined that satisfies the current state of stress, the plastic velocity gradient ($\boldsymbol{L}^p$) is tabulated as

$$\boldsymbol{L}^p = \sum_{\alpha} \dot{\gamma^{\alpha}}\, \boldsymbol{m}_0^{\alpha} \otimes \boldsymbol{n}_0^{\alpha}. \tag{B.5}$$

Then, the plastic deformation evolution, $\dot{\boldsymbol{F}}^p$ is described by the following rule:

$$\dot{\boldsymbol{F}}^p = \boldsymbol{L}^p \boldsymbol{F}^p \tag{B.6}$$

where $\boldsymbol{F}^p$ is the plastic deformation tensor. Eq. (B.6) is solved for $\boldsymbol{F}^p$ numerically via fully-implicit time-integration scheme

$$\boldsymbol{F}^p(t + \Delta t) = \boldsymbol{e}^{\{\Delta t \boldsymbol{L}^p(t+\Delta t)\}} \boldsymbol{F}^p(t) \tag{B.7}$$

where the exponential function is approximated via Taylor expansion. Once the plastic deformation is known, the elastic deformation $\boldsymbol{F}^*$ can be easily calculated from the elastic-plastic decomposition rule:

$$\boldsymbol{F} = \boldsymbol{F}^{*}\boldsymbol{F}^{p}. \tag{B.8}$$

The Cauchy Stress, $\boldsymbol{T}$ in the crystal is defined as

$$\boldsymbol{F} = \boldsymbol{F}^{*}\boldsymbol{F}^{p}. \tag{B.9}$$

Finally, the lattice spin tensor $\boldsymbol{W}^{*}$ (and the related lattice rotation tensor, $\boldsymbol{R}^{*}$) in the crystalline region is updated by

$$\boldsymbol{W}^{*} = \dot{\boldsymbol{R}}^{*}\boldsymbol{R}^{*T} = \boldsymbol{W} - \boldsymbol{W}^{p}, \qquad \boldsymbol{W}^{p} = \frac{1}{2}(\boldsymbol{L}^{p} - \boldsymbol{L}^{pT}) \tag{B.10}$$

where $\boldsymbol{W}$ is the applied spin tensor and $\boldsymbol{W}^{p}$ is the plastic spin tensor. The constitutive behavior described above determines the response of an individual grain at each time step increment.

REFERENCES

ABAQUS, 2014. Simulia Providence, RI: Dassault Systemes.

Abu Al-Rub, R.K., Voyiadjis, G.Z., 2004. Analytical and experimental determination of the material intrinsic length scale of strain gradient plasticity theory from micro- and nano-indentation experiments. International Journal of Plasticity 20, 1139-1182.

Adams, B.L., Kalidindi, S.R., Fullwood, D.T., 2012. Microstructure Sensitive Design for Performance Optimization. Elsevier Science.

Alberts, H., Wedepohl, P., 1971. Elastic constants of dilute iron-silicon alloy single crystals below room temperature. Physica 53, 571-580.

Anand, L., Kalidindi, S.R., 1994. The process of shear-band formation in plane-strain compression of FCC-metals - effects of crystallographic texture. Mechanics of Materials 17, 223-243.

Asgari, S., ElDanaf, E., Kalidindi, S.R., Doherty, R.D., 1997. Strain hardening regimes and microstructural evolution during large strain compression of low stacking fault energy fcc alloys that form deformation twins. Metallurgical and Materials Transactions a-Physical Metallurgy and Materials Science 28, 1781-1795.

ASTM, 2015. Standard Tests Methods for Tension Testing of Metallic Materials, ASTM International, West Conshohocken, PA.

Bachu, V., Kalidindi, S.R., 1998. On the accuracy of the predictions of texture evolution by the finite element technique for fcc polycrystals. Materials Science and Engineering a-Structural Materials Properties Microstructure and Processing 257, 108-117.

Barlat, F., Maeda, Y., Chung, K., Yanagawa, M., Brem, J.C., Hayashida, Y., Lege, D.J., Matsui, K., Murtha, S.J., Hattori, S., Becker, R.C., Makosey, S., 1997. Yield function development for aluminum alloy sheets. Journal of the Mechanics and Physics of Solids 45, 1727-1763.

Basu, S., Moseson, A., Barsoum, M.W., 2006. On the determination of spherical nanoindentation stress–strain curves. Journal of Materials Research 21, 2628-2637.

Becker, R., 1991. Analysis of texture evolution in channel die compression-I. Effects of grain interaction. Acta Metallurgica Et Materialia 39, 1211-1230.

Beghini, M., Bertini, L., Fontanari, V., 2006. Evaluation of the stress-strain curve of metallic materials by spherical indentation. International Journal of Solids and Structures 43, 2441-2459.

Beyerlein, I.J., Tomé, C.N., 2007. Modeling transients in the mechanical response of copper due to strain path changes. International Journal of Plasticity 23, 640-664.

Bhattacharya, A.K., Nix, W.D., 1988. Finite element simulation of indentation experiments. International Journal of Solids and Structures 24, 881-891.

Bhattacharyya, A., El-Danaf, E., Kalidindi, S.R., Doherty, R.D., 2001. Evolution of grain-scale microstructure during large strain simple compression of polycrystalline aluminum with quasi-columnar grains: OIM measurements and numerical simulations. International Journal of Plasticity 17, 861-883.

Bishop, C.M., 2006. Pattern Recognition and Machine Learning. Springer.

Bishop, R.F., Hill, R., Mott, N.F., 1945. The theory of indentation and hardness tests. Proceedings of the Physical Society 57, 147-159.

Bron, F., Besson, J., 2004. A yield function for anisotropic materials Application to aluminum alloys. International Journal of Plasticity 20, 937-963.

Bronkhorst, C.A., Kalidindi, S.R., Anand, L., 1992. Polycrystalline Plasticity and the evolution of crystallogrpahic texture in FCC metals. Philosophical Transactions of the Royal Society of London Series A-Mathematical Physical and Engineering Sciences 341, 443-477.
Bucaille, J.L., Stauss, S., Felder, E., Michler, J., 2003. Determination of plastic properties of metals by instrumented indentation using different sharp indenters. Acta Materialia 51, 1663-1678.
Cammarata, R., Schlesinger, T., Kim, C., Qadri, S., Edelstein, A., 1990. Nanoindentation study of the mechanical properties of copper-nickel multilayered thin films. Applied Physics Letters 56, 1862-1864.
Çeçen, A., Fast, T., Kumbur, E.C., Kalidindi, S.R., 2014. A data-driven approach to establishing microstructure–property relationships in porous transport layers of polymer electrolyte fuel cells. Journal of Power Sources 245, 144-153.
Cheng, Y.-T., Cheng, C.-M., 1999. Scaling relationships in conical indentation of elastic-perfectly plastic solids. International Journal of Solids and Structures 36, 1231-1243.
Copson, E.T., 1950. An Introduction to the Theory of Functions of a Complex Variable. Clarendon Press.
Cordill, M.J., Moody, N.R., Gerberich, W.W., 2009. The role of dislocation walls for nanoindentation to shallow depths. International Journal of Plasticity 25, 281-301.
Dao, M., Chollacoop, N., Van Vliet, K.J., Venkatesh, T.A., Suresh, S., 2001. Computational modeling of the forward and reverse problems in instrumented sharp indentation. Acta Materialia 49, 3899-3918.
Delannay, L., Melchior, M.A., Signorelli, J.W., Remacle, J.F., Kuwabara, T., 2009. Influence of grain shape on the planar anisotropy of rolled steel sheets - evaluation of three models. Computational Materials Science 45, 739-743.
Doerner, M.F., Nix, W.D., 1986. A method for interpreting the data from depth-sensing indentation instruments. Journal of Materials Research 1, 601-609.
Donohue, B.R., Ambrus, A., Kalidindi, S.R., 2012. Critical evaluation of the indentation data analyses methods for the extraction of isotropic uniaxial mechanical properties using finite element models. Acta Materialia 60, 3943-3952.
Farthing, L., Weihs, T., Kisker, D., Krajewski, J., Tang, M., Stevenson, D., 1988. Hardness and elastic modulus measurements in CdTe and ZnTe thin film and bulk samples and ZnTe-CdTe superlattices, MRS Proceedings. Cambridge Univ Press.
Fast, T., Knezevic, M., Kalidindi, S.R., 2008. Application of microstructure sensitive design to structural components produced from hexagonal polycrystalline metals. Computational Materials Science 43, 374-383.
Field, J., Swain, M., 1993. A simple predictive model for spherical indentation. Journal of Materials Research(USA) 8, 297-306.
Field, J.S., Swain, M.V., 1995. Determining the mechanical properties of small volumes of material from submicrometer spherical indentations. Journal of Materials Research 10, 101-112.
Fischer-Cripps, A., 1997. Elastic–plastic behaviour in materials loaded with a spherical indenter. Journal of materials science 32, 727-736.
Fischer-Cripps, A.C., 2011. Nanoindentation. Springer New York.

Fullwood, D.T., Niezgoda, S.R., Adams, B.L., Kalidindi, S.R., 2010. Microstructure sensitive design for performance optimization. Progress in Materials Science 55, 477-562.
Gambin, W., Barlat, F., 1997. Modeling of deformation texture development based on rate independent crystal plasticity. International Journal of Plasticity 13, 75-85.
Gianola, D., Eberl, C., 2009. Micro-and nanoscale tensile testing of materials. JOM 61, 24-35.
Groh, S., Marin, E.B., Horstemeyer, M.F., Zbib, H.M., 2009. Multiscale modeling of the plasticity in an aluminum single crystal. International Journal of Plasticity 25, 1456-1473.
H, B., 1982. Texture Analysis in Material Science. London.
H., H., 1896. Miscellaneous papers. New York: Macmillan.
Haddadi, H., Bouvier, S., Banu, M., Maier, C., Teodosiu, C., 2006. Towards an accurate description of the anisotropic behaviour of sheet metals under large plastic deformations: Modelling, numerical analysis and identification. International Journal of Plasticity 22, 2226-2271.
Hashin, Z., Shtrikman, S., 1962. On some variational principles in anisotropic and nonhomogeneous elasticity. Journal of the Mechanics and Physics of Solids 10, 335-342.
Herbert, E.G., Pharr, G.M., Oliver, W.C., Lucas, B.N., Hay, J.L., 2001. On the measurement of stress-strain curves by spherical indentation. Thin Solid Films 398-399, 331-335.
Hertz, H., 1896. Miscellaneous Papers. MacMillan and Co., Ltd., New York.
Hill, R., 1948. A Theory of the Yielding and Plastic Flow of Anisotropic Metals.
Hill, R., Lee, E.H., Tupper, S.J., 1947. The Theory of Wedge Indentation of Ductile Materials.
Hill, R., Storakers, B., Zdunek, A.B., 1989. A Theoretical Study of the Brinell Hardness Test.
Hull, D., 1963. Orientation and Temperature Dependence of Plastic Deformation Processes in 3.25% Silicon Iron. Proceedings of the Royal Society of London A: Mathematical, Physical and Engineering Sciences 274, 5-20.
Ishlinsky, A.I., 1944. The axi-symmetrical problem in plasticity and the Brinell test. Journal of Applied Mathematics and Mechanics 8, 201.
Johnson, K.L., 1987. Contact Mechanics. Cambridge University Press.
Johnson, K.L., Johnson, K.K.L., 1987. Contact Mechanics. Cambridge University Press.
Kalidindi, S.R., Anand, L., 1992. An approximate procedure for predicting the evolution of crystallographic texture in bulk deformation processing of fcc metals. International Journal of Mechanical Sciences 34, 309-329.
Kalidindi, S.R., Anand, L., 1994. MACROSCOPIC SHAPE CHANGE AND EVOLUTION OF CRYSTALLOGRAPHIC TEXTURE IN PRE-TEXTURED FCC METALS. Journal of the Mechanics and Physics of Solids 42, 459-490.
Kalidindi, S.R., Bhattacharyya, A., Doherty, R.D., 2004. Detailed analyses of grain-scale plastic deformation in columnar polycrystalline aluminium using orientation image mapping and crystal plasticity models. Proceedings of the Royal Society of London Series a-Mathematical Physical and Engineering Sciences 460, 1935-1956.
Kalidindi, S.R., Bhattacharyya, A.,Doherty, R.D., 2004. Detailed analysis of grain-scale plastic deformation in columnar polycrystalline aluminum using orientation image mapping and crystal plasticicty models. Proc. R. Soc. A 460, 1935-1956.

Kalidindi, S.R., Bronkhorst, C.A., Anand, L., 1992. Crystallographic texture evolution in bulk deformation processing of FCC metals. Journal of the Mechanics and Physics of Solids 40, 537-569.
Kalidindi, S.R., Duvvuru, H.K., Knezevic, M., 2006. Spectral calibration of crystal plasticity models. Acta Materialia 54, 1795-1804.
Kalidindi, S.R., Landi, G., Fullwood, D.T., 2008. Spectral representation of higher-order localization relationships for elastic behavior of polycrystalline cubic materials. Acta Materialia 56, 3843-3853.
Kalidindi, S.R., Pathak, S., 2008. Determination of the effective zero-point and the extraction of spherical nanoindentation stress-strain curves. Acta Materialia 56, 3523-3532.
Kalidindi, S.R., Schoenfeld, S.E., 2000. On the prediction of yield surfaces by the crystal plasticity models for fcc polycrystals. Materials Science and Engineering a-Structural Materials Properties Microstructure and Processing 293, 120-129.
Kalpakjian, S., Schmid, S.R., 2008. Manufacturing Processes for Engineering Materials. Pearson Education.
Klusemann, B., Svendsen, B., Vehoff, H., 2012. Investigation of the deformation behavior of Fe–3%Si sheet metal with large grains via crystal plasticity and finite-element modeling. Computational Materials Science 52, 25-32.
Knezevic, M., Al-Harbi, H.F., Kalidindi, S.R., 2009. Crystal plasticity simulations using discrete Fourier transforms. Acta Materialia 57, 1777-1784.
Kocks, U.F., Tomé, C.N., Wenk, H.R., 2000. Texture and Anisotropy: Preferred Orientations in Polycrystals and Their Effect on Materials Properties. Cambridge University Press.
Kucharski, S., Mróz, Z., 2001. Identification of plastic hardening parameters of metals from spherical indentation tests. Materials Science and Engineering A 318, 65-76.
Lebensohn, R.A., Tomé, C.N., 1993. A self-consistent anisotropic approach for the simulation of plastic deformation and texture development of polycrystals: Application to zirconium alloys. Acta Metallurgica Et Materialia 41, 2611-2624.
Li, D.S., Garmestani, H., Schoenfeld, S., 2003. Evolution of crystal orientation distribution coefficients during plastic deformation. Scripta Materialia 49, 867-872.
Li, N., Mara, N.A., Wang, Y.Q., Nastasi, M., Misra, A., 2011. Compressive flow behavior of Cu thin films and Cu/Nb multilayers containing nanometer-scale helium bubbles. Scripta Materialia 64, 974-977.
Li, X., Bhushan, B., 2002. A review of nanoindentation continuous stiffness measurement technique and its applications. Materials Characterization 48, 11-36.
Liu, Y., Varghese, S., Ma, J., Yoshino, M., Lu, H., Komanduri, R., 2008. Orientation effects in nanoindentation of single crystal copper. International Journal of Plasticity 24, 1990-2015.
Machova, A., Kadečková, S., 1977. Elastic constants of iron-silicon alloy single crystals. Czechoslovak Journal of Physics B 27, 555-563.
McDowell, D.L., 2010. A perspective on trends in multiscale plasticity. International Journal of Plasticity, special issue in honor of David L. McDowell 26(9), 1280-1309.
Oliver, W.C., Pethica, J.B., 1989. Method for continuous determination of the elastic stiffness of contact between two bodies. Google Patents.

Oliver, W.C., Pharr, G.M., 1992. An improved technique for determining hardness and elastic modulus using load and displacement sensing indentation experiments. Journal of Materials Research 7, 1564-1583.
Orlans-Joliet, B., Driver, J.H., Montheillet, F., 1990. Plane strain compression of silicon-iron single crystals. Acta Metallurgica et Materialia 38, 581-594.
Panchal, J.H., Kalidindi, S.R., McDowell, D.L., 2013. Key computational modeling issues in integrated computational materials engineering. Computer-Aided Design 45, 4-25.
Park, Y.J., Pharr, G.M., 2004. Nanoindentation with spherical indenters: Finite element studies of deformation in the elastic-plastic transition regime. Thin Solid Films 447-448, 246-250.
Patel, D.K., Al-Harbi, H.F., Kalidindi, S.R., 2014. Extracting single-crystal elastic constants from polycrystalline samples using spherical nanoindentation and orientation measurements. Acta Materialia 79, 108-116.
Pathak, S., Kalidindi, S.R., 2015. Spherical nanoindentation stress–strain curves. Materials Science and Engineering: R: Reports 91, 1-36.
Pathak, S., Kalidindi, S.R., Klemenz, C., Orlovskaya, N., 2008. Analyzing indentation stress-strain response of LaGaO3 single crystals using spherical indenters. Journal of the European Ceramic Society 28, 2213-2220.
Pathak, S., Stojakovic, D., Kalidindi, S.R., 2009. Measurement of the local mechanical properties in polycrystalline samples using spherical nanoindentation and orientation imaging microscopy. Acta Materialia 57, 3020-3028.
Pelletier, H., 2006. Predictive model to estimate the stress-strain curves of bulk metals using nanoindentation. Tribology International 39, 593-606.
Press, W.H., 2007. Numerical Recipes 3rd Edition: The Art of Scientific Computing. Cambridge University Press.
Proust G, K.S., 2004. Effect of the crystal orientation on the measured response during nanoindentation. TMS Letters (The Minerals, Metals and Materials Society) 7, 151.
Raabe, D., Klose, P., Engl, B., Imlau, K.-P., Friedel, F., Roters, F., 2002. Concepts for integrating plastic anisotropy into metal forming simulations. Advanced Engineering Materials 4, 169.
Roters, F., Eisenlohr, P., Bieler, T.R., Raabe, D., 2011. Crystal Plasticity Finite Element Methods: in Materials Science and Engineering. Wiley.
Roters, F., Eisenlohr, P., Hantcherli, L., Tjahjanto, D.D., Bieler, T.R., Raabe, D., 2010. Overview of constitutive laws, kinematics, homogenization and multiscale methods in crystal plasticity finite-element modeling: Theory, experiments, applications. Acta Materialia 58, 1152-1211.
Routbort, J., Reid, C., Fisher, E., Dever, D., 1971. High-temperature elastic constants and the phase stability of silicon-iron. Acta Metallurgica 19, 1307-1316.
Sarma, G.B., Dawson, P.R., 1996. Texture predictions using a polycrystal plasticity model incorporating neighbor interactions. International Journal of Plasticity 12, 1023-1054.
Segurado, J., Lebensohn, R.A., Llorca, J., Tomé, C.N., 2012. Multiscale modeling of plasticity based on embedding the viscoplastic self-consistent formulation in implicit finite elements. International Journal of Plasticity 28, 124-140.

Shan, Z.W., Mishra, R.K., Syed Asif, S.A., Warren, O.L., Minor, A.M., 2008. Mechanical annealing and source-limited deformation in submicrometre-diameter Ni crystals. Nat Mater 7, 115-119.
Simmons, G., Wang, H., 1971. Single crystal elastic constants and calculated aggregate properties: a handbook. M.I.T. Press.
Suits, J.C., Chalmers, B., 1961. Plastic microstrain in silicon-iron. Acta Metallurgica 9, 854-860.
Suresh, S., Giannakopoulos, A., 1998. A new method for estimating residual stresses by instrumented sharp indentation. Acta Materialia 46, 5755-5767.
Swain, M.V., 1998. Mechanical property characterisation of small volumes of brittle materials with spherical tipped indenters. Materials Science and Engineering A 253, 160-166.
Tabor, D., 1948. A Simple Theory of Static and Dynamic Hardness.
Tabor, D., 1951. The Hardness of Metals. ClarendonP.
Taljat, B., Zacharia, T., Kosel, F., 1998. New analytical procedure to determine stress-strain curve from spherical indentation data. International Journal of Solids and Structures 35, 4411-4426.
Taylor, G.I., 1934. The Mechanism of Plastic Deformation of Crystals. Part I. Theoretical. Proceedings of the Royal Society of London A: Mathematical, Physical and Engineering Sciences 145, 362-387.
Taylor, G.I., 1938. Plastic strain in metals. 307-324.
Tikhovskiy, I., Raabe, D., Roters, F., 2007. Simulation of earing during deep drawing of an Al-3% Mg alloy (AA 5754) using a texture component crystal plasticity FEM. Journal of Materials Processing Technology 183, 169-175.
Tomé, C.N., Lebensohn, R.A., Necker, C.T., 2002. Mechanical anisotropy and grain interaction in recrystallized aluminum. Metallurgical and Materials Transactions A: Physical Metallurgy and Materials Science 33, 2635-2648.
Tomé, C.N., Maudlin, P.J., Lebensohn, R.A., Kaschner, G.C., 2001. Mechanical response of zirconium—I. Derivation of a polycrystal constitutive law and finite element analysis. Acta Materialia 49, 3085-3096.
Uchic, M.D., Dimiduk, D.M., Florando, J.N., Nix, W.D., 2004. Sample Dimensions Influence Strength and Crystal Plasticity. Science 305, 986-989.
Vachhani, S.J., Doherty, R.D., Kalidindi, S.R., 2013. Effect of the continuous stiffness measurement on the mechanical properties extracted using spherical nanoindentation. Acta Materialia 61, 3744-3751.
Vachhani, S.J., Doherty, R.D., Kalidindi, S.R., 2016. Studies of grain boundary regions in deformed polycrystalline aluminum using spherical nanoindentation. International Journal of Plasticity 81, 87-101.
Vlassak, J., Ciavarella, M., Barber, J., Wang, X., 2003. The indentation modulus of elastically anisotropic materials for indenters of arbitrary shape. Journal of the Mechanics and Physics of Solids 51, 1701-1721.
Vlassak, J.J., Nix, W., 1993. Indentation modulus of elastically anisotropic half spaces. Philosophical Magazine A 67, 1045-1056.
Vlassak, J.J., Nix, W., 1994. Measuring the elastic properties of anisotropic materials by means of indentation experiments. Journal of the Mechanics and Physics of Solids 42, 1223-1245.

Willis, J., 1966. Hertzian contact of anisotropic bodies. Journal of the Mechanics and Physics of Solids 14, 163-176.
Yu, W., Blanchard, J.P., 1996. An elastic-plastic indentation model and its solutions. Journal of Materials Research 11, 2358-2367.
Zaafarani, N., Raabe, D., Singh, R.N., Roters, F., Zaefferer, S., 2006. Three-dimensional investigation of the texture and microstructure below a nanoindent in a Cu single crystal using 3D EBSD and crystal plasticity finite element simulations. Acta Materialia 54, 1863-1876.
Zhang, H., Schuster, B.E., Wei, Q., Ramesh, K.T., 2006. The design of accurate micro-compression experiments. Scripta Materialia 54, 181-186.
Zhao, Z., Roters, F., Mao, W., Raabe, D., 2001. Introduction of a Texture Component Crystal Plasticity Finite Element Method for Anisotropy Simulations. Advanced Engineering Materials 3, 984-990.